Pilot's Detection of Change in Aircraft Dynamics

An Open-Loop Stability Model For Varying Display Types and Transition Rates

Devashish Patel

Delft University of Technology

TU Delft

Pilot's Detection of Change in Aircraft Dynamics

An Open-Loop Stability Model For Varying Display Types and Transition Rates

Thesis report
by

Devashish Patel

to obtain the degree of Master of Science
at the Delft University of Technology
to be defended publicly on May 15, 2024 at 14:00

Thesis committee:

Supervisors:	Prof. Dr Ir. Max Mulder
	Dr Ir. M.M. van Paassen
	Dr Ir. Daan M. Pool
Place:	Faculty of Aerospace Engineering, Delft
Project Duration:	September 2023 - May 2024
Student number:	5459990

An electronic version of this thesis is available at `https://repository.tudelft.nl/`.

Cover Image Credits: William Topa on Unsplash

Faculty of Aerospace Engineering · Delft University of Technology

Preface

This thesis report is the culmination of the hard work done over the past year to obtain a master's in aerospace engineering; a milestone no short of a dream come true. The report starts with the literature review and preliminary simulations followed by the scientific article. The research conducted in the span of this study has been truly fulfilling and would not have been possible without my supervisors, Max, Daan and Rene. Your patience and guidance were vital to the existence of this thesis. Importantly, I would like to thank my family, who have always been a cornerstone and a constant motivation for me along with my friends, without whom, I cannot thrive or survive. It is because of all of these people, that I have had a beautiful time here in Delft.

I hope you enjoy reading this report!

Devashish Patel
Delft, May 2024

Contents

Nomenclature

List of Abbreviations

C	Compensatory Display
CE	Controlled Element
CL	Closed-loop
DI	Double integrator
FCS	Flight Control System
G	Rate of change [sec^{-1}]
HMI	Human-Machine Interface
HO/HC	Human Operator/Controller
LOC-I	Loss of Control-In-flight
LPV	Linear Parameter-Varying
LTI	Linear Time Invariant
M	Moment of maximum rate of change [sec]
MLE	Maximum Likelihood Estimation
MMS	Man-Machine Systems
NMS	Neuromuscular System
OL	Open-loop
P	Pursuit Display
PIO	Pilot Induced Oscillation
SAS	Stability Augmentation System
SI	Single integrator
TV	Time Varying

List of Symbols

ω_c	Crossover frequency
ω_{nm}	NMS frequency
τ_e	Effective Time Delay
ζ_{nm}	NMS damping ratio
H_n/H_r	Remnant model transfer function
$H_p(s)$	Pilot transfer function
$H_{CE}(s)$	Controlled element transfer function
H_{NMS}	Neuromuscular transfer function
K_n	Remnant gain
n	Remnant signal
T_I	Lag time constant
T_L	Lead time constant
T_n	Remnant time constant
W	Gaussian white noise
$j\omega$	Frequency-domain
t	Time-domain

List of Figures

List of Tables

Part I

Literature Review & Research Definition

1

Introduction

Vehicles have played a pivotal role in the development and progress of the human civilization over several centuries and the one common link among the usage of all types of vehicles has been the role of humans in controlling them. Human control of vehicles has been a burning question for decades and understanding *how* humans control vehicles can help improve safety and vehicle design [1]. This study of human-vehicle control has now evolved into a mature field of study called manual control. As stated by Mulder et al., "Manual control cybernetics aims to understand and describe how humans control vehicles and devices using mathematical models of human control dynamics" [2]; with Weiner describing cybernetics as the main system-theoretical, model-based approach to understand how humans control vehicles and devices [3]. As a result, manual control research has led to many important insights in the field of aerospace engineering. A prime example of this is the famous crossover model proposed by McRuer and Jex in their seminal work [4], which is a mathematical model that describes how the human operator adapts to the vehicle dynamics for tracking tasks using a compensatory display.

In aviation, Loss of Control-inflight (LOC-I) has long been one of the top causes of fatal accidents [5]; such LOC-I situations can also arise, for example, in the case of Stability Augmentation System (SAS) failures and manual control can help develop insights into (adaptive)human behaviour and consequently increase safety. Humans are known to have adaptive behavioural strategies that they use when a change is detected in the dynamics of the element that they are trying to control, i.e., in our case, the vehicle/aircraft. In manual control, the vehicle/aircraft is termed a controlled element (CE) which makes the pilot the human operator/controller (HO). While manual control research and studies are available for pilot behaviour in varied scenarios, they are majorly focused on Linear Time-Invariant (LTI) systems with only a few experiments conducted for pilot model identification in time-variant cases.

With the present understanding of adaptive pilot behaviour and most of this research being focused on the development of complex mathematical models to describe time-varying behaviour and not on understanding these time-varying parameters, we lack valuable insight into how a pilot adapts to time-varying CE dynamics [6]. There is a clear gap in understanding how well the adaptive behaviour of the human pilot can handle the time-varying vehicle dynamics. Accordingly, this study aims to understand and analyse the stability of the resultant system obtained as the output of the adaptive pilot changing their control behaviour to time-varying aircraft dynamics to better understand the adaptive nature of the pilot. This is also backed by Mulder et al. in [3] which states that the temporal scales of human adaptation and learning in changing situations should be addressed using open-loop techniques to assess the combined dynamic stability in time. Therefore, the main research objective of this thesis is:

Research Objective

Utilize open-loop techniques to analytically and experimentally investigate how adaptive human controllers employ the changes in combined pilot-aircraft dynamic stability to detect changes in controlled element dynamics during manual tracking tasks.

In the context of our specific research inquiry, which is:

Research Question

How does the human operator use the reduced stability/complete instability of the open-loop system to detect the change in controlled element dynamics?

To help answer the main research question, the following sub-questions have been formulated:

1. What time-domain signals, in and near the region of reduced stability or instability, are used by the human controller to detect the change in controlled element dynamics?
2. What are the specific characteristics and numerical values of the relevant signal(s)?
3. How does the rate of change in controlled element dynamics affect the detection of this change?
4. How does the type of display (compensatory/pursuit) affect the human operator's detection of change in controlled element dynamics?

The chapters of this literature report are structured such that Chapter 2 encompasses the background study required for this thesis and explores various facets of multiple researches in the domain of manual control followed by Chapter 3 that details the initial simulations and their results to back the proposed research methodology.

2

Literature Review

This chapter thoroughly examines the existing body of knowledge in the field of manual control, with a focus on time-varying controlled element dynamics. By articulating and analysing existing literature, this chapter will lay a solid foundation for the research question and the subsequent research efforts to prove the presented hypotheses.

The sections of this chapter, namely, section 2.1, section 2.2 and section 2.3 elaborate on the concepts of manual control, existing research in this field and conclusion, respectively. This is followed by chapter 3 that shows preliminary simulations with procedure and results, conducted using MATLAB that will be used as a basis to conduct further analytical and experimental research.

2.1. Concepts of Manual Control

This section bases itself on the foundations of simulations and experiments carried out in the field of manual control and the main variables they utilize. As mentioned by McRuer and Jex, the human pilot has the capability of adjusting or equalizing his behaviour so that the closed-loop characteristics fulfil the basic conditions required of any good feedback control system [7], which are:

- Provides some desired command-response ($f_t \rightarrow y$) relationship
- Suppress unwanted inputs and disturbances(f_d)
- Reduces the effects of variations and uncertainties in the components of the control loop
- Provides adequate closed-loop stability margins.

To understand these further a compensatory tracking task as seen in Figure 2.1 will be used as a reference in this section. Here, the different blocks and their details are explained in the subsections that follow.

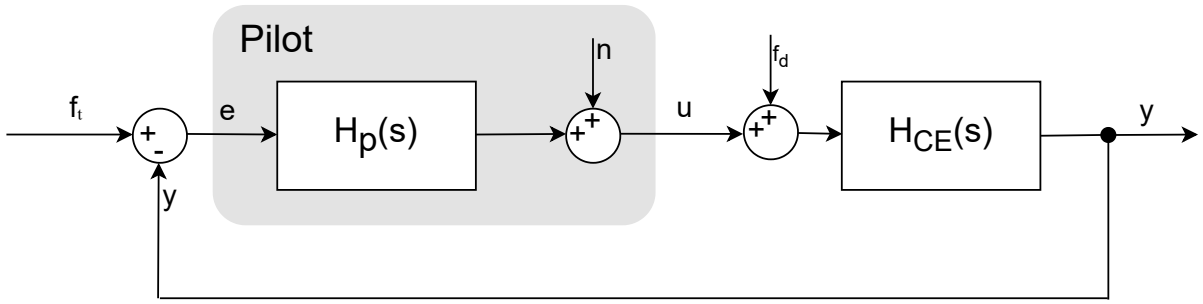

Figure 2.1: Compensatory tracking task

Thus, this chapter serves as an introduction to the important concepts of manual control highly relevant to the thesis and is divided into four sections with each articulating a different facet.

2.1.1. Forcing functions

In a manual tracking task, the pilot, whose linear part is represented in the above figure by $H_p(s)$ and the non-linear part by the remnant n controls the aircraft/vehicle represented by $H_{CE}(s)$ given the forcing function f_t. This forcing function depicts the actual task at hand, for example, changing the altitude of the aircraft, making a coordinated turn or maintaining a wings-level flight during turbulence. In system identification tasks, these forcing function signals are used to excite the pilot's control behaviour [8] and are kept to be fairly representative of the task at hand. Moreover, forcing function signals are kept unpredictable for the human and difficult enough to prevent boredom in order to obtain high levels of control behaviour linearity and limit subject variability [4, 9]. There are a number of characteristics that need to be considered when designing a forcing function that are mentioned below as obtained from [4, 9, 10, 11, 12],

- The forcing function must be random-appearing, to prevent the human from detecting patterns in the signal. When the human controller can anticipate the forcing function, his behaviour can no longer be modelled by a feedback system but should include a feedforward path as well.
- The forcing function must be sufficiently exciting, to get the human engaged in the proper way and maximize the accuracy of the describing function.
- The forcing function must have a high signal-to-noise ratio at frequencies of interest, to maximize the accuracy of identification.
- The forcing function must have a Gaussian magnitude distribution, to obtain describing functions that resemble real-life control behaviour as closely as possible.
- The number of sinusoids is limited such that the signal power does not get diluted over too many frequencies.
- Preferably an equally spaced separation on a logarithmic scale of the integer frequencies over approximately two decades is applied in order to identify the describing function.

These characteristics of the quasi-random multisine signals force compensatory control behaviour and also facilitate the frequency domain describing functions of the human pilot in compensatory tracking tasks. A standard set of forcing functions generally used to compare spectrums are the ones used in McRuer's work [4] where he used three spectrums, namely, 6:4, 7:3 and 8:2 which signifies the low-frequency high power to high-frequency low power ratio of the number of sinusoids used, which resulted in them having a bandwidth of $1.5rad/s$, $2.5rad/s$ and $4.0rad/s$, respectively.

2.1.2. Pilot Model

The forcing functions discussed above are used to excite the pilot control behaviour. The human pilot is a multimode, adaptive, learning controller capable of exhibiting an enormous variety of behaviour [7]. As seen in Figure 2.1, the pilot model consists of a linear part, i.e., $H_p(s)$ and a non-linear part n. There have been multiple attempts at mathematical modelling of the human pilot but the most prominent model, which is also the one used in this study, is the precision model proposed by Mcruer et al. in [4]. Equation 2.1 shows the model with the difference that it omits the indifference threshold describing function.

$$H_p(j\omega) = \overbrace{K_p\left(\frac{T_L j\omega + 1}{T_I j\omega + 1}\right)}^{\text{equalization}} \overbrace{\left(\frac{T_K j\omega + 1}{T'_K j\omega + 1}\right)}^{\text{low-freq. lag-lead}} \overbrace{e^{-j\omega\tau}}^{\text{delay}} \overbrace{\left[\frac{1}{(T_N j\omega + 1)\left(\left[\frac{j\omega}{\omega_{nm}}\right]^2 + \frac{2\zeta_{nm} j\omega}{\omega_{nm}} + 1\right)}\right]}^{\text{neuromuscular dynamics, } H_{nm}} \tag{2.1}$$

In this equation, the *equalization* term represents the main adaptation of the pilot to the CE dynamics with $\mathcal{T}_L$ and T_I being the lead and lag time constants respectively. This use of lead and/or lag depends on the type of CE dynamics controlled by the pilot. The second term, i.e., the low-frequency lead-lag term is included to capture the low-frequency phase equalization but is frequently omitted based on the frequencies in the experiment. The third term is the time-delay term where τ (alternatively written as τ_e) accounts for the effective time-delay followed by the last term representing the neuromuscular system (NMS) dynamics. This equation has been simplified to take the form shown in Equation 2.2 with the NMS dynamics simplified to be that of the second order and with the low-frequency term being omitted.

$$H_p(j\omega) = K_p \left(\frac{T_L j\omega + 1}{T_I j\omega + 1} \right) e^{-j\omega\tau_e} \left[\frac{\omega_{nm}^2}{s^2 + 2\zeta_{nm}\omega_{nm} + \omega_{nm}^2} \right] \tag{2.2}$$

As seen in Figure 2.1, n is added to the pilot model. This is the non-linear part of the pilot model, i.e., remnant is defined as the portion of the pilot's control output power which is not linearly correlated with the system input. The remnant accounts for all the non-linearities and is often omitted while modelling the pilot or during system identification studies, like in the case of McRuer's quasi-linear model described above. As humans are inherently non-linear, and to make the simulations have high fidelity, the n, which can also be seen as a noise term is obtained by multiplying zero-mean Gaussian white noise W with the remnant transfer function $H_n(s)$ as seen in Figure 2.2.

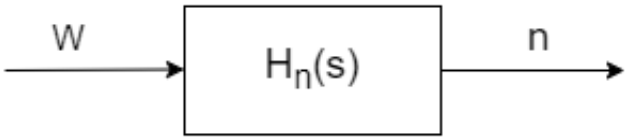

Figure 2.2: Remnant signal

Here, while there have been multiple attempts at modelling the remnant signal, there is still no consensus on how to model the remnant transfer function $H_n(s)$. Studies conducted [6, 7, 13] suggest that the remnant transfer function should have the structure given by [14], which defines the structure to be that of Equation 2.3 with $m = 1$. This model structure has also been verified based on the ratio of remnant signal power to control signal power in [15].

$$H_n(s,t) = \frac{K_n}{(T_n s + 1)^m} \tag{2.3}$$

With, K_n being the remnant gain and T_n the time constant. In order to decide on the order of the remnant transfer function, van Grootheest et. al in [16] conducted Monte-Carlo simulations. The paper decided on the selection of $H_n(s)$ by analyzing the performance of different $H_n(s)$ orders on a set of benchmark functions. Based on the results, they found that the second-order $H_n(s)$ provided the best trade-off between accuracy and complexity. Furthermore, they observed that higher-order H_n can lead to overfitting, while lower-order $H_n(s)$ can result in underfitting. Therefore, they concluded that the second-order $H_n(s)$ is the most suitable choice for practical applications. Hence, Equation 2.2 with the addition of Equation 2.3 of the second order gives the entire pilot model. This precision model developed by McRuer only works for compensatory tracking tasks and does not describe the adaptive control behaviour of the human pilot but rather only caters to fixed dynamics of the controlled element. Later on, Section 2.2 talks about the adaptive control behaviour.

2.1.3. Controlled Element

The controlled element (CE) fits after the pilot's block in Figure 2.1 and represents the inherent dynamics of the vehicle, i.e., the aircraft in our case. Ever since the pioneering work of Tustin [17] and Elkind [18] in the field of manual control, many types of CE transfer function $H_{CE}(s)$ have been used in simulations and experiments; these range from pure gain, single integrator and double-integrator to transfer functions which act single integrator-like, double integrator-like, etc. These controlled elements are linked to typical aircraft control tasks; Table 2.1 taken from [7] shows relevant vehicle control tasks and their representative CE dynamics.

2.1.4. Display types

The term "display" pertains to the visual rendering of available information sources. The interpretation of this information by the human controller (HC) depends on the manner in which it is displayed. In manual control tasks, three types of displays are used, namely, compensatory, pursuit and preview. As preview display is beyond the scope of this project, it will not be discussed. Figure 2.3 shows both, the compensatory and the pursuit displays.

Table 2.1: Typical aircraft control tasks and related simple controlled element [7]

Controlled Element	Related Vehicle Control Situation
$Y_c = K_c$	Aircraft load factor control (at high speeds) by elevator
$Y_c = \frac{K_c}{s}$	Aircraft pitch angle control by elevator / Attitude control of vehicles with augmented damping / Automobile heading control by steering wheel
$Y_c = \frac{K_c}{s^2}$	Space vehicle attitude control by control jets / Rocket booster control (at launch) by thrust deflection / Aircraft heading control by ailerons
$Y_c = \frac{K_c}{s(s+1/T)}$	Aircraft roll angle control by ailerons / V/STOL thrust translation control (at hover) by thrust deflection
$Y_c = \frac{K_c}{(s-1/T)}$	Pitch angle control of a statically unstable aircraft by elevator
$Y_c = \frac{1}{s(s-1/T)}$	Unstable rocket booster control (at high dynamic pressure) by thrust deflection

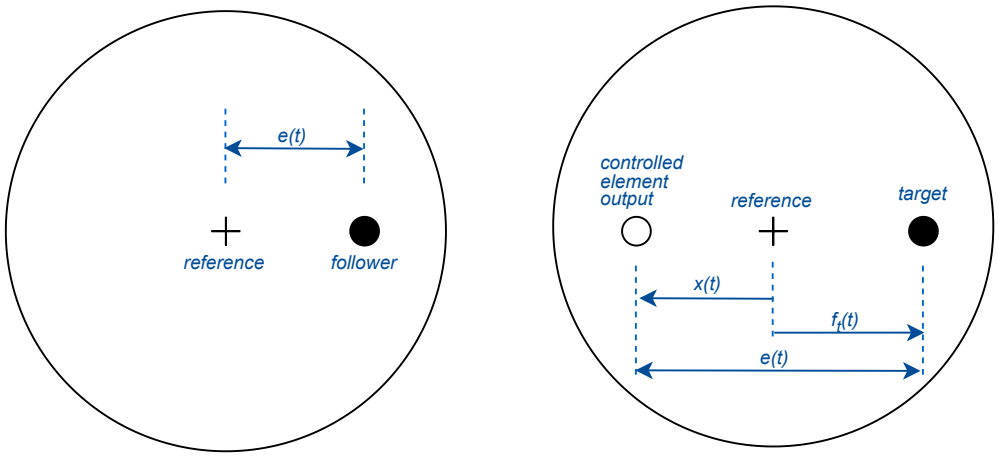

(a) Compensatory Display

(b) Pursuit Display

Figure 2.3: Compensatory and Pursuit displays

In compensatory (C) displays, only the error signal, i.e., the difference between the system response $x(t)$ and target signal $f_t(t)$ is shown. By doing so the human controller tries to minimize the error by giving input via a manipulator and keeping the follower (ideally) on the reference mark in the centre of the display. In the case of pursuit (P) displays, the system response $x(t)$, the target signal $f_t(t)$ and the error $e(t)$, all three are shown. It is to be noted that the error signal is shown as the difference between the response and the target ($e(t) = f_t(t) - x(t)$). As a result, the pursuit tracking task takes a different form of control structure which is shown in Figure 2.4.

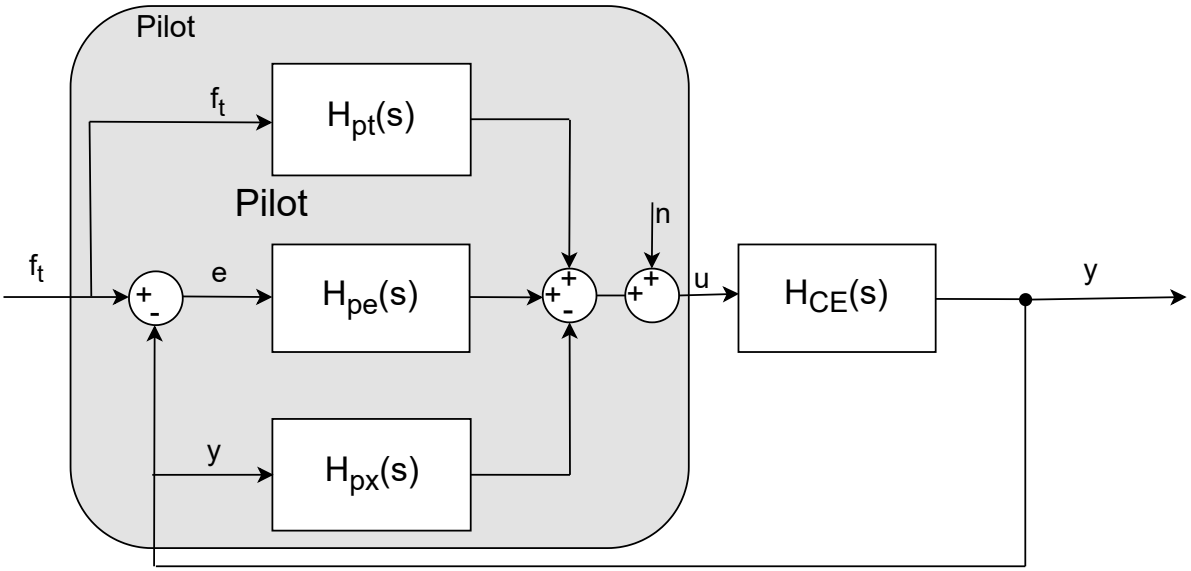

Figure 2.4: Pursuit tracking task

While compensatory control behaviour, where the operator controls based only on feedback of a "tracking error" shown on the display, is reasonably well understood and a number of highly useful models for human operator's compensatory control dynamics are available [7, 19], the modelling of HC behaviour in pursuit tracking tasks has received meagre attention. The main reason is that the multi-loop control behaviour in pursuit makes its modelling significantly more complicated. As seen above, a pursuit configuration yields three different describing functions, as a result, HCs may choose to mechanize feedforward and/or feedback control responses driven by the $e(t)$, $f_t(t)$ and $x(t)$ signals, however, as $e(t) = f_t(t) - x(t)$, only two of the three possible HC responses are independent, resulting in an inherently over-determined model structure [2]. Hence, for pursuit tasks various model structures have been proposed and applied [20].

2.1.5. Crossover model

The culmination of Section 2.1.1, Section 2.1.2, Section 2.1.3 and Section 2.1.4 is the manual tracking task. One of the most important models of this setup is McRuer's *crossover model* [4] which pertains to a compensatory target-tracking task and explains the pilot's adaptation to CE dynamics as seen in Equation 2.4. This finding states that the pilot adapts his/her control behaviour to the CE dynamics such that the open-loop response of the combined pilot-vehicle system near the crossover frequency ω_c (i.e., where $|Y_{OL}(j\omega)|_{\omega=\omega_c} = 1$) behaves like a single-integrator.

$$Y_{OL} = Y_p(j\omega)Y_c(j\omega) = \frac{\omega_c}{j\omega}e^{-j\omega\tau_e} \tag{2.4}$$

That is, the pilot adjusts their behaviour such that the slope of the magnitude of open-loop dynamics is $-20dB/decade$ in and around the crossover region. It can be seen from Equation 2.4 that this model takes only the linear part of the pilot as it uses a simplified precision model that accounts for the effective time delay but does not take into consideration, the NMS transfer function. As this model is used as a reference for pilot modelling to date, the study carried out in this thesis will also use this model to obtain initial simulations with the addition of the NMS and the non-linear time-varying part of the pilot by including the remnant. Lastly, the use of the crossover model in this study will be in obtaining the phase margins as a function of time of the time-varying open-loop (OL) dynamics; as a result, it becomes important to define and understand the concept of phase margins, denoted by ϕ_m.

Phase margin is a critical concept in control theory, particularly when analyzing and designing control systems. Mathematically, ϕ_m is defined as the difference between the phase ϕ of the system and $-180°$ at the gain crossover frequency (ω_{cg}), i.e., the frequency at which the gain of the system is equal to 1 ($0dB$).

$$\phi_m = \phi - (-180^\circ) \tag{2.5}$$

Typically in control systems, the phase lag varies with frequency and progressively deteriorates to eventually become and/or cross -180° where the output of the system becomes inverted, i.e $\frac{o/p}{i/p} = -1$, at this point using Equation 2.5, the phase margin becomes ≤ 0 and the system is said to be unstable. In other words, having a positive phase margin is a measure of the system's stability. An example of the positive phase margin of an arbitrary system is shown in Figure 2.5 to represent how the phase margin is calculated in this study using bode plots.

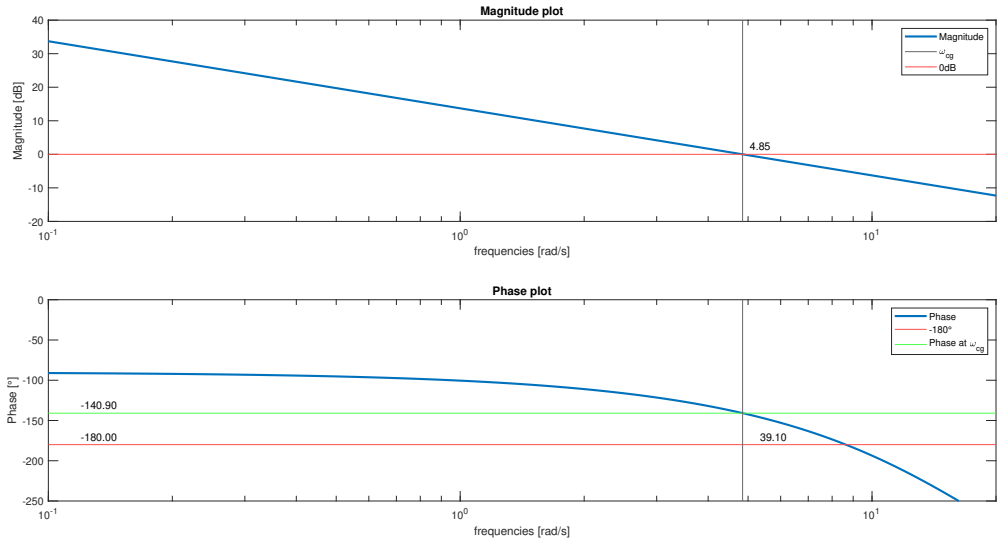

Figure 2.5: Capturing the phase margin (ϕ_m)

Consequently, if the system is changing with time, then at each time step, the above process can be carried out to capture the phase margin of the system to obtain phase margin as a function of time. This will be seen later on in Section 3.0.2.

Now, having a global picture of manual control tasks and their components, the next section discusses relevant research carried out in this field with an emphasis on time-varying control tasks followed by their findings.

2.2. Review of Past Research

Quoting McRuer and Jex [7]: "The human pilot is a multimode, adaptive, learning controller capable of exhibiting an enormous variety of behaviour". The ability of the human controller (HC) to adapt to – and learn from interactions with – the environment is phenomenal and makes the study of HC behaviour a fundamental challenge. One of the first reported experiments on ***adaptive human behaviour*** was conducted by Young et al. [21]; Young conducted an experimental investigation using changes in gains and polarity of the controlled element (CE) with position control (pure gain control) to determine lower bounds on the adaptation process and employed C as well as P displays. In this experiment, the tracking error and time histories of HO response were used to determine pilot-model structure. They concluded that the adaptation process should be considered to have three phases, namely, *detection*, which deals with the recognition that the CE dynamics have changed; *identification*, which indicates an occurrence of change is a response and; lastly, *adjustment*, which encompasses reduction of error following the identification phase. Here, *adaptation* encompasses both, the detection and identification phases of the human controller.

Sadoff's study (1962) emphasizes the requirement of these experiments, stating that aircrafts should be designed so that when the Stability Augmentation System (SAS) is inoperative or has failed, the vehicle dynamics should still be acceptable by the pilot [22]. This study was one of the first to state that pilot rating boundaries had only been established for time-invariant CE dynamics. Hence, the focus had to be shifted to sudden changes in CE dynamics, like SAS failures. Subsequently, many studies took place for time-varying CE dynamics.

One such paper that resonates with McRuer and Jex's review paper [7] is McDonnell's paper that investigated the change in pilot behaviour given a sudden change in the CE dynamics [23]. In his paper, McDonnell carried out an experiment using compensatory displays for a single-axis lateral movement (roll) tracking task where the CE dynamics switched from CE_1 to CE_2 using a step function, which is representative of augmenter failures and control power changes as a result of surface actuator failure. The forcing function was a multi-sine consisting of a sum of four sinusoids of equal amplitude with random phases and different frequencies. They hypothesized that after the CE dynamics had changed, one of the two conditions would prevail, i.e.:

1. The new closed-loop system would be stable
2. The new closed-loop system would be unstable until some operator adjustment was made

The study states that the use of McRuer's crossover model may be considered an average description of the pilot's behaviour but fails to describe the operator's output at every instant of time, however, it still allows for stability to be assessed. One unique trait of this experiment was the availability of a button on the control stick that the operator would press when they recognized a change in the CE dynamics that they were trying to control. As a result, a time difference (Recognition time t_r) between when the CE actually changed and when the pilot recognized this change could be obtained and used for post-analysis and had a direct implication of the operator's ability to detect a change and take corrective action, for example, disengaging a failed augmentation system. In all these studies mentioned above, the display type being used was a compensatory display; Wasicko et al.(1966) in their study, titled, "Human Pilot Dynamic Response in Single-loop Systems with Compensatory and Pursuit Displays" compared the pilot's response to time-invariant CE dynamics when using different displays for single axis (roll) tracking tasks [24]. The CE dynamics that they tested were: $K_c, K_c/s, K_c/s^2, K_c/s(s-\lambda)$($\lambda$ = variable pole) and $K_c(s+0.25)/(s+5)^2$ with the forcing function made up of a rectangular signal spectrum. The outcome of this experiment gave a clear comparison of the pilot's performance and error using the two displays. Table 2.2 lists the important results of this study while the following list details the important implications mentioned in the paper.

- *"It is important to recognize that presentation of the signals does not necessarily imply pilot action thereon; for instance, in a pursuit display the operator may act only on the error, thereby performing a compensatory fashion despite the presence of the forcing function and output."*
- *"Conversely, under certain conditions with a compensatory display (e.g., a predictable forcing function) the operator can mentally separate input from output in the displayed error signal. Then by using a reasonable facsimile of the system forcing function and the error as information inputs the operator may function in a pursuit fashion."*
- *"The usual way of inducing compensatory or pursuit behaviour is using a display and random-appearing inputs."*

- A key feature of the experimental program reported here is that comparisons were also made in terms of the effective open-loop describing function, y_β, which reveals the dynamic effects of the pilot's system organization and is given below where, subscripts i, e and m represent the three pursuit display describing functions of input, error and output as seen in Figure 2.4:

$$Y_\beta = \frac{\Phi_{im}}{\Phi_{ie}} = \frac{Y_c\left(Y_{p_i} + Y_{p_e}\right)}{1 - Y_c\left(Y_{p_m} + Y_{p_i}\right)}$$

- *"For pursuit display tracking, the actual block diagram structure adopted by the operator, i.e., the system parameters used to generate his output, is not known, nor is there any knowledge that the same block diagram structure exists for all inputs and controlled elements."*

Controlled Element	Result
$Y_c = K_c$	P is better than C for low bandwidth inputs and performance becomes the same for high bandwidth input
$Y_c = \frac{K_c}{s}$	C is slightly better at low and high bandwidth inputs with essentially no difference for moderate bandwidth inputs
$Y_c = \frac{K_c}{s^2}$	P is increasingly better than C
$Y_c = \frac{K_c}{s(s-\lambda)}$	P is increasingly better than C as λ increases.
$Y_c = \frac{K_c(s+0.25)}{(s+5)^2}$	For the bandwidths tested there is no significant difference between displays

Table 2.2: Results of better performance based on CE and type of display [24]

In 1969, Phatak and Bekey proposed a model for compensatory tracking tasks such that it captured the adaptive behaviour of the pilot called the 'Supervisory Control Model' [25]. This model was based on the knowledge that the human operator detects change based on a large differential change in the error and error rate. This model is considered to be a promising framework and was found to be limited due to the lack of standardized limits independent of the CE dynamics being used as found by Van Ham et al. at the Department of Control and Simulation, TU Delft [26].

The research of Johnson et al. had a very clear and specific aim to understand the effects of time-varying CE dynamics as the pilot adapts to these dynamics where, they found that their hypothesis of graceful degradation was true, i.e., a flight control system design that gives less change in the effective CE dynamics post failure results in better tracking performance. Here, the SAS/Flight Control System(FCS) failure is the representation of why the CE dynamics change [27]. It is to be noted that, this literature study deliberately limits itself to the explorations and discussions of manual control in single-loop tasks and avoids detailed explanations other than vital insights from multi-loop tasks because it is a known fact that model identification and model validation become complex and intricate in multi-loop situations [28].

One such study was carried out by Hess in which he ran multiple simulations using both, a multi-loop (pursuit-like) pilot identification procedure for single and two axes tracking tasks. In his tracking task loop, the inner loop was set to be a rate control loop which was considered to be the primary adaptation loop while the outer loop was hypothesized to provide a vernier adjustment to improve the pilot's tracking performance. The CE dynamics used were varied gradually as well as suddenly to capture fast and slow adaptations of the pilot in these simulations. The conclusion of this study suggested a pilot model can be structured to have two loops in case of pursuit tasks and that the obtained model provides a framework that could help study pilot control behaviour in cases of sudden CE-dynamic changes [29]. Following this, Hess conducted another study in 2011 to provide a preliminary understanding of the dynamics of human pilots controlling systems with time-varying dynamics. In this study, he used a single subject and a pursuit tracking task with changing CE dynamics and discussed a procedure for creating a real-time, pilot-in-the-loop simulation environment using Simulink [30]. As seen in Figure 2.6, the gains of the CE dynamics were varied linearly to represent a tilt-rotor aircraft and rotorcraft with variable speed rotors as examples of systems with time-varying dynamics.

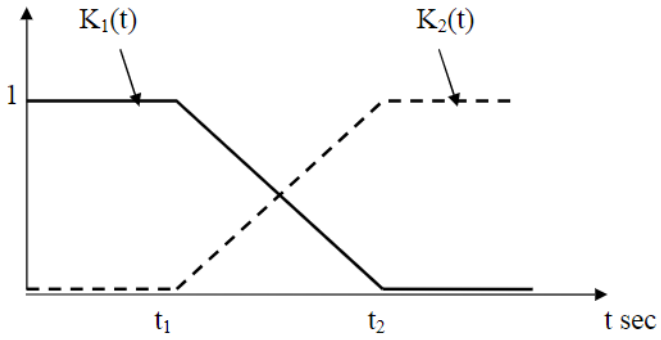

Figure 2.6: Time varying gains, Hess [30]

Identifying the pilot model is a crucial aspect of manual control. Numerous experiments are conducted to comprehend the less prominent time-invariant and generally seen time-variant behaviour of the human pilot. These experiments aim to obtain novel and more effective methods to develop complex mathematical models that describe time-varying behaviour and estimate time-varying frequency responses or time-varying model parameters. These papers use methods like ARX, Kalman filtering, wavelet transforms, etc to obtain a good parameter estimation for these models. In one such paper, Zaal and Sweet [31] proposed a Windowed Maximum Likelihood Estimation (MLE) to be used as a parameter estimation technique. The details of this experiment are as seen below in Table 2.3.

Experiment description	Estimate the parameters of a pilot model with time-dependent sigmoid functions to characterize time-varying human control behaviour.
Task	Multi-axis (pitch and roll) tracking task
Display	Compensatory
CE dynamics	$\frac{90}{s(s+6)}$ to $\frac{30}{s(s+0.2)}$ using a sigmoid function with $G = 0.5$ and $100s^{-1}$
Task time	$T = 90s$ and $T_{measured} = 81.92s$
Forcing functions	Multi-sine forcing function with 10 sinusoids
Participants	9 general aviation pilots, all male. The average age was 24.3 years old. All of the pilots were right-handed. Only one had prior experience with the type of control task in question.

Table 2.3: Experiment overview, Zaal et al. [6]

The NMS transfer function used was the same as mentioned previously in Equation 2.2 with $\zeta_{nm} = 0.20$ and $\omega_{nm} = 10rad/s$ with the effective time delay kept constant at $\tau_e = 0.20s$. A very similar paper was published by the same authors which serves as a justification for using MLE instead of wavelet transform (inspired by the use of this method as used in [32] and [33]) in [31]. In this paper published by Zaal and Sweet, simulations were used, which gave an insight that the pilot's frequency response and model parameters were less affected by remnant if MLE was used, however, more studies would be required to understand the effect of time-window length on these estimation results [6].

A study conducted at TU Delft by Pool et al. is also an example of various methods being proposed for pilot model identification. In this paper [34], a successful approach to modelling the non-linear portion of the human pilot has been discussed. This paper uses MLE and utilizes Genetic Algorithm (GA) for the identification of the non-linear terms. The method was applied to vestibular motion thresholds for previously obtained tracking data. Many such papers on pilot modelling and identification, both in time and frequency domain exist [35, 36, 37, 38, 39, 40, 41, 42, 43]. As the research question deals with identifying stability regions, the modelling and identification of pilot models is used as an inspiration for experiments and simulations with the literature study restricted on its details.

Furthermore, Zaal et al. in a study involving a multi-axis tracking task looked into the influence of motion

gains on tracking performance. The experiment details are shown in Table 2.4.

Experiment description	To understand the effect of motion gains on pilot tracking performance
Task	Multi-axis (pitch and roll) tracking task
Display	Compensatory
CE dynamics	$\frac{30}{s(s+0.2)}$ for both axes; using a sigmoid function to change motion filter gain
Task time	$T = 90s$ and $T_{measured} = 81.92s$
Forcing functions	Multi-sine forcing function with 10 sinusoids
Participants	8 subjects. Students and staff at TU Delft with extensive experience in manual tracking tasks.

Table 2.4: Experiment overview, Zaal et al. [44]

The study concluded that pilots modified their equalisation dynamics in the same axis when the roll or pitch motion filter gains were increased, improving tracking performance. Pilots adjusted their equalisation dynamics in the opposite direction when motion filter gains were reduced, which reduced tracking performance. These modifications in tracking behaviour were discovered to be comparable to those seen in single-axis tracking tasks with various gains from static motion cues. Indicators of minor cross-coupling between the pitch and roll axes were also discovered by the study [44]. This paper also gives insights into choosing relevant forcing functions such that they cover the complete frequency range of human control with regular intervals on a logarithmic scale; the forcing functions used here have also been used in a number of other experiments proving their quality [6, 31, 45, 46, 47]. Here, four sets of phases were chosen for the target and disturbance signals in the pitch and roll axes, yielding signals with an approximately Gaussian distribution and an average crest factor, as well as an average crest factor for the signal's first and second derivatives.

In 2014, based on simulations, Hess proposed an adaptive pilot model for pursuit tracking tasks for time-varying CE dynamics, representing loss of control events, which was able to capture similar behaviour as expected near the crossover frequency as detailed by McRuer (mentioned in Section 2.1.5) and was able to recreate Pilot Induced Oscillations (PIOs) which is typical of LOC-I events. The NMS transfer function used the parameter values of $\zeta_{nm} = 0.707$ and $\omega_{nm} = 10rad/s$ [36]. This paper was later used in Hess's study of further simulations depicting real-world scenarios, namely, a single-axis control task, a rotorcraft control task, a multiaxis GTM (vehicle model) control task, PIO simulation, aircraft departure from controlled flight (GTM model) and a rudder reversal PIO scenario. The adaptive model was able to capture both, gradual failure and sudden failures of the aircraft. It successfully captures multiaxis control task behaviours as well as PIOs leading to a conclusion that the model could be used for an assessment of adaptive or robust flight control systems with time-varying (TV) CE dynamics and to model pilot behaviour in LOC-I events [37]. Similarly, a model for preview tracking tasks based on empirical results has also been proposed by van der El et al. at TU Delft [42].

Mulder et al. in their review paper summarizing the fundamental limitations in current manual control and cybernetics provide a road map for the required shift from LTI models to linear parameter-varying systems. In this paper, the primary limitation of using the assumption of time-invariance is stated as the inability induced by this assumption to model the ability of human controllers to *adapt*. Moreover, this paper limits the discussion to single-axis control tasks with displays, which is also the main interest of this thesis. While mentioning the limitations of compensatory tasks, the review talks about the requirement of keeping forcing functions quasi-random so as to avoid any non-linear behaviour that the pilot may display in case of predictability or anticipation; the same problem is faced for the case of remnants where humans have to be trained before experiments to obtain linear operator behaviours given the current inability for a widely accepted remnant model. Mulder et al. also detail the limitations of pursuit task modelling problems given its over-determined structure and the ability of the pilot to use six possible strategies. A proposal is then made to apply novel closed-loop identification techniques for Linear Parameter-Varying (LPV) systems so as to identify time-varying (TV) manual control models, for which, they mention, **"A possible approach would be to systematically change the main task variables (P and T), use extensive computer**

simulations to explore how the HC may adapt, assuming optimality, and validate these findings through experiments." where P and T are the forcing function and CE dynamics respectively [3]. This statement resonates strongly with the research question proposed in this thesis.

Zaal, in yet another study, studies manual control adaptation in multi-axis tasks with time-varying (TV) CE dynamics. Using the same set of subjects from before, i.e., [6]. In this study (details mentioned in Table 2.5), he checks for cross-coupling between the two axes and how changing CE dynamics in a specific axis affected the other axis performance and the overall performance [48].

Experiment description	To study manual control adaptation to changing controlled element dynamics in roll-pitch control tasks.
Task	Multi-axis (pitch and roll) tracking task
Display	Compensatory
CE dynamics	$\frac{90}{s(s+6)}$ to $\frac{30}{s(s+0.2)}$ using a sigmoid function with $G = 0.5$ and $100s^{-1}$
Task time	$T = 90s$ and $T_{measured} = 81.92s$
Forcing functions	Multi-sine forcing function with 10 sinusoids, same as used in [31]
Participants	9 general aviation pilots, all male. The average age was 24.3 years old. All of the pilots were right-handed. Only one had prior experience with the type of control task in question.

Table 2.5: Experiment overview, Zaal [48]

The transition function used in this case, is the same as before, i.e., the sigmoid function. This paper based the transition function's selection on the assumption that the parameter function used for time-varying pilot model parameters was equivalent to the parameter function used to vary the CE dynamics in time. The change in CE dynamics was explained as changing conditions like flight mode transitions and adaptive fly-by-wire control laws. The pilot model was extracted using a time-domain parameter estimation technique, MLE. The results obtained based on the hypotheses of this study are summarized below:

- Both roll and pitch axis tracking performance were affected by changing CE dynamics and by the rate of change of these dynamics, i.e., G value. Though more change was seen in the axis that experienced the CE change, cross-coupling effects were also observed.
- As obtained theoretically from VAR, as the CE transitioned from single integrator-like to double integrator-like, the pilot gains decreased and the visual lead increased.
- Pilot performance was better and control activity was lower in the pitch axis even though equivalent dynamics were used for both axes.

In recent years, efforts of pilot identification, system analysis and pilot modelling have continued. M. Jirgl et al. carried out an experiment to study human adaptability in Man-Machine Systems (MMS) using a flight simulator running the X-PLANE 10 software with a simulated step-change in the aircraft models' altitude [49]. A comparison of pilot model parameters was made based on experiments conducted using the same subjects 6 months apart with the result indicating that the average reaction delay had decreased indicating a positive change. This study used MATLAB's *System Identification Toolbox* for parameter estimations and statistical tests like mean, variance, standard deviation, coefficient of variation, skewness and kurtosis to comment on the comparison made. Similarly, for pilot model identification, van Grootheest et al. (2019) used recursive ARX models for compensatory tracking tasks [16]. The details of this analytical study are shown in Table 2.6.

As this was a simulation-based study the pilot models were developed for CE_1 and CE_2 based on the Verbal Adjustment Rules (VAR). The resultant pilot models along with open-loop(OL) crossover frequency and phase margin were obtained as seen in Table 2.7.

The outcome of this study showed that ARX models were successfully able to model the human pilot given a good tuning of the forgetting factor and adjustment of the remnant intensity levels. It was concluded that this model identification method could also be used for HC monitoring and adaptive support systems.

Experiment description	To use ARX models to identify adaptations of a simulated time-varying pilot model.
Task	Single axis $\cdot_{\cdot}^{\cdot}$ simulations used single-axis time-varying (TV) CE
Display	Compensatory
CE dynamics	$\frac{90}{s(s+6)}$ to $\frac{30}{s(s+0.2)}$ using a sigmoid function with $G = 0.5$ and $100s^{-1}$
Task time	$T = 90s$ and $T_{measured} = 81.92s$ with total recording time $T_r = 8T_{measured}$
Forcing functions	Multi-sine forcing function with 10 sinusoids, same as used in [31, 48]

Table 2.6: Experiment overview, van Grootheest et al. [16]

	CE		HO						HO × CE	
State	K_c $[-]$	ω_b $[rad/s]$	K_e $[-]$	T_L $[s]$	$K_{\dot{e}}$ $[s]$	τ_e $[s]$	ω_{nm} $[rad/s]$	ζ_{nm} $[-]$	ω_c $[rad/s]$	ϕ_m $[°]$
1	90	6	0.09	0.4	0.036	0.28	11.25	0.35	1.5	77.0
2	30	0.2	0.07	1.2	0.084	0.28	11.25	0.35	2.8	22.7

Table 2.7: Pilot model details van Grootheest et al. [16]

Mulder et al. in their detailed study of pursuit display [20] build on the statements of their preceding papers: [2] and [3], which mentioned the limitations of the crossover model given its time-invariant characteristics and the limited applicability covering only compensatory displays. This study is taken as a reference for the details of the pursuit tracking task given the variety of strategies it offers based on the explicit presentation of both, the target signal and the system output. Given that previously mentioned research supports pursuit displays, as they have proved to be better for double integrator-like CE dynamics when compared to compensatory displays, Mulder et al. argue for the requirement of time-varying (TV) systems as skilled operators can learn to characterize the probabilistic nature of tracking tasks which inherently makes them non-linear controllers making their behaviour beyond the scope of current LTI models. That is, because the forcing function f_t is shown separately in pursuit displays, the HC may learn its properties and use it to predict its behaviour; with simpler signals like the single integrator this becomes easier to do [50, 51]. It is presented that as the output of the system x is also explicitly visible, the HC may be able to see the first $\dot{x}$ and sometimes the second derivative $\ddot{x}$ making it easier for difficult CE dynamics to be controlled.

As stated in [24], the HC has three inputs in a pursuit display, namely, f_t, e and x, with the relation of $e = f_t - x$, which enables the HC to choose either a feedforward or a feedback control strategy with the drawback of the model being its over-determined structure. It is further argued that the HC is sure to understand these characteristics of the forcing function and to use them to improve their tracking performance. To explore this idea, a normally distributed forcing function is taken into consideration and given that in tracking tasks, the f_t signal does not leave the screen, a probabilistic perspective on the HC's behaviour is developed. The summarized argument is that given the characteristics of the forcing function when the f_t is at the right end of the screen, the HC will control the system output x knowing that f_t won't go more to the right but rather towards the centre and vice versa. The HC will use this knowledge in their control behaviour, making it time-varying and non-linear. Figure 2.7 shows this probabilistic view.

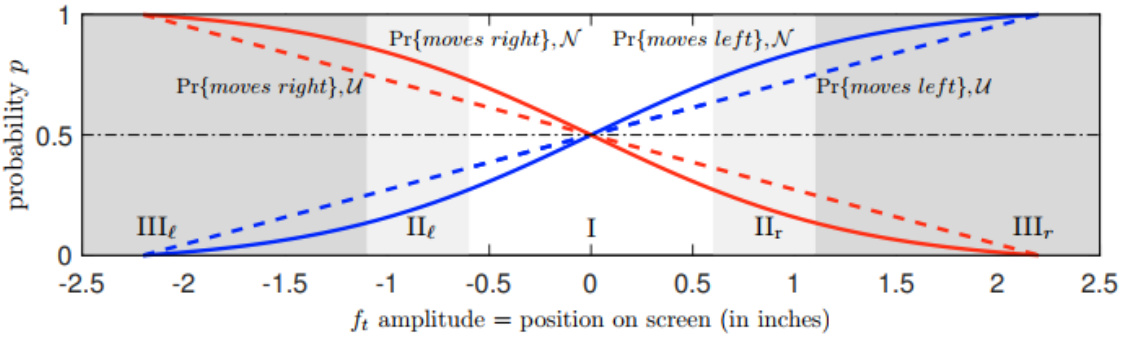

Figure 2.7: Probabilistic view of HC behaviour in pursuit tracking [20]

In 2019, Plaetinck et al. in their endeavour of pilot identification in situations of sudden loss of stability used a very similar approach as Grootheest et al. [16] of ARX models. Specifically, a low-order recursive ARX identification with two detection methods - Time-Invariant Condition Average (TICA) and Moving Average (MA) [35]. The details of this experiment are shown in Table 2.8.

Experiment description	To use low-order recursive ARX identification method to identify pilot models in sudden loss of stability events.
Task	Single axis (pitch control)
Display	Compensatory
CE dynamics	time-varying: $H_c(s,t) = \frac{k_c(t)}{s(s+\omega_b(t))}$ using a sigmoid function with $G = 0.5$ and $100s^{-1}$
Task time	$T_{measured} = 81.92s$ with preceding run-in time varied between $5s, 10s$ and $15s$
Forcing functions	Multi-sine forcing function with 10 sinusoids, same as used in [31, 48, 16]
Participants	8 skilled participants

Table 2.8: Experiment overview, Plaetinck et al. [35]

The study found that using the pilot error response gain $K_{\dot{e}}$ was the most reliable parameter for adaptation detection. Moreover, the TICA method, which is based on comparing pilot behaviour with existing data of non-adaptive pilot behaviour was a better method than MA, which uses the moving average of past $K_{\dot{e}}$ trace itself.

Adding to studies conducted lately, Terenzi et al. at TU Delft used a model-based adaptive control technique, Model Reference Adaptive Control (MRAC) in their experiment to describe the adaptive behaviour of the HC in pursuit tracking tasks [52]. Model Reference Adaptive Control (MRAC) is an adaptive control technique that employs an internal model to facilitate controller adaptation in response to changing task conditions. It functions by contrasting the anticipated output of the internal model with the observed output and subsequently adjusting the controller parameters based on the disparities between them. The adaptation of the controller parameters is instigated by the mismatch between the predicted and observed outputs. MRAC encompasses both a feedforward and a feedback controller, along with an internal reference model. The internal model is employed to establish the ideal control policy independently of the controlled dynamics. By continuously updating the control gains and internal model parameters, MRAC can emulate human adaptation in pursuit tracking tasks when there is a modification in the dynamics of the controlled system. The experimental details can be seen below.

It was found that the current MRAC model can approximate human adaptation in pursuit tracking tasks when there is a change in the dynamics of the controlled system that requires significant feedback controller adaptation. However, the MRAC model's accuracy in predicting human control adaptation is limited, particularly for transitions from double to single integrator dynamics. The study also found that using

Experiment description	To evaluate the effectiveness of a model-based adaptive control technique, Model Reference Adaptive Control (MRAC), for the adaptive controller.
Task	Single axis (pitch control)
Display	Pursuit
CE dynamics	time-varying: $H_c(s,t) = \frac{k_c(t)}{s(s+\omega_b(t))}$ using a sigmoid function with $G = 100$
Task time	$T_{measured} = 90s$
Forcing functions	Multi-sine forcing function with 10 sinusoids
Participants	10 participants. Wherein, 7 were male and 3 were females. No prior tracking experience except for 2 subjects.

Table 2.9: Experiment overview, Terenzi et al. [52]

transition-specific learning rates improved the adaptation of the MRAC model's control gains for different types of transitions.

In 2022, Mulder et al. considered a probabilistic perspective for manual control by investigating probability densities of tracking error signal e [53]. The inspiration behind this study was to obtain the ability to differentiate control behaviour based on the type of tracking task, namely, compensatory, pursuit and preview because current models average out the time domain signals and hence lose out on task-specific behaviours. This paper used Van der El et al. [54] experimental data and the probabilistic view presented in Mulder et al. [20] and proved that HCs indeed use such strategies, especially for pursuit displays and that these effects became stronger for higher target signal bandwidths. The error signal densities plotted for all three tracking tasks showed an increase in tracking performance moving in the order of compensatory $\rightarrow$ pursuit $\rightarrow$ preview.

Furthermore, Jakimovska et. al very recently in 2023 presented an analysis and validation effort for the Hess Adaptive Pilot Model (HAPM), which aimed to model human operator's control adaptations in pursuit tracking tasks. The Hess Adaptive Pilot Model includes a mathematical framework to predict when pilots may trigger an adaptation of their control behaviour and to predict realistic adaptations of pilot control gains. The authors replicated the simulation results reported by Hess to verify the model implementation and then made adjustments to the model, such as adding a human operator delay, to fit it to the experiment data. The experiment data used in the study were obtained from a previous experiment conducted at TU Delft, where participants performed a pursuit tracking task with transitions in controlled element dynamics. The results show that the model accurately describes the measured steady-state tracking behaviour for the participants in the data set. It was also able to capture the transient control behaviour during transitions in controlled element dynamics. However, some modifications and simplifications were required to achieve an accurate fit to the data, such as adding a human operator delay and re-tuning the adaptive logic's low-pass filters.

2.3. Conclusions

The main conclusion drawn from existing state-of-the-art research in the field of manual control is the need to better understand and explore the detection phase of the adaptive human controller. Multiple attempts to model the human pilot were studied throughout the literature [1, 4, 14, 19, 21, 24, 25, 36, 38, 39, 40, 42] and many others to estimate as well as identify human control behaviour in both, cases of time-invariant conditions and in time-variant condition using a plethora of techniques [6, 9, 16, 22, 23, 26, 27, 28, 29, 30, 31, 32, 34, 35, 37, 43, 44, 48, 52, 55, 56, 57, 58]. Throughout these attempts, many forcing functions f_t, pilot dynamics H_p, remnant models H_r, controlled element dynamics H_{CE} and displays (compensatory, pursuit and preview) were utilized and scrutinized to better understand human role in manual control tasks. Having done so, the field of manual control can be seen to have matured rapidly with time and to be ever-developing. However, this study finds a gap in the knowledge of adaptive pilot behaviour to be concerning; as consistently emphasized by [2, 3] attempts to develop an understanding given the sharpened tools of this field, i.e., between adaptive pilot modelling attempts and identification pursuits, the understanding of this adaptive behaviour in time-varying scenarios needs to be improved equally.

Real-world scenarios in which human controllers (HCs) are compelled to adjust their control behaviours include instances of time-varying alterations in the dynamics of the controlled system, sudden changes in task constraints, loss of control events, and transitions from automatic to manual control modes. These adaptations by HCs to time-varying conditions are inherently marked by high variability, non-linearity, short duration, and strong task-specific dependencies, rendering them significantly more complex to grasp than linear time-invariant (LTI) HC behaviour [2].

Siting this gap of knowledge, a study will be undertaken, which will utilize current models and tracking task knowledge to analyse how the adaptive behaviour of the human controller shapes the open-loop dynamics for time-varying conditions. An intensive study will be done for time-varying vehicle dynamics to see if the combined dynamics have temporal instability when the pilot adapts to the changing CE dynamics. These regions of instability will be further analysed to check if the pilot uses their existence to detect the change in CE dynamics which will shed light on the detection phase of the adaptive control behaviour. This will eventually help develop pilot training procedures; personalised support systems and improve Stability Augmentation Systems (SAS). Consequently, Chapter 3 details the research methodology used and the preliminary simulations developed to identify these regions of open-loop instability.

3

Preliminary Simulations

This chapter deals with an initial set of simulations that serve as a foundation for the first research phase that deals with extensive simulations encompassing multiple parameters. A set of preliminary simulations are presented to show the adaptive behaviour of the pilot for time-varying controlled element dynamics. The focus of these simulations lies in compensatory tracking tasks as a universally accepted model for this task exists [4]. Simulations were conducted in MATLAB and Simulink wherein all the parameters and variables of a compensatory tracking task seen in Figure 2.1 are selected/derived as elaborated below.

3.0.1. Simulation setup

Forcing function

A typical selection/design of forcing functions is by the use of multisine signals given their quasi-random behaviour that helps with linear pilot behaviour as well as in frequency domain identification techniques [8]. A multisine forcing function f_t, which is a sum of sine waves is used in the simulations. Equation 3.1 shows the general structure of these forcing functions.

$$f_t = \sum_{n=1}^{10} A_t[n] \sin\left(\omega_t[n]t + \phi_t[n]\right) \tag{3.1}$$

Where $A_t[n]$ is the amplitude of the nth sinusoid with $\omega_t[n]$ the frequency and $\phi_t[n]$ the phase of that sinusoid. In the current simulations, 10 sine waves have been used ($n = 10$) as shown in Table 3.1. This set of 10 sine waves used in our simulations are the same as used by Terenzi et al.[52]; the reason behind using this set is to have homogeneity and a reference for comparison of implementation if required. It is to be noted that multiple runs and forcing functions(based on phase shift) can be simulated but for simplicity, both, the number of runs and the forcing function realizations have been kept to be unitary in the simulations.

k$[-]$	$n_t[-]$	ω_t[rad/sec]	A_t[rad]	ϕ_t[rad]
1	2	0.419	$2.905 \cdot 10^{-2}$	2.841
2	5	1.047	$1.916 \cdot 10^{-2}$	3.319
3	9	1.885	$1.020 \cdot 10^{-2}$	0.718
4	13	2.723	$6.032 \cdot 10^{-3}$	0.768
5	19	3.979	$3.356 \cdot 10^{-3}$	2.925
6	27	5.655	$1.983 \cdot 10^{-3}$	5.145
7	39	8.168	$1.230 \cdot 10^{-3}$	2.085
8	51	10.681	$9.331 \cdot 10^{-4}$	0.383
9	67	14.032	$7.541 \cdot 10^{-4}$	0.763
10	83	17.383	$6.674 \cdot 10^{-4}$	3.247

Table 3.1: Parameters of the ten sine waves used to make the forcing function

Here, the fundamental frequency is defined as $\omega_m = \frac{2\pi}{T_m}$ with T_m being the measurement time. This parameter is also kept to be in line with Terenzi's experiment and has a value of $T_m = 30s$. While the total simulation duration is 200 seconds, the measurement time is selected to be $30s$ as the frequency of all sine waves must be an integer multiple n_t of the fundamental frequency to avoid spectral leakage. Consequently, ω_m is calculated to be $0.209rad/sec$.

Lastly, note that the bandwidth used for calculations is $\omega_i = 2.723rad/sec$, which is the frequency of the fourth sinusoid of the forcing function. The selection is based on the fact that post this sinusoid, the amplitude drops considerably.

CE dynamics and transition function

The dynamics of the controlled element, while positioned downstream within the control loop of a tracking task, are fundamentally responsible for determining the control behaviour exhibited by the pilot. Hence, here, the CE dynamics H_{CE} are discussed first. As the forcing function was in line with [52], the CE dynamics are also inspired by the same paper in terms of its structure as seen in Equation 3.2.

$$H_{CE}(s,t) = \frac{K_c(t)}{s(s+\omega_b(t))} \tag{3.2}$$

Where K_c is the CE gain and ω_b is the break frequency. As the study focuses on the time-varying dynamics of the CE, a parameter function is required to simulate this time-varying behaviour. There are many mathematical functions used to simulate time transitions out of which, the sigmoid function is prominent given its rate and the moment of maximum rate can be selected as required. Equation 3.3 shows the structure of the sigmoid function, where P_1 and P_2 are the initial and final values; G is the rate of transition, i.e., it defines how quickly the transition happens and; M is the moment of maximum rate of transition, i.e., it shows where the sigmoid is centred. Figure 3.1 represents the sigmoid function with varying G values $(0.08, 0.3, 100)$ all centred at the same $M = 100s$ to show the function's behaviour.

$$P(t) = P_1 + \frac{P_2 - P_1}{1 + e^{-G(t-M)}} \tag{3.3}$$

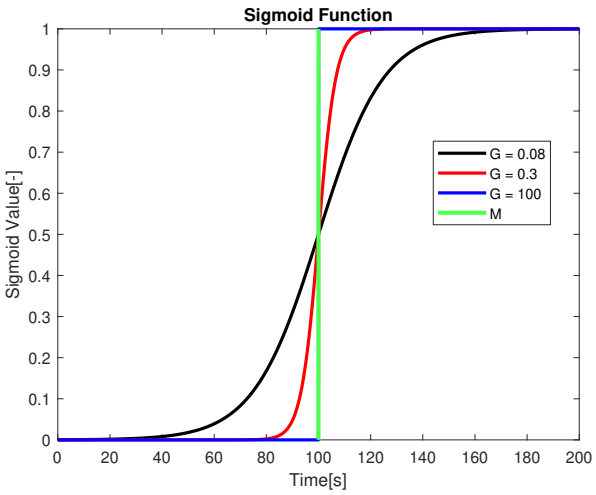

Figure 3.1: Varying Sigmoid function behaviour

Now, having defined the transition function, the CE dynamics have to be selected. In general, by varying the values of K_c and ω_b, the CE can be made to have the desired behaviour, with our focus being single integrator-like(SI) or double integrator-like(DI) dynamics. In the simulations, the CE dynamics chosen have their values selected such that the time and frequency domain outputs which will be seen in Section 3.0.2 have prominent effects for easier understanding. Essentially, the break frequency ω_b can be varied from a high value to depict a single integrator-like to a low value representing a double integrator-like dynamics.

Lastly, the reason behind choosing ω_b to be differing by a factor of 100 is to have the respective CE behaviours approximate a pure-SI and pure-DI. Table 3.2 shows the values of the CE parameters chosen for these simulations.

CE dynamics	k_c	ω_b[rad/sec]
Single integrator-like(SI)	90	20
Double integrator-like(DI)	30	0.2

Table 3.2: Parameters of the CE dynamics

Pilot Model and calculations
As the pilot aims to control the CE dynamics and adjusts his control behaviour based on the task-specific requirements; the CE dynamics are used to obtain the pilot model parameters using the Verbal adjustment Rules (VAR). The following pilot model is used to define the HC, which is a simplification over Equation 2.1:

$$H_p(s,t) = K_p(t)(\tau_L(t)s+1)e^{-s\tau_e(t)}\frac{\omega_{nm}^2}{s^2+2\zeta_{nm}\omega_{nm}s+\omega_{nm}^2} \tag{3.4}$$

In Equation 3.4, K_p is the pilot gain, τ_L the lead time generated by the pilot (as an optimal pilot is considered in the simulations, the lead time τ_L of the pilot equals the lag of the CE, i.e., the CE time constant $\tau_{CE} = \frac{1}{\omega_b}$), τ_e the effective time delay, ω_{nm} the neuromuscular frequency and ζ_{nm} the neuromuscular damping ratio. Here, the NMS parameters are kept constant and are chosen to be $\omega_{nm} = 15rad/sec$ and $\zeta_{nm} = 0.7$. The lead and lag terms, the latter being removed from Equation 3.4 as SI and DI CE dynamics don't need the lag term, are adjusted by the pilot to achieve the $-20dB/decade$ slope near the crossover region while the gain is adjusted to place the crossover frequency ω_c as required. The gain and effective time delay are the primary means by which the pilot adjusts the closed-loop stability. As McRuer didn't account for the NMS transfer function in his crossover model, minor adjustments have to be made to the parameter values obtained from the VARs. Given that the second-order NMS term induces a certain time delay to the open-loop system, this has to be accounted for such that the crossover frequency is reduced to maintain the phase margin obtained from the VARs, this is done by changing the gain, which is, adjusting the gain value to accommodate the NMS. Table 3.3 shows the values obtained for the pilot model for both, the SI dynamics and the DI dynamics. The sigmoid function is then used to transition between these pilot models.

Pilot dynamics	k_p	τ_L[sec]	τ_e[sec]	ω_{nm} [rad/sec]	ζ_{nm}
H_{p1} for SI	0.7057	0.05	0.183	15	0.7
H_{p2} for DI	0.0062	5	0.323	15	0.7

Table 3.3: Parameters of the Pilot

To this existing pilot model, another term needs to be added that represents the non-linear part of the human controller, the remnant. McRuer's pilot model was quasi-linear and hence there were no non-linearities included in that model but, as humans are inherently non-linear, a remnant term needs to be added to increase the fidelity of the simulations. As mentioned in Section 2.1.2, there exists no consensus on remnant modelling and hence as mentioned by [16], a second-order remnant structure will be taken of the form of Equation 2.3 where the time constant does not vary with time but the remnant gain K_n does. Hence, to obtain the remnant gain values for SI and DI CE dynamics, an analytical solution where the ratio of the power in control input due to noise to power in control input was taken to be 0.2 [15]. Solving this equation for K_n resulted in Equation 3.5. The gain values obtained from this equation are mentioned in Table 3.4.

$$k_n = \frac{1}{2}\cdot\sqrt{\frac{\pi\sigma_{u_{f_t}}^2}{\int_0^\infty \left|\frac{1}{1+H_p(\omega)H_c(\omega)H_{\text{del}}(\omega)}\right|^2 \left|\frac{1}{T_n(j\omega)s+1)^2}\right|^2 W(\omega)\text{d}\omega}} \tag{3.5}$$

CE dynamics	k_n[-]	T_n[sec]
Remnant for SI	0.0011	0.06
Remnant for DI	0.00059	0.06

Table 3.4: Parameters of the CE dynamics

Where $H_{del}(\omega)$ represents the effective time-delay of the pilot.

Thus, having the forcing function f_t, the pilot model H_p and the CE dynamics H_{CE} and using the sigmoid function for the latter two, a time-varying target tracking task was simulated. A MATLAB script was used to obtain the frequency domain results while a simulink model (shown in Figure 3.2, Figure 3.3, Figure 3.4 and Figure 3.5) was developed to obtain the time-domain results that are discussed briefly in the next section. An obvious characteristic of the simulations should be that the instability will occur in the transient phase of the OL and not when the combined dynamics are at a steady state, i.e., when SI-like CE dynamics are handled by H_{p1} and DI-like CE dynamics by H_{p2}. In these cases, the crossover frequency ω_c and phase margin ϕ_m will be the same obtained by the VARs. Table 3.5 shows the respective values for both CE conditions.

CE dynamics	ω_c[rad/sec]	ϕ_m[°]
OL for SI dynamics	3.17	39.14
OL for DI dynamics	2.80	22.82

Table 3.5: Crossover frequency ω_c and phase margin ϕ_m for the open-loop dynamics

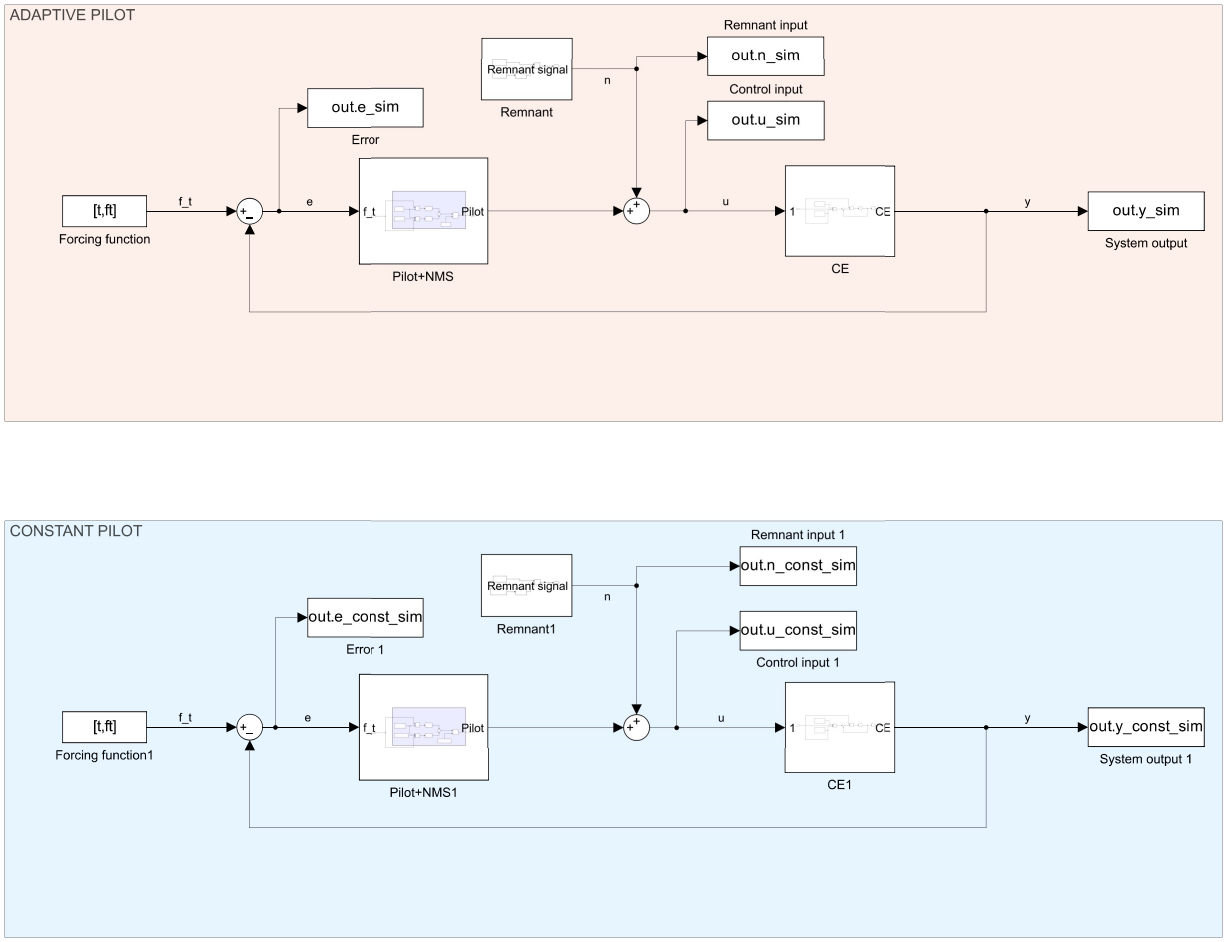

Figure 3.2: Tracking task simulink model

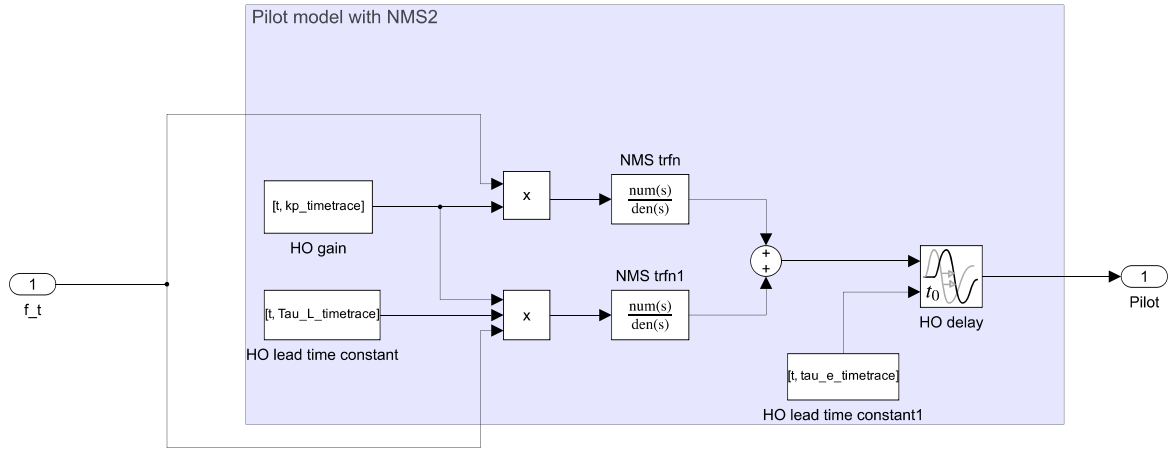

Figure 3.3: Pilot simulink model

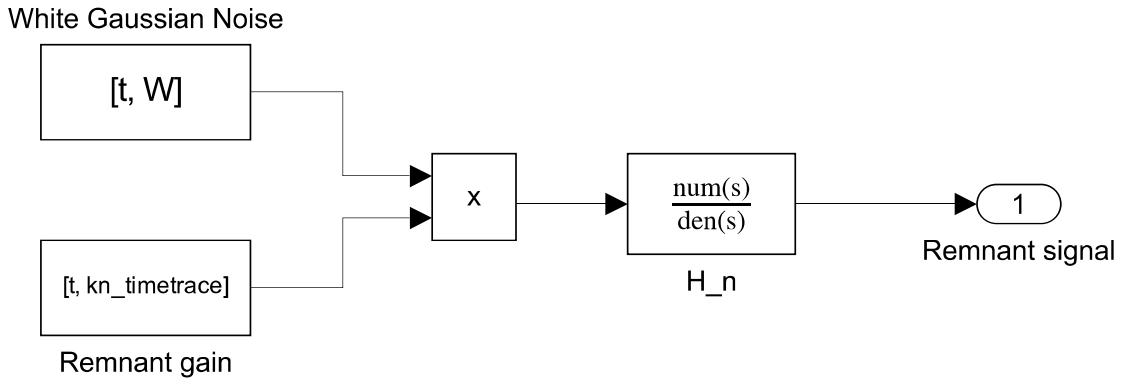

Figure 3.4: Remnant simulink model

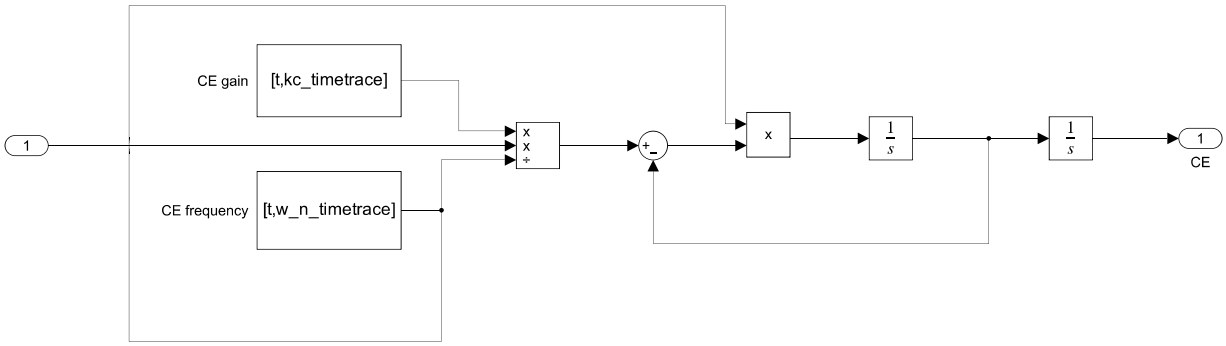

Figure 3.5: CE simulink model

3.0.2. Simulation Results

The culmination of the designed setup is a simulation environment capable of giving high-fidelity frequency-domain and time-domain data that can be used to assess the pilot's control behaviour. The stability of a system cannot be inferred directly from time-domain signals of the tracking task but can be studied in-depth in the frequency domain using open-loop frequency domain techniques. The structure of this research can be explained in a succinct form that frequency domain techniques will be used to identify regions of instability as the pilot adapts to changing CE dynamics and then these regions will be used to obtain time-windows to assess various signals and their characteristic trends. Here, a constant non-adaptive pilot is also taken to compare results and better understand the adaptive behaviour of the pilot.

Firstly, several details need to be known to understand and interpret the results that are presented below. These details are:

- The time duration of all simulations is $200seconds$; Measurement time T_m, which is not a relevant factor for simulations but required for future experiments can be taken to be a multiple of $30s$.
- The time-step $dt = 0.01seconds$ for time-domain simulations and $0.1seconds$ for frequency-domain simulations.
- The adaptive pilot is considered both, optimal and delayed, i.e., $M_{CE} = M_{pilot}$ and $M_{CE} < M_{pilot}$, respectively. The former represents a simplified and hypothetical case while in real-world scenarios, an adaptive pilot has a time lag for when they identify the change in the CE dynamics as seen in [59] and taken care of by the latter case.

- The moment of maximum rate of change is taken to be the mean of the time duration, i.e., $M = 100seconds$ for the optimal pilot and $101seconds$ for the delayed, realistic pilot.
- The rate of change of the sigmoid function for both, the CE and the pilot is then taken to be $G = 100sec^{-1}$ which is a step-change and represents a sudden change in the CE dynamics, for example, structural damage on aircraft or sudden mode change/SAS failure.

Keeping these in mind, the results of the simulations are as presented below after the compensatory tracking task and a time-trace of the forcing function, which are shown for ease of reference.

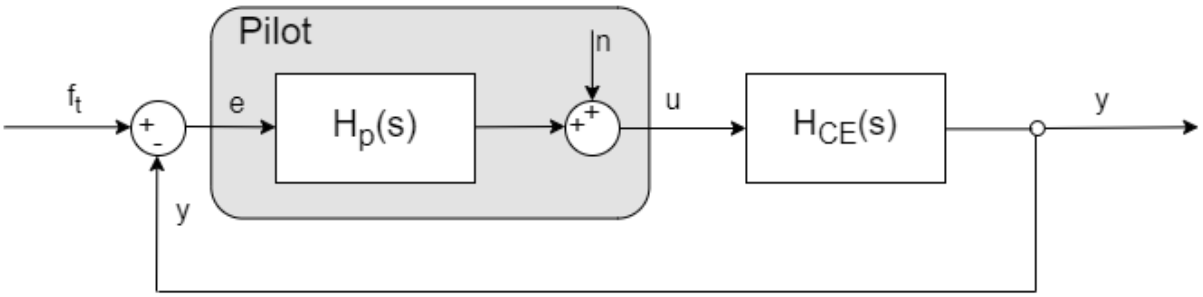

Figure 3.6: Compensatory tracking task for reference

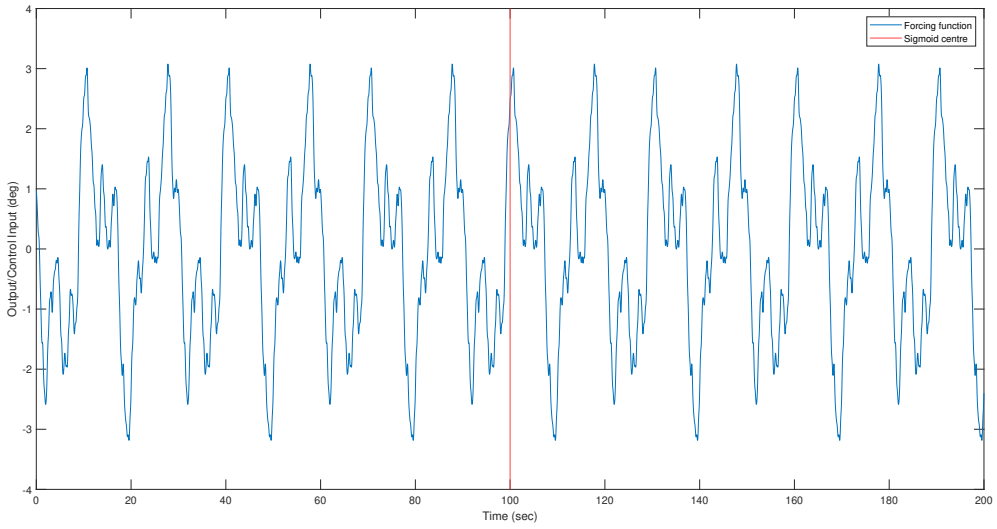

Figure 3.7: Forcing function in time-domain

In the frequency domain, a direct method exists to study the behaviour of an open-loop system, bode plots, i.e., the magnitude and phase plots. The magnitude plot shows the amplitude of the system's response at different frequencies and the the phase plots show the phase shift introduced by the system at different frequencies. Now, a gain crossover frequency ω_{cg} is defined as the frequency at which a system crosses the $0dB$ line in the magnitude plot; at this frequency ω_{cg}, if the phase of the system $\phi_{(\omega=\omega_c g)}$ is checked then a phase margin ϕ_m can be defined as $\phi_m = 180^\circ - \phi_{(\omega=\omega_c g)}$. This phase margin is the amount by which the phase of the open-loop transfer function can be increased (in degrees) before the system becomes unstable; a control system is considered stable if its phase margin is positive and a larger phase margin indicates greater stability. Hence, using this concept, if the phase margin ϕ_m is calculated at each time-step of the duration of the simulation of the time-varying OL dynamics ($CE \times HC$), then the stability of the system can be checked for as a function of time. As a result, if the ϕ_m becomes ≤ 0, then the system can be called unstable.

In the simulations carried out, the phase margins were obtained for the open-loop dynamics of both, the constant pilot and the optimal adaptive and delayed pilot as shown below. It is noted that two figures have been shown for each case with the second showing a magnified view of the regions of instability($\phi_m \leq 0$) for the delayed pilot. The optimal adaptive pilot results are a purely theoretical case, which shows that there are analytical cases where the open loop system is always stable.

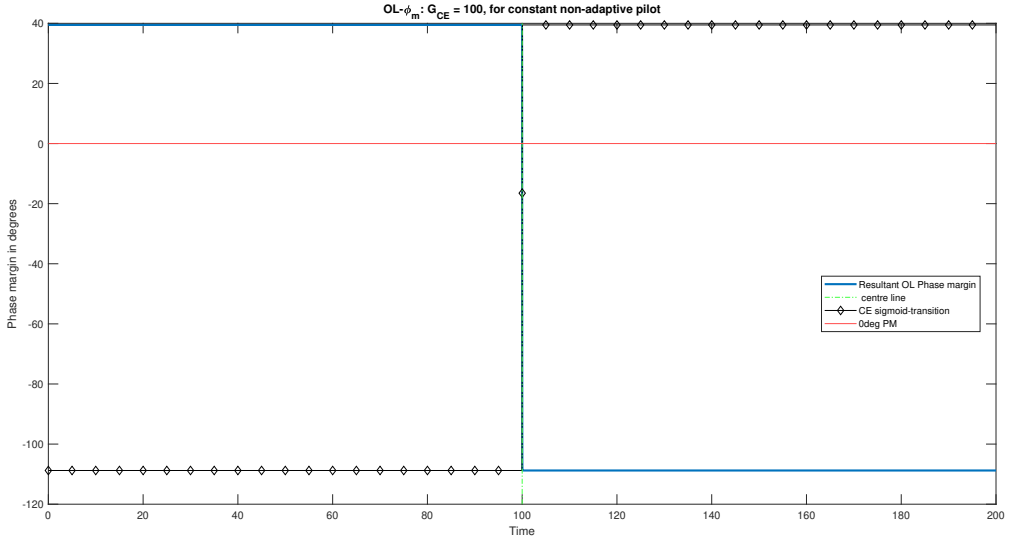

Figure 3.8: ϕ_m of the constant pilot+CE OL dynamics

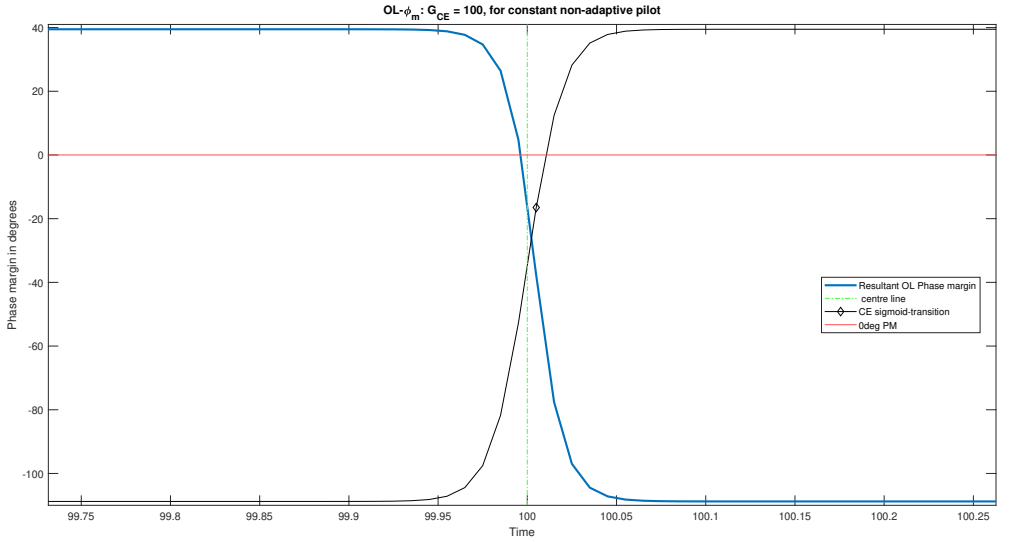

Figure 3.9: Magnified ϕ_m of the constant pilot+CE OL dynamics

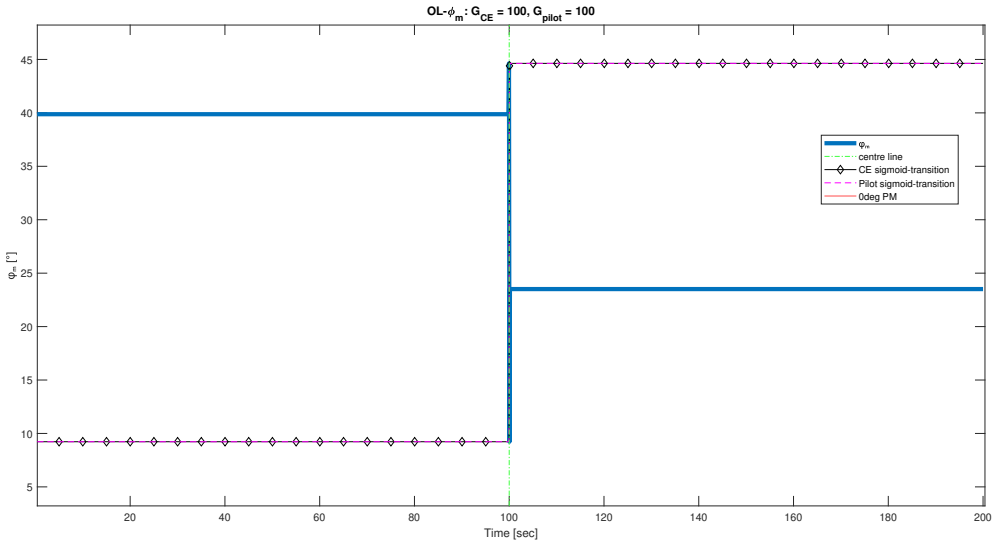

Figure 3.10: ϕ_m of the optimal adaptive pilot+CE OL dynamics

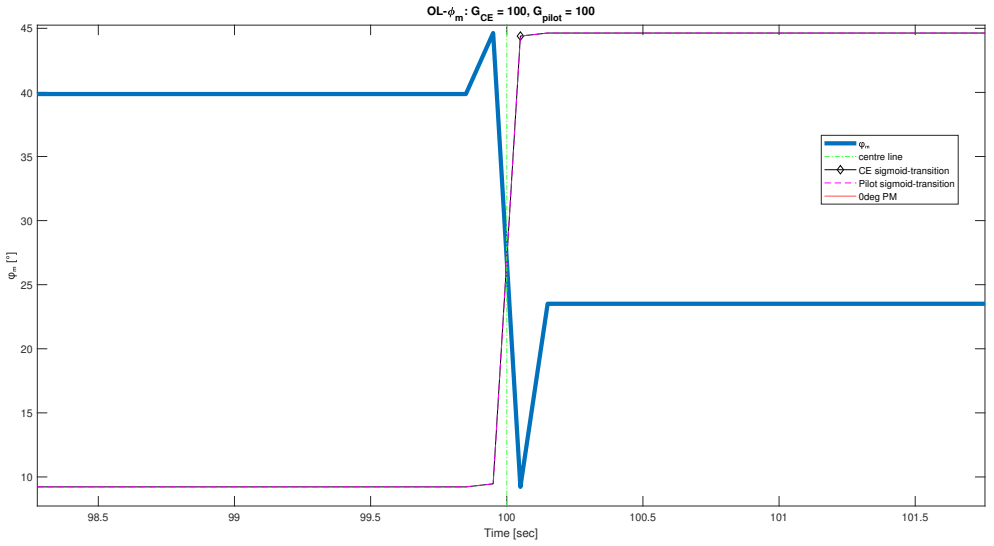

Figure 3.11: Magnified ϕ_m of the optimal adaptive pilot+CE OL dynamics

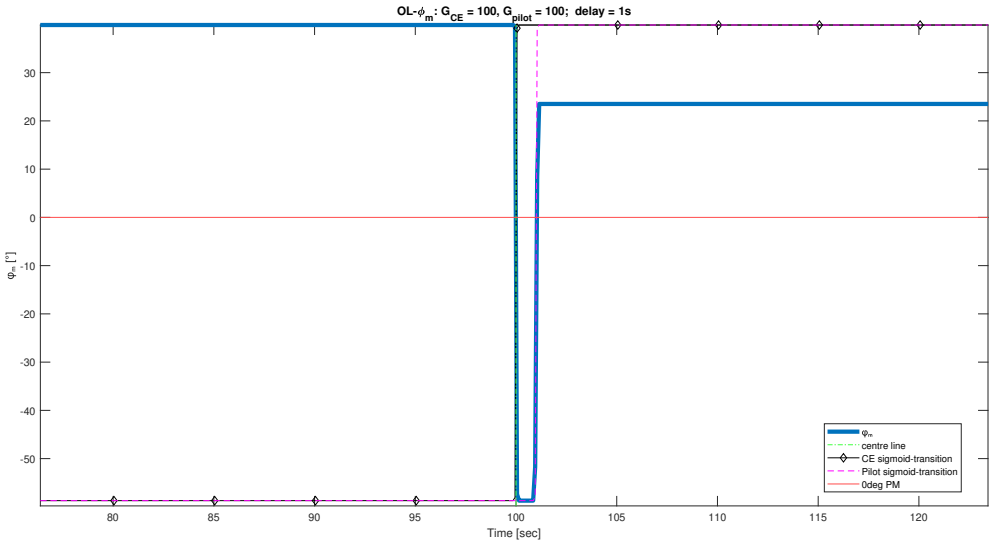

Figure 3.12: Magnified ϕ_m of the delayed adaptive pilot+CE OL dynamics

It can be seen in Figure 3.9, that with the pilot not adapting to the changing CE dynamics, as the weight of the DI tends to become more than SI, the phase margin reduces and consequently the system becomes unstable never to recover as the pilot model that caters to SI dynamics cannot handle DI dynamics. Contrastingly, as the pilot is optimal in Figure 3.11 the phase margin never becomes ≤ 0 and the system remains stable throughout the time duration. Lastly, as seen in Figure 3.12 even though the pilot is adaptive and changes their behaviour with the CE dynamics, the stability of the OL is compromised around M as regions of instability can be seen owing to the delay of the optimal pilot in detecting and hence, adapting to the changing CE dynamics. These regions, though they last only for milliseconds, show the inherent instability of the OL after which the pilot recovers the OL stability.

Having identified regions of instability, time-domain data of the pilot's control output y, control input u and error signals e, have been captured by the Simulink models shown above. The following figures show these time traces for both, constant, and delayed adaptive pilots. The case of optimal adaptive pilot is not considered in time as it is completely theoretical.

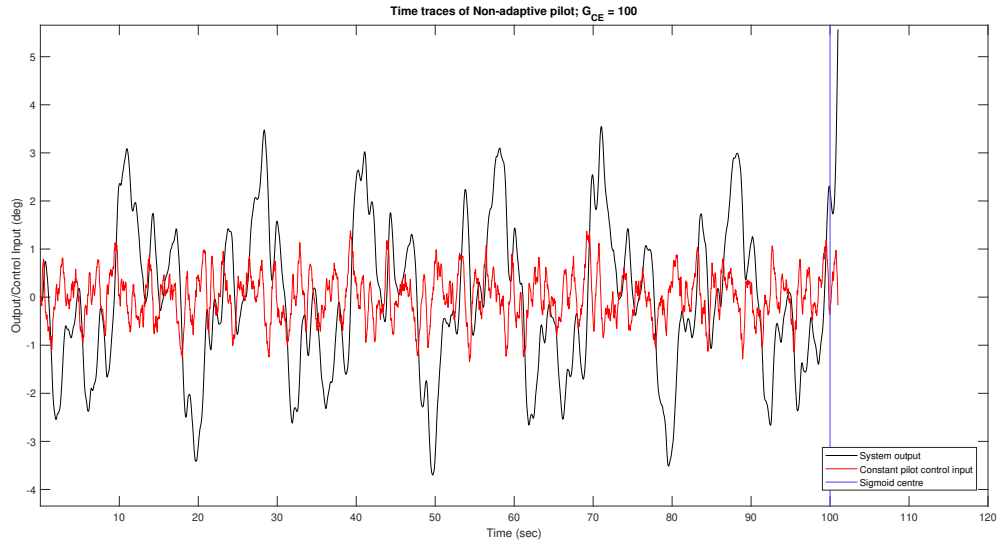

Figure 3.13: Control output and input for the case of constant pilot

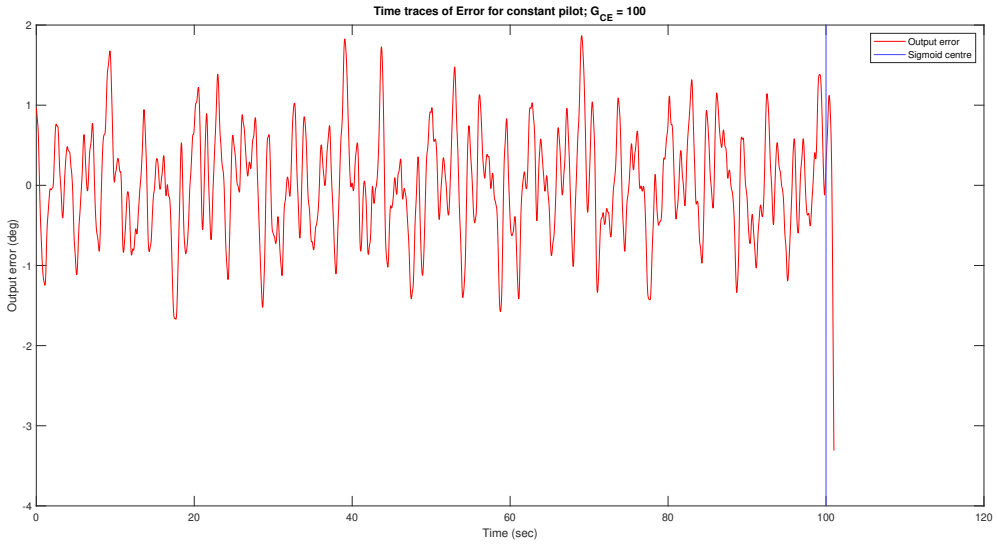

Figure 3.14: Error signals for the case of constant pilot

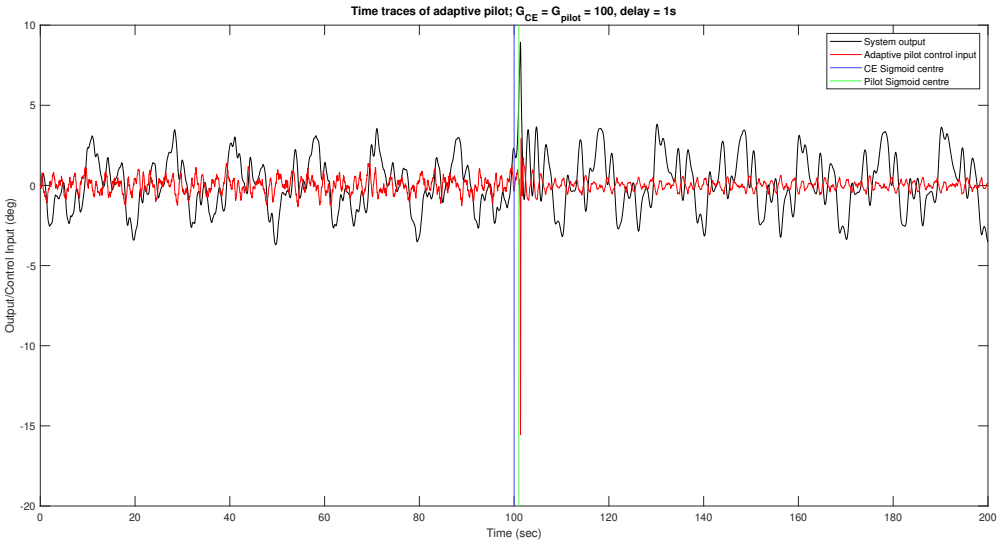

Figure 3.15: Control output and input for the case of adaptive pilot

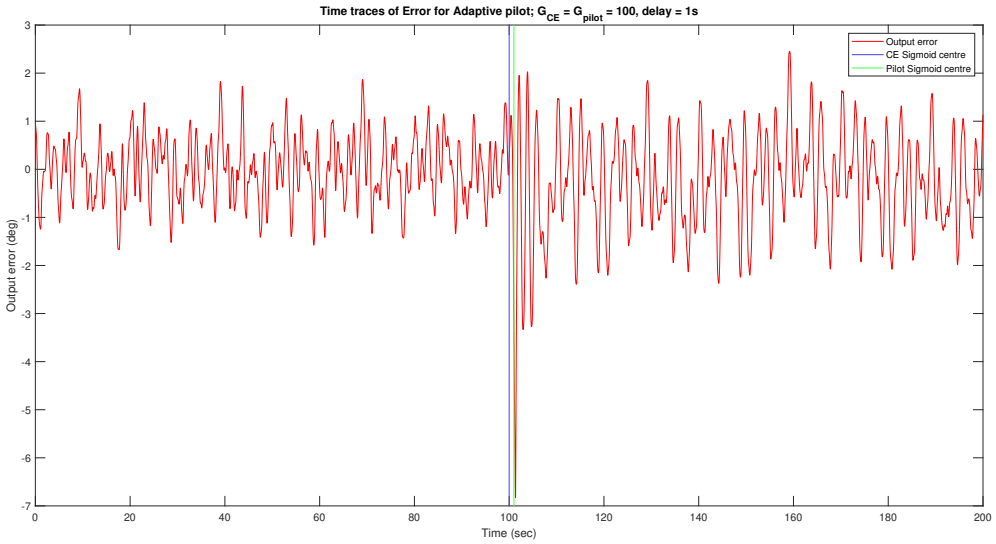

Figure 3.16: Error signals for the case of adaptive pilot

In Figure 3.13 and Figure 3.14, these time-domain signals have been shown till just before the signals diverge and go to unreal-magnitudes. The reason behind showing these signals is to show how in the time-domain the constant pilot's control input as well as the system output look for inherently unstable systems. For the case of the delayed adaptive pilot, Figure 3.15 and Figure 3.16 give valuable insights. At the point where the DI becomes more prominent, i.e., just after M_{pilot}, the control input of the pilot can be seen peak given their delayed detection and followed by a drastic decrease (red signals) compared to pre-transition conditions to maintain the same system control output. This shows how the pilot adapts to DI-like dynamics by decreasing his gain as seen by the control input signals. Also, the error signals become more prominent post M showing the comparative difficulty of controlling DI over SI.

These frequency and time-domain data will be scrutinized further in *research phase 1*, where the time-duration of instability will be calculated from phase margin ϕ_m plots and corresponding time-domain signals will then be extracted. A statistical analysis will be run on these time-domain signals to identify characteristic properties. These tests will be exhaustively explored and the regions will also be varied to analyse, for example, the start of instability regions or the trends that occur just before and similarly for the ends of these instability regions.

The successful execution of this analysis has the potential to enhance pilot training through the online application of the derived methodology. Furthermore, it aids in the identification of controlled element (CE) dynamics that should be avoided when engaging or disengaging Stability Augmentation Systems (SAS). These simulations will also be extended to encompass human-in-the-loop experiments, facilitating the implementation and scrutiny of real-world scenarios.

4

Research Methodology

This chapter deals with the research methodology to be used throughout the duration of this project and elaborates on the relevant progress required to answer the research question proposed in Chapter 1. The structure of this research is such that post the literature study and preliminary set of simulations, the main research is divided into two phases, namely, *research phase 1* and *research phase 2*.

4.1. Research Phase 1

Given the preliminary simulations showing the phase margins as a function of time and the corresponding time-domain signals, namely, control input u, system output y and error e, this phase is planned to deal with a detailed simulation study on the basis of the former results.

The goal of this research phase is to obtain answers to sub-questions 1,2 and 3 mentioned in Chapter 1. In order to do so, the following steps will be followed:

- Use Matlab and Simulink to make a simulator that gives phase margins of resultant open-loop dynamics of the time-varying CE dynamics and the adaptive human controller. Using this simulator, the time stamps of reduced stability/ complete instability will be obtained for the corresponding CE-HO combinations. These simulations will primarily focus on a delayed pilot to increase the fidelity of the simulation along with two G values, namely G_1 and G_2. Where, G_1 will represent a sudden change of CE dynamics using a higher value, for example, a sudden instability caused by an SAS failure; while G_2 will be shown for slower CE changes using lower values, for example, a change in the aircraft's altitude.
- The use of two different G values from the first step of simulations will help to answer sub-question 3 eventually.
- The obtained CE-HO parameters from the simulator will be used to run the Simulink model shown in Chapter 3 which acts as a manual tracking task simulator giving the time-domain signals u, e and y as the output. Then after, the time stamps from the previous simulator will be used to extract these signals for the specific duration. By doing so, the time-domain trends will be obtained for the regions of reduced stability/ complete instability.
- The resultant time periods of the signals will be statistically analysed based on the mean, variance and standard deviation. The first derivatives of these signals will also undergo the same statistical tests. As a result, relevant signals and their rates will be compared with the pre-transition duration of the simulation, which includes a steady-state CE-HO combination. The aim here is to obtain definite trends using one or multiple signals.
- Monte-Carlo simulations will be run for the process detailed above to successfully generalize the results of the time signals, for both, slow (G_2) and fast (G_1) CE changes.

It is noted that the CE changes will only include single-integrator-like (SI) to double-integrator-like (DI) given that a transition from easy-to-difficult dynamics is prone to result in instability which is the focus of this study. Moreover, the simulation used to obtain phase margin vs time ($\phi_m - t$) plots uses Equation 2.2 as the pilot model and does not include the remnant transfer function as it is independent of phase margins, which are completely a function of the system's dynamics, i.e., $H_p(s)$ and $H_{CE}(s)$. Consequently, *research phase 1* will help answer sub-questions 1,2 and 3 that deal with signals, their characteristics and the effect of rate of change on the detection of change in CE dynamics.

4.2. Research Phase 2

The results and the answers from *research phase 1* will be used to then form hypotheses which will be proved/disproved in *research phase 2*. This research phase focuses on the experimental implementation of the simulations to generate validations of the model that is created to understand the detection mechanism of the adaptive pilot.

In this phase (*research phase 2*), the Human-Machine Interaction Laboratory (HMI Lab) simulator of the Faculty of Aerospace Engineering at Delft University of Technology will be used to conduct manual tracking task experiments, with compensatory and pursuit displays. Here, even though the simulations are mathematically restricted to replicate compensatory tracking tasks, the same results will also be used for pursuit tracking tasks. The details of the second phase are as mentioned below:

- An experimental setup will be designed to conduct within-participants experiments using pursuit and compensatory displays with each display having two G values, G_1 and G_2 for a transition $SI \rightarrow DI$ CE transition.
- A Maximum Likelihood Estimation (MLE) algorithm will be used that utilizes the magnitude and phase data obtained from the experimental setup for the pilot's parameter estimation.
- Subsequently, the simulators used in *research phase 1* will be used along with the relevant signal's characteristics to verify the answers obtained from the simulations.
- Ultimately, all four sub-questions will be answered resulting in an answer to the research question and fulfilling the research objective.

At its culmination, this study will aim to equip the research community with a method to better understand how the adaptive pilot detects the changes in controlled element dynamics in manual tracking tasks.

References

[1] Frank M Drop. *Control-Theoretic Models of Feedforward in Manual Control*. Vol. 46. Logos Verlag Berlin GmbH, 2016. url: https://api.semanticscholar.org/CorpusID:114491896.

[2] Max Mulder et al. “Manual control cybernetics: State-of-the-art and current trends”. In: *IEEE Transactions on Human-Machine Systems* 48.5 (2017), pp. 468–485. doi: 10.1109/THMS.2017.2761342.

[3] Max Mulder et al. “Fundamental issues in manual control cybernetics”. In: *IFAC-PapersOnLine* 49.19 (2016), pp. 1–6. doi: 10.1016/j.ifacol.2016.10.429.

[4] Duane T McRuer. “Human pilot dynamics in compensatory systems-theory, models, and experiments with controlled element and forcing function variations”. In: *AFFDL-TR-65-15* (1965).

[5] *Loss of Control In-flight (LOC-I)*. https://www.iata.org/en/programs/safety/operational-safety/loss-of-control-inflight/. Accessed: 2023-10-11.

[6] Peter Zaal et al. “Estimation of time-varying pilot model parameters”. In: *AIAA Modeling and Simulation Technologies Conference*. 2011, p. 6474. url: https://doi.org/10.2514/6.2011-6474.

[7] Duane T McRuer et al. “A review of quasi-linear pilot models”. In: *IEEE transactions on human factors in electronics* 3 (1967), pp. 231–249. doi: 10.1109/THFE.1967.234304.

[8] Herman J Damveld et al. “Design of forcing functions for the identification of human control behavior”. In: *Journal of Guidance, Control, and Dynamics* 33.4 (2010), pp. 1064–1081. url: https://doi.org/10.2514/1.47730.

[9] MM Van Paassen et al. “Identification of human control behavior in multiple-loop tracking tasks”. In: *International encyclopedia of ergonomics and human factors* (2006), pp. 400–407. url: https://doi.org/10.1016/S1474-6670(17)40135-2.

[10] DM Pool et al. “Effects of peripheral visual and physical motion cues in roll-axis tracking tasks”. In: *Journal of guidance, control, and dynamics* 31.6 (2008), pp. 1608–1622. url: https://doi.org/10.2514/1.36334.

[11] Herman J Damveld. “A cybernetic approach to assess the longitudinal handling qualities of aeroelastic aircraft”. In: (2009).

[12] GC Beerens et al. “Investigation into crossover regression in compensatory manual tracking tasks”. In: *Journal of guidance, control, and dynamics* 32.5 (2009), pp. 1429–1445. url: https://doi.org/10.2514/1.43528.

[13] Henry R Jex et al. “Corroborative data on normalization of human operator remnant”. In: *IEEE Transactions on Man-Machine Systems* 10.4 (1969), pp. 137–140. url: https://doi.org/10.1109/TMMS.1969.299912.

[14] William H Levison et al. “A model for human controller remnant”. In: *IEEE Transactions on man-machine systems* 10.4 (1969), pp. 101–108. url: https://doi.org/10.1109/TMMS.1969.299906.

[15] K Van der El et al. “Analysis of human remnant in pursuit and preview tracking tasks”. In: *IFAC-PapersOnLine* 52.19 (2019), pp. 145–150. doi: 10.1016/j.ifacol.2019.12.165..

[16] Andries van Grootheest et al. “Identification of Time-Varying Manual Control Adaptations with Recursive ARX Models”. In: *2018 AIAA Modeling and Simulation Technologies Conference*. 2018, p. 0118. url: https://doi.org/10.2514/6.2018-0118.

[17] Arnold Tustin. “The nature of the operator’s response in manual control, and its implications for controller design”. In: *Journal of the Institution of Electrical Engineers-Part IIA: Automatic Regulators*

and Servo Mechanisms 94.2 (1947), pp. 190–206. url: https://doi.org/10.1049/ji-2a.1947.0025.

[18] Jerome I Elkind. “Characteristics of simple manual control systems”. PhD thesis. Massachusetts Institute of Technology, 1956. url: http://hdl.handle.net/1721.1/26873.

[19] Robert L Stapleford et al. “Pilot describing function measurements in a multiloop task”. In: *IEEE Transactions on Human Factors in Electronics* 2 (1967), pp. 113–125. url: https://doi.org/10.1109/THFE.1967.233628.

[20] Max Mulder et al. “Manual control with pursuit displays: New insights, new models, new issues”. In: *IFAC-PapersOnLine* 52.19 (2019), pp. 139–144. url: https://doi.org/10.1016/j.ifacol.2019.12.125.

[21] Laurence R Young et al. “Adaptive dynamic response characteristics of the human operator in simple manual control”. In: *IEEE Transactions on Human Factors in Electronics* 1 (1964), pp. 6–13. url: https://doi.org/10.1109/THFE.1964.231648.

[22] Melvin Sadoff. *A Study of a Pilots Ability to Control During Simulated Stability Augmentation System Failures*. National Aeronautics and Space Administration, 1962. doi: 19630000307.

[23] JD McDonnell. “A preliminary study of human operator behavior following a step change in the controlled element”. In: *IEEE Transactions on Human Factors in Electronics* 3 (1966), pp. 125–128. url: https://doi.org/10.1109/THFE.1966.232651.

[24] Richard J Wasicko et al. *Human pilot dynamic response in single-loop systems with compensatory and pursuit displays*. Vol. 66. Air Force Flight Dynamics Laboratory, Research and Technology Division, Air …, 1966. url: https://doi.org/10.21236/ad0646652.

[25] Anil V Phatak et al. “Model of the adaptive behavior of the human operator in response to a sudden change in the control situation”. In: *IEEE Transactions on Man-Machine Systems* 10.3 (1969), pp. 72–80. url: https://doi.org/10.1109/TMMS.1969.299886.

[26] Jacomijn van Ham. “Predicting Adaptive Human Control Behavior to Changing Controlled Element Dynamics Based on Statistical Variations in Error and Error Rate”. In: (2021). url: https://doi.org/10.1016/j.ifacol.2022.10.250.

[27] David H Weir et al. “Pilot’s Response to Stability Augmentation System Failures and Implications for Design”. In: *Proceedings of the Fourth Annual NASA-University Conference on Manual Control*. 1969, pp. 341–360. url: https://doi.org/10.2514/3.44096.

[28] MM René van Paassen et al. “Identification of human operator control behaviour in multiple-loop tracking tasks”. In: *IFAC Proceedings Volumes* 31.26 (1998), pp. 455–460. url: http://dx.doi.org/10.1016/S1474-6670(17)40135-2.

[29] Ronald A Hess. “Modeling pilot control behavior with sudden changes in vehicle dynamics”. In: *Journal of Aircraft* 46.5 (2009), pp. 1584–1592. url: https://doi.org/10.2514/1.41215.

[30] Ronald Hess. “A preliminary study of human pilot dynamics in the control of time-varying systems”. In: *AIAA modeling and simulation technologies conference*. 2011, p. 6554. url: https://doi.org/10.2514/6.2011-6554.

[31] Peter Zaal et al. “Identification of Time-Varying Pilot Control Behavior in Multi-Axis Control Tasks”. In: *AIAA Modeling and Simulation Technologies Conference*. 2012, p. 4793. url: http://dx.doi.org/10.2514/6.2012-4793.

[32] David Klyde et al. “Wavelet-based time-varying human operator models”. In: *AIAA Atmospheric Flight Mechanics Conference and Exhibit*. 2001, p. 4009. url: https://doi.org/10.2514/6.2001-4009.

[33] Peter Thompson et al. “Development of wavelet-based techniques for detecting loss of control”. In: *AIAA Atmospheric Flight Mechanics Conference and Exhibit*. 2004, p. 5064. url: https://doi.org/10.2514/6.2004-5064.

[34] DM Pool et al. “Identification of nonlinear motion perception dynamics using time-domain pilot modeling”. In: *Journal of guidance, control, and dynamics* 35.3 (2012), pp. 749–763. url: https://doi.org/10.2514/1.56236.

[35] Wouter Plaetinck et al. “Online identification of pilot adaptation to sudden degradations in vehicle stability”. In: *IFAC-PapersOnLine* 51.34 (2019), pp. 347–352. url: https://doi.org/10.1016/j.ifacol.2019.01.020.

[36] Ronald A Hess. “A model for pilot control behavior in analyzing potential loss-of-control events”. In: *Proceedings of the Institution of Mechanical Engineers, Part G: Journal of Aerospace Engineering* 228.10 (2014), pp. 1845–1856. url: https://doi.org/10.2514/6.2011-6474.

[37] Ronald A Hess. “Modeling human pilot adaptation to flight control anomalies and changing task demands”. In: *Journal of Guidance, Control, and Dynamics* 39.3 (2016), pp. 655–666. url: https://doi.org/10.2514/1.G001303.

[38] ShuTing Xu et al. “Pilot time-varying control behavior modeling in refractory period with aircraft failures”. In: *Science China Technological Sciences* (2023), pp. 1–13. url: https://doi.org/10.1007/s11431-022-2099-6.

[39] Ronald A Hess. “Modeling the pilot detection of time-varying aircraft dynamics”. In: *Journal of aircraft* 49.6 (2012), pp. 2100–2104. url: https://doi.org/10.2514/1.C031805.

[40] Nora Jakimovska et al. “Using the Hess Adaptive Pilot Model for Modeling Human Operator’s Control Adaptations in Pursuit Tracking”. In: *AIAA SCITECH 2023 Forum*. 2023, p. 0541. doi: 10.2514/6.2023-0541.

[41] Maxim C Vos et al. “Identification of multimodal control behavior in pursuit tracking tasks”. In: *2014 IEEE International Conference on Systems, Man, and Cybernetics (SMC)*. IEEE. 2014, pp. 63–68. url: https://doi.org/10.1109/SMC.2014.6973885.

[42] Kasper van der El et al. “An empirical human controller model for preview tracking tasks”. In: *IEEE transactions on cybernetics* 46.11 (2015), pp. 2609–2621. url: https://doi.org/10.1109/tcyb.2015.2482984.

[43] Ronald Andrew Hess. “The human operator as an element in a control system with time varying dynamics”. B.S. thesis. University of Cincinnati, 1965.

[44] Peter Zaal et al. “Multimodal pilot behavior in multi-axis tracking tasks with time-varying motion cueing gains”. In: *AIAA Modeling and Simulation Technologies Conference*. 2014, p. 0810. url: https://doi.org/10.2514/6.2014-0810.

[45] PMT Zaal et al. “Multimodal pilot control behavior in combined target-following disturbance-rejection tasks”. In: *Journal of guidance, control, and dynamics* 32.5 (2009), pp. 1418–1428. url: https://doi.org/10.2514/1.44648.

[46] Peter MT Zaal et al. “Use of pitch and heave motion cues in a pitch control task”. In: *Journal of Guidance, Control, and Dynamics* 32.2 (2009), pp. 366–377. url: https://doi.org/10.2514/1.39953.

[47] Daan M Pool et al. “Effects of heave washout settings in aircraft pitch disturbance Rejection”. In: *Journal of guidance, control, and dynamics* 33.1 (2010), pp. 29–41. url: https://doi.org/10.2514/1.46351.

[48] Peter MT Zaal. “Manual control adaptation to changing vehicle dynamics in roll-pitch control tasks”. In: *Journal of guidance, control, and dynamics* 39.5 (2016), pp. 1046–1058. url: https://doi.org/10.2514/1.G001592.

[49] M Jirgl et al. “Measuring and evaluation of dynamic properties of human operator”. In: *Ifac-Papersonline* 49.25 (2016), pp. 266–271. url: https://doi.org/10.1016/j.ifacol.2016.12.045.

[50] Frank M Drop et al. “The predictability of a target signal affects manual feedforward control”. In: *IFAC-PapersOnLine* 49.19 (2016), pp. 177–182. url: https://doi.org/10.1016/j.ifacol.2016.10.482.

[51] RE Magdaleno et al. “Tracking Quasi-Predictable Displays Subjective Predictability Gradations, Pilot Models for Periodic and Narrowband Inputs”. In: *Annual NASA-University Conference on Manual Control*. Vol. 215. Scientific and Technical Information Division, Office of Technology … 1969, p. 391.

[52] Lorenzo Terenzi et al. “Adaptive manual control: A predictive coding approach”. In: *AIAA SCITECH 2022 Forum*, p. 2448. url: https://doi.org/10.2514/6.2022-2448.

[53] Max Mulder et al. “Probabilistic Perspective on Compensatory, Pursuit and Preview Manual Control”. In: *IFAC-PapersOnLine* 55.29 (2022), pp. 154–159. url: https://doi.org/10.1016/j.ifacol.2022.10.248.

[54] Kasper van der El et al. “Effects of Target Trajectory Bandwidth on Manual Control Behavior in Pursuit and Preview Tracking”. In: *IEEE Transactions on Human-Machine Systems* PP (Nov. 2019), pp. 1–11. doi: 10.1109/THMS.2019.2947577.

[55] Duncan C Miller et al. “The adaptive response of the human controller to sudden changes in controlled process dynamics”. In: *IEEE Transactions on Human Factors in Electronics* 3 (1967), pp. 218–223. url: https://doi.org/10.1109/THFE.1967.233971.

[56] R Wade Allen et al. *An experimental investigation of compensatory and pursuit tracking displays with rate and acceleration control dynamics and a disturbance input*. Tech. rep. NASA, 1968.

[57] RJ Niemela et al. “Detection of Change in Plant Dynamics in Man-Machine”. In: *IEEE Transactions on Systems, Man, and Cybernetics* (1975).

[58] Iuliia Zaitceva et al. “Approach to Identifying Areas of Uncontrolled Oscillations in Human-Machine Systems”. In: *2023 International Russian Smart Industry Conference (SmartIndustryCon)*. IEEE. 2023, pp. 196–201. url: https://doi.org/10.1109/SmartIndustryCon57312.2023.10110762.

[59] LR Young. “On adaptive manual control”. In: *Ergonomics* 12.4 (1969), pp. 635–674. url: https://doi.org/10.1109/TMMS.1969.299931.

Part II

Scientific Article

Pilot's Detection of Change in Aircraft Dynamics: An Open-Loop Stability Model For Varying Display Types and Transition Rates

Devashish Patel *
Control and Simulation Section, Faculty of Aerospace Engineering,
Delft University of Technology, Delft, The Netherlands

The human operators' manual control behaviour under time-invariant conditions has been successfully modelled. However, significant gaps remain in understanding and modelling adaptive manual control behaviour under time-varying conditions. One such less-understood aspect is the pilot's ability to detect changes in time-varying controlled element dynamics. This study aims to develop a mathematical model that investigates open-loop stability as a criterion in compensatory and pursuit tracking tasks to model the pilot's detection of change in controlled element dynamics across different transition rates, particularly for transitions from stable to less-stable vehicle dynamics. The model operates under the assumption that trained human operators track statistical properties of tracking task signals within periods of compromised open-loop stability to trigger their detection of change in dynamics. The model identifies regions of reduced stability and simulates the tracking task signals through time-varying computer simulations. Subsequently, human-in-the-loop experiments are conducted to validate the model. The validated model demonstrates a combined accuracy of 88.54% **for the compensatory task and** 80.62% **for the pursuit task. Notably, in the experiments, the error signal consistently outperforms the error rate signal across all transition rates, diverging from the results of the computer simulations. Overall, the proposed model's ability to successfully predict pilot detection across a spectrum of transition rates marks an advancement towards developing more human-like automation.**

Nomenclature

$\dot{e}(t)$	=	Error rate signal $(^\circ/s)$
$\dot{u}(t)$	=	Control input rate signal $(^\circ/s)$
$\dot{y}(t)$	=	Control output rate signal $(^\circ/s)$
ω_b	=	CE break frequency (rad/s)
ω_c	=	Crossover frequency (rad/s)
ω_i	=	Bandwidth of forcing function (rad/s)
ω_m	=	Fundamental frequency (rad/s)
$\omega_t[i]$	=	Frequency of the i^{th} sinusoid (rad/s)
ω_{nm}	=	Natural frequency of the neuromuscular system (rad/s)
ϕ	=	Phase (rad)
ϕ_m	=	Phase margin $(^\circ)$
$\phi_t[i]$	=	Phase shift of the i^{th} sinusoid (rad)
ρ	=	Pearson correlation coefficient (-)
σ	=	Standard deviation (-)
σ_u^2	=	Total power in control input (rad^2)
$\sigma_{uf_t}^2$	=	Variance/Power of forcing function in control input (rad^2)
σ_{un}^2	=	Variance/Power of noise in control input (rad^2)
τ_e	=	Effective time delay (s)
τ_n	=	Remnant time constant (s)
ζ_{nm}	=	Damping ratio of the neuromuscular system (-)
$A_t[i]$	=	Amplitude of the i^{th} sinusoid (rad)
$e(t)$	=	Error signal $(^\circ)$

*MSc Student, Control and Simulation Section, Faculty of Aerospace Engineering, Delft University of Technology

$f_t(t)$ = Forcing function (°)
FN = False negative (-)
FP = False positive (-)
G = Rate of transition (s^{-1})
$H_n(s,t)$ = Remnant transfer function (-)
$H_p(s,t)$ = Pilot transfer function (-)
$H_{CE}(s,t)$ = Controlled Element (CE) transfer function (-)
k = Multiple of base frequency (-)
K_c = CE gain (-)
K_n = Remnant gain (-)
K_p = Pilot gain (-)
M = Moment of maximum rate of transition (s)
$n(t)$ = Noise signal (°)
P_1 = Initial parameter value (-)
P_2 = Final parameter value (-)
P_n = Specific power ratio (-)
$RMSE$ = Root mean square error (°)
t = Time (s)
T_L = Lead time (s)
T_m = Measurement time (s)
$T_{\phi_m \leq 15^\circ}$ = Time of the first instance of phase margin $\leq$ 15°
$T_{M_{pilot}}$ = Time value of centre (M) of pilot-sigmoid (s)
T_{tr} = Time taken to transition from 5% to 95% of final value (s)
TN = True negative (-)
TP = True positive (-)
$u(t)$ = Control input signal (°)
W = Intensity of white noise (-)
$w(t)$ = Gaussian white noise (-)
$y(t)$ = Control output signal (°)

I. Introduction

Loss of Control-Inflight (LOC-I) has long been one of the leading causes of fatal aviation accidents [1], which can arise in situations like Stability Augmentation System (SAS) failure. In such conditions, the pilot has to take control of the aircraft immediately i.e., shift from supervisory control to manual control. Analysis of such safety-critical manual control tasks can help develop insights into adaptive human behaviour and increase safety. In the present context, as a result of McRuer's crossover model [2], we have a thorough understanding of pilot-vehicle systems in steady-state (time-invariant) conditions but lack valuable insight into conditions of time-varying controlled element dynamics [3], which has made it vital to understand adaptive human control behaviour better. Moreover, with the development of new flight control systems, the current models of human control behaviour have fallen behind [4]. Hence, this study addresses the pressing need for mathematical models that adequately describe adaptive human control behaviour. The importance of this research lies in its potential applications; gaining insight into the limitations of human operators can significantly contribute to the advancement of man-machine systems. Furthermore, at a time when there is a growing emphasis on reducing human intervention, understanding human adaptability can enhance the design of human-like automated control systems that can address the phenomena highlighted in the automation paradox.

In the pursuit of modelling adaptive human behaviour, Young et al. [5] identified adaptive behaviour to occur in three stages, namely, *detection*, where the human operator detects that a change in Controlled Element (CE) dynamics has occurred; *identification*, where the human operator adapts to the new CE dynamics and; *adjustment*, which involves reducing the error following the change in strategy. It can be argued that the latter two stages occur simultaneously while the first phase is distinct. Amongst all the three phases, the detection phase is of prime interest to this study. The ability to mathematically model the pilot's detection phase is essential, as such a model can be utilised for pilot training and the development of more efficient automatic control systems. For instance, this could involve enhancing the detection process artificially or designing systems that produce changes in dynamics that are easier for pilots to detect. The significance of detection is highlighted in Sadoff's study [6], which emphasises the necessity for the aircraft

to be engineered in a manner that ensures acceptable aircraft dynamics in the event of inoperative or failed Stability Augmentation Systems (SAS). This directly illustrates the practical application of having a model for the Human Operator's (HO) detection of changes in CE dynamics.

Numerous studies have explored various approaches to modelling adaptive human behaviour [5, 7–19]. Among these, the research conducted by Hess [18][19] stands out. Hess's study involved the use of time-varying CE dynamics, incorporating both slow and fast changes, to investigate human adaptation in pursuit and compensatory tracking tasks, including single and two-axis tasks. In his findings, the detection phase was identified based on the system's error rate crossing a threshold value derived from a multiple of the steady-state (pre-transition) standard deviation. Subsequently, several models, particularly for compensatory tracking tasks where CE dynamics transition from more stable to less stable states, have been proposed. These models utilise a similar threshold, either on the tracking error or error rate [10] [20][21]. The underlying premise of these findings is that well-trained human operators keep track of the statistical properties of signals and can detect changes by identifying abnormalities in them. Notably, the findings regarding the graceful degradation of Flight Control Systems (FCS), leading to improved tracking performance (reduced RMSE) [22], suggest that the rate of change of CE dynamics also influences adaptive control behaviour.

To date, the aforementioned research has primarily concentrated on identifying the signals employed by human operators to detect changes in controlled element (CE) dynamics. However, a crucial aspect that remains inadequately addressed is understanding the rationale behind the utilization of these signals during the time interval preceding detection, with a specific focus on how varying rates of change in CE dynamics influence their usage. With current literature [3, 23–26] limited in the rates of transition examined, with the majority focused on $100s^{-1}$ (very fast) and/or $0.5s^{-1}$ (very slow), the knowledge gap suggests an incomplete understanding of the detection phase in human adaptive control behaviour. In essence, a fast transition makes the change obvious while a slow transition makes it difficult for the adaptive pilot to detect the change. Moreover, it also raises a question regarding the impact of display types on the detection process for varying transition rates. This question highlights a lack of understanding of the role of visual feedback and interface design in adaptive manual control behaviour.

In practical applications, different types of displays are used, with compensatory and pursuit displays being the primary choices in aviation. While in the former, the only information provided to the HO is the error e between the system output y and target signal f_t, the latter provides explicit visibility of the target signal and the system output, which also leads to the visibility of the error ($e = f_t - y$). The display types and their associated control diagrams are shown in Figure 1 and Figure 2. Here, the compensatory display, which only includes the error signal, allows for the adoption of a single strategy ($H_p(s,t)$) for the tracking task while the pursuit display offers multiple strategies that the pilot can utilise, namely, $H_{pe}(s,t)$, $H_{pt}(s,t)$, and $H_{px}(s,t)$. As the precision model and the crossover model are limited to compensatory displays, the simulations conducted in this study pertain to compensatory displays. However, the experiments also include the pursuit display to evaluate the model's applicability and performance comprehensively.

Furthermore, the universally accepted precision model by McRuer and Jex [7], defines the pilot's behaviour towards Time-Invariant (TI) CE dynamics for compensatory displays. Based on this model, it can be argued that the stability of the Open-Loop (OL) system during the CE transition from stable to less-stable dynamics will decrease or will be completely lost when the pilot does not adapt. Notably, the adapting pilot adapts to the changed CE dynamics but with a delay; there exists a certain delay between the actual moment of change in CE dynamics and the moment of the pilot's detection of change. Consequently, the pilot's *delayed* adjustment of control behaviour, may result in transitional instability/reduced stability of the open-loop system. The study aims to use this phenomenon to model the pilot's detection of changes in CE dynamics. To achieve the objective, time-varying compensatory tracking task simulations are conducted to obtain two outputs, namely, the crossover model parameters and time domain signals. While the former helps determine the time duration (region) of compromised OL stability the latter provides the time signals of the tracking task. Both these sets of results are then examined using Monte Carlo simulations followed by experiments that address the effect of different display types. This approach gives an insight into how varying rates of change affect the HO's use of tracking task signals to detect the change in CE dynamics as a function of the provided display.

Notably, in this study, the CE dynamics always transition from stable (Single-Integrator (SI)) dynamics, indicating a responsive vehicle, to unstable (Double-Integrator (DI)) dynamics characterized by sluggishness and reduced stability margins. This characteristic feature aims to make the change in CE dynamics easily noticeable to the pilot and visible in the OL phase margins.

The structure of this paper is as follows: first, a comprehensive explanation of the design, methodology, and outcomes of the computer simulations is provided in section II, followed by the resulting hypotheses. Thenafter, the details of the experiment's design and data analysis methodology are outlined in section III, while section IV presents the results of the experiments. Lastly, section V comments on the findings of the study with section VI consisting of the

conclusions.

II. Methodology

The initial phase of the study deals with MATLAB simulations that are categorised into two parts, based on required outputs:

- **Crossover model calculations** denoted as frequency-domain (f-domain) outputs
- **Time signal calculations** denoted as Time-domain (t-domain) outputs

Here, the f-domain outputs help analyse the system's behaviour in the frequency domain and comprise the required crossover model parameters, namely, the crossover frequency (ω_c) and phase margin (ϕ_m) to quantify the stability of the open-loop (OL) system as a function of time for Time-Varying (TV) CE dynamics. These results are interpreted as the duration of compromised stability margins. The t-domain results are obtained using a SIMULINK model that replicates the control diagram of a compensatory tracking task depicted in Figure 1. This generates six time signals, namely, error $e(t)$, control input $u(t)$, system output $y(t)$, and their derivatives $\dot{e}(t)$, $\dot{u}(t)$, and $\dot{y}(t)$. Thus, the computer simulations help identify how the regions of reduced open loop stability manifest in the t-domain signals, and use this insight to model the human controller's detection of change in CE dynamics.

This section first details the common design setup of the computer simulation required to obtain both outputs in subsection II.A, followed by the output-specific design steps in subsection II.B and subsection II.C.

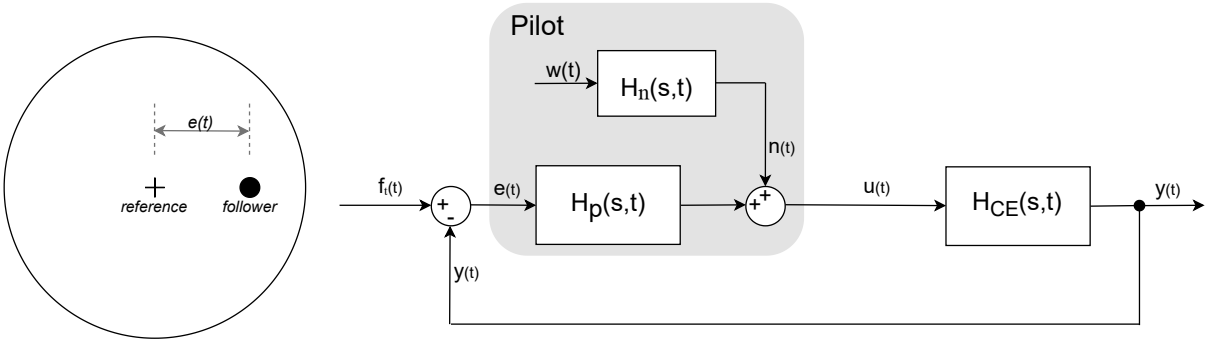

Fig. 1 Compensatory display and the corresponding tracking task control diagram

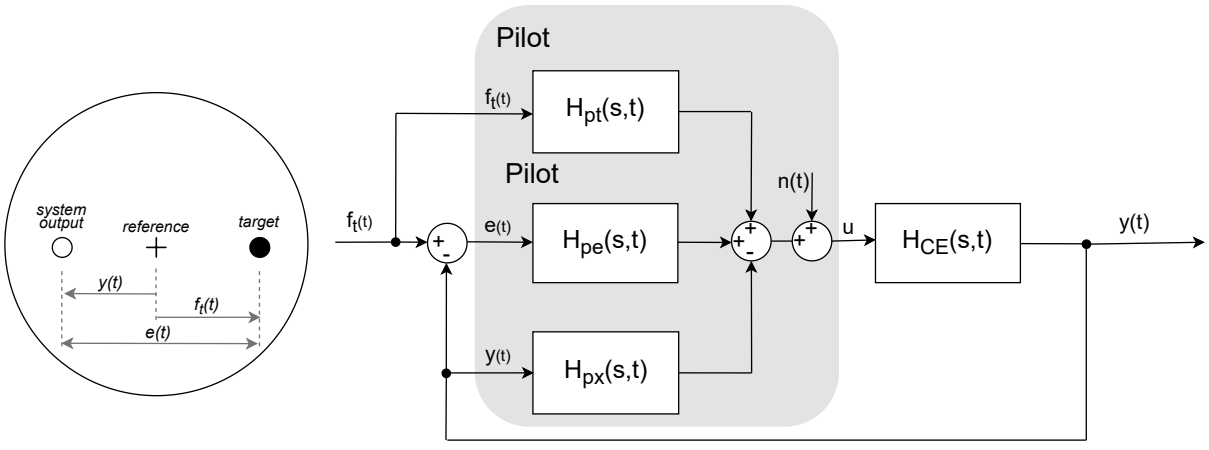

Fig. 2 Pursuit display and the corresponding tracking task control diagram

A. Common Simulation Setup

The common design steps for both sets of output include the design of the Controlled Element (CE) and the pilot model. While for the f-domain output, the CE-pilot system is treated only for the open-loop system they constitute (as illustrated in Figure 3), the t-domain outputs require using the entire closed-loop compensatory tracking task control loop. The simulations feature the TV CE dynamics that transition from dynamics 1 (DYN1) (single-integrator-like dynamics) to dynamics 2 (DYN2) (double-integrator-like dynamics) denoted as DYN12 and modelled using a sigmoid function.

Following McRuer's Verbal Adjustment Rules (VAR), a distinct pilot model is derived corresponding to DYN1 and DYN2 of the CE [13][18][27]. It is essential to note that this method of obtaining the pilot employs a time-invariant approach, and the resulting pilot model can only accommodate the specific CE dynamics from which it is derived. The step-by-step modelling process is detailed below:

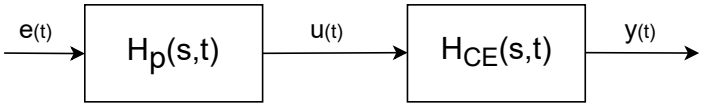

Fig. 3 Open-loop of the Compensatory Tracking Task

1. Controlled Element (CE) Dynamics:

The first step in designing the simulation involves defining a set of initial and final dynamics of the Controlled Element (CE). The transfer function of the TV CE, denoted as $H_{CE}(s,t)$, is structured according to Eq.(1), where $K_c(t)$ represents the TV CE gain, and $\omega_b(t)$ denotes the TV break frequency in rad/s. The rationale behind this structure is elaborated in Appendix A.

$$H_{CE}(s,t) = \frac{K_c(t)}{s(s+\omega_b(t))} \tag{1}$$

The VAR dictate that the CE dynamics determine the pilot parameter values, therefore, the CE dynamics are required to be modelled carefully. The values of $K_c(t)$, which only affect the scaling, are chosen based on typical values used in manual control tasks, with $K_{c1}(t) = 90$ and $K_{c2}(t) = 30$. On the other hand, $\omega_b(t)$ is a crucial parameter selected to change the behaviour of CE dynamics from single-integrator-like to double-integrator-like within the HO's range of perception. As the pilot can perceive changes within the range of $0.1 - 10$ rad/s, the break frequencies are selected to be $\omega_{b1}(t) = 20$ rad/s for DYN1 and $\omega_{b2}(t) = 0.2$ rad/s for DYN2. This configuration ensures that DYN1 possesses a pole beyond the pilot's range of perception, effectively rendering the CE a single-integrator. Conversely, DYN2 features a pole before the start of the HO's perception range, causing it to behave like a double-integrator. The selected values for the CE dynamics align with existing literature [25–27], as they meet the requirement of $\omega_b >> 1$ rad/s to exhibit single-integrator-like behaviour and $\omega_b << 1$ rad/s for double-integrator-like behaviour.

2. Parameter Function:

The next step, before obtaining the pilot models, involves selecting a parameter function to simulate the time-varying nature of the CE. The transition function selected in this study is the sigmoid function because of its ability to let the user select two essential parameters, namely, the rate of transition $G\ [s^{-1}]$ and the moment of maximum rate of transition $M\ [s]$, which is also the centre of the sigmoid. The transition is then defined for each required parameter P_1 to parameter P_2 that marks the start and end values. The equation of the sigmoid function is given below.

$$P(t) = P_1 + \frac{P_2 - P_1}{1 + e^{-G(t-M)}} \tag{2}$$

Since the rate of transition (G) significantly impacts the adaptive pilot's detection, five distinct values of G are selected for the simulations: 0.5, 2.94, 5.88, 50 and $100s^{-1}$. These values span a very slow change, like a change in aircraft's altitude, to a rapid change like a Stability Augmentation System (SAS) failure. The difference in the behaviour of the sigmoid function for different G values centred around the time duration (which is 90s for both simulations) at $M = 45$s, is depicted in Figure 4 using the slowest and fastest G values. This diagram accurately represents how all the required parameters vary with time. As the rate of transition G varies across different simulation scenarios, their

selection was based on the time required, in seconds, to transition from 5% to 95% of the final value, denoted as T_{tr}. For instance, in Figure 4 for $G = 0.5s^{-1}$, T_{tr} corresponds to the time duration between the two dashed lines. Consequently, the values of T_{tr} were determined to be $\approx$ 10, 2, 1, 0.10 and 0.05s, respectively. Lastly, in the simulations, the delay in the pilot's detection of change in CE dynamics is simulated by shifting the HO's sigmoid in time. That is, by keeping the centre of the pilot's sigmoid (M_{Pilot}) beyond M_{CE}.

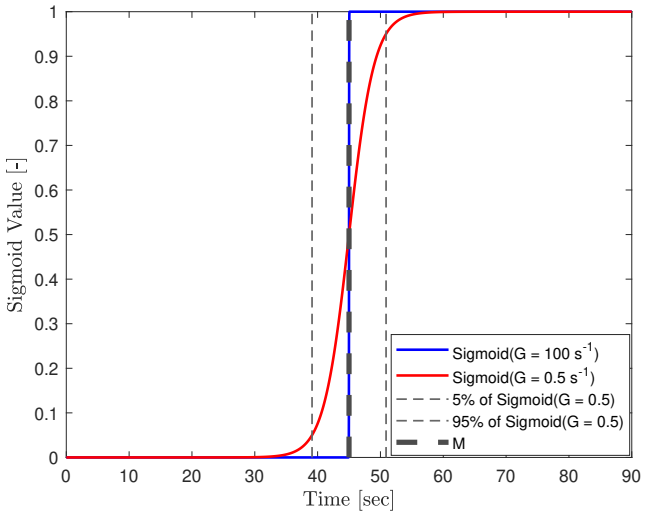

Fig. 4 Sigmoid function with varying rates of transition

3. Pilot Model:

The next essential step involves calculating the pilot models. The TV pilot transfer function $H_p(s,t)$ employed in the simulations is based on the simplified precision model proposed by McRuer and Jex [7] with the addition of the neuromuscular system (NMS) as seen in Eq.(3). Here, $K_p(t)$ represents the TV pilot gain; $\tau_L(t)$ signifies the TV lead time in seconds; $\tau_e(t)$ denotes the TV effective time delay in seconds; ω_{nm} is the natural frequency of the neuromuscular system in rad/s and ζ_{nm} the damping ratio of the neuromuscular system.

For both conditions of DYN1 and DYN2, the parameters of the neuromuscular system are kept constant, with $\omega_{nm} = 15$ rad/s and $\zeta_{nm} = 0.7$.

$$H_p(s,t) = K_p(t)(\tau_L(t)s + 1)e^{-s\tau_e(t)} \frac{\omega_{nm}^2}{s^2 + 2\zeta_{nm}\omega_{nm}s + \omega_{nm}^2} \tag{3}$$

The values of pilot model parameters $K_p(t)$, $\tau_L(t)$, and $\tau_e(t)$ are determined separately for DYN1 and DYN2 using the Verbal Adjustment Rules (VAR) prior to applying the parameter function. The VAR used for these calculations are specified in Eq.(4), with the bandwidth ω_i of the forcing function $f_t(t)$ taken as $\omega_i = 2.72$ rad/s. The motivation behind selecting this bandwidth is explained in subsubsection II.C.1. The numerical values of the CE and the obtained pilot model parameters for DYN1 and DYN2 are mentioned in Table 1.

$$\begin{aligned} \omega_c &= \omega_{c_0}(H_{CE}) + 0.18\omega_i \\ \tau_e &= \tau_0(H_{CE}) - \Delta\tau(H_{CE})\,\omega_i \\ \tau_L &= \frac{1}{\omega_b} \\ \phi_m &= \frac{\pi}{2} - \omega_c\tau_e \end{aligned} \tag{4}$$

With K_p obtained using:

$$|Y_{OL}(j\omega)|_{\omega=\omega_c} = 1.0 \tag{5}$$

B. Simulation Setup - Crossover Model Calcuations

This subsection provides details of the required setup to obtain the f-domain results. Upon obtaining the CE and pilot models, MATLAB's `Symbolic Math Toolbox` is utilised to generate a symbolic state-space (ss) representation of both the CE and pilot model such that, the elements of this symbolic state-space system can be updated with new values at each time step.

In the case of the state-space representation, each element of all four system matrices (A, B, C and D) is required to transition using the sigmoid function. As illustrated in Eq.(3), as the effective time delay (τ_e) is an exponential term, a second-order *pade approximation* is necessary to accommodate this parameter in the ss. Moreover, a state-space representation of the system is preferred because it was found that transfer functions transitioned using the scheduled parameter function (sigmoid) exhibited divergence from the required transition behaviour; the details of which are detailed in Appendix A.

Subsequently, the simulation is run to obtain the open-loop system at each time step using the updated state-space matrices ($H_{OL}(s) = H_P(s) \times H_{CE}(s)$). With the open-loop system calculated, the crossover frequency ω_c, the corresponding phase ϕ, and the phase margin ϕ_m are calculated from the frequency response of the $H_{OL}(s)$. Table 1 also states the crossover frequency and phase margin obtained for DYN 1 and DYN 2, the time-invariant conditions used as the start and end dynamics. The process thus yields the ϕ_m of the TV OL system, which can be further utilised to identify the Region Of Interest (ROI). The objective is to identify regions of instability/ reduced stability based on specific criteria - instability is characterised by a complete loss of phase margin ϕ_m i.e., the region (time duration) where the phase margin as a function of time $\phi_m(t)$ drops below 0°. On the other hand, for reduced stability, the criteria are set to contain the region where $\phi_m \leq 15°$. Therefore, the ROI starts when the time-varying simulation exhibits $\phi_m \leq 15°$, extending up to the moment of pilot detection ($T_{M_{pilot}}$) indicated by the location of the centre of the pilot sigmoid.

Table 1 CE and Pilot parameters for DYN1 and DYN2

Condition	K_c [-]	ω_b $[rad/s]$	K_p [-]	$\tau_L[s]$	$\tau_e[s]$	ω_{nm} $[rad/s]$	ζ_{nm} [-]	ω_c $[rad/s]$	$\phi_m[°]$
DYN1	90	20	0.7057	0.05	0.183	15	0.7	3.17	39.14
DYN2	30	0.2	0.0062	5	0.323	15	0.7	2.80	22.82

The selection of the ROI to start when $\phi_m(t) \leq 15°$ is based on the fact that an ideal (theoretical) pilot would adapt to the above simulation setup such that the phase margin goes from 39.14° to 22.82° as a sigmoid, while for a real-world scenario, there will be a decrease in $\phi_m(t)$ (see Figure 5) beyond the minimum value, obtained for DYN2.

C. Simulation Setup - Time Signal Calculations

The second set of results that deal with the t-domain, employ SIMULINK to simulate a compensatory tracking task. The control diagrams of the developed SIMULINK model are provided in Appendix B.

While the t-domain outputs utilize the same ss representation as their f-domain counterparts for the sigmoidal transitions of the CE and the pilot, additional modelling steps are required to obtain the time signals of the tracking task that include the incorporation of the forcing function ($f_t(t)$) and the remnant transfer function ($H_n(s,t)$).

1. Forcing Function ($f_t(t)$):

Table 2 lists the parameters of the sinusoids used to make the multisine forcing function $f_t(t)$ that follows the structure of Eq.(6). These sinusoids are identical to those employed by Terenzi et al. [26] in manual tracking experiments conducted at the Faculty of Aerospace Engineering, Delft University of Technology. This is done to ensure the availability of a reference for comparison in the event of implementing the signals for the experiment phase of this study.

$$f_t = \sum_{n=1}^{10} A_t[n] \sin\left(\omega_t[n]t + \phi_t[n]\right) \tag{6}$$

Here, $A_t[n]$ is the amplitude, $\omega_t[n]$ the frequency and $\phi_t[n]$ the phase shift of the n^{th} sine wave. The summation goes up to ten as there are a total of ten sinusoids that make the forcing function. The fundamental frequency, denoted as ω_m, is defined as $\omega_m = \frac{2\pi}{T_m}$, where T_m represents the measurement time. This parameter is maintained consistent with Terenzi's experiment [26] and Barragan's report [28], with a value of T_m = 30s. Although the total simulation duration for the time domain is 120s, the period of the forcing function is designed to be 30s. Therefore, ω_m = 0.209 rad/s.

Despite the simulation running for 120s, only the final 90s are utilized for signal analysis to derive the *steady-state* standard deviation for the single-integrator phase. Thus, the initial 30s serves as the run-in time. Consequently, M_{CE} is positioned at 75s for the Simulink model but can be interpreted to be at 45s given the reduced duration of the utilised signal.

Moreover, the bandwidth is selected to correspond to the frequency of the 4^{th} sinusoid, as the amplitudes of the subsequent sinusoids drop considerably [28].

Table 2 Parameters of the ten sinusoids that make the forcing function

k[−]	n_t[−]	ω_t $[rad/s]$	A_t $[rad]$	ϕ_t $[rad]$
1	2	0.419	$2.905 \cdot 10^{-2}$	2.841
2	5	1.047	$1.916 \cdot 10^{-2}$	3.319
3	9	1.885	$1.020 \cdot 10^{-2}$	0.718
4	13	2.723	$6.032 \cdot 10^{-3}$	0.768
5	19	3.979	$3.356 \cdot 10^{-3}$	2.925
6	27	5.655	$1.983 \cdot 10^{-3}$	5.145
7	39	8.168	$1.230 \cdot 10^{-3}$	2.085
8	51	10.681	$9.331 \cdot 10^{-4}$	0.383
9	67	14.032	$7.541 \cdot 10^{-4}$	0.763
10	83	17.383	$6.674 \cdot 10^{-4}$	3.247

2. Remnant Transfer Function ($H_n(s,t)$):

Humans are inherently non-linear [3]. In contrast to the crossover calculations, the time signals are influenced by the noise arising from the non-linear part of the pilot characterized by the remnant signal $n(t)$. The source of this non-linearity can be pure noise injection, non-linear operations and non-steady pilot behaviour in increasing order of impact [22]. Consequently, meticulous modelling of the remnant transfer function $H_n(s,t)$, which exhibits the structure given below, is imperative.

$$H_n(s,t) = \frac{K_n(t)}{(\tau_n s + 1)^m} \tag{7}$$

In the above equation, $K_n(t)$ represents the TV remnant gain, while τ_n denotes the time-invariant remnant time constant maintained at a constant value of 0.06s [24][29]. Moreover, based on the findings of Van Grootheest et al., [24], a second-order ($m = 2$) remnant transfer function is considered. Here, the value of the remnant gain relies on the required power ratio P_n (as seen in Eq.(8), which is defined as the ratio of power in the control input $u(t)$ attributed to the remnant (σ^2_{un}) to the total power in the control input (σ^2_u), where $\sigma^2_u = \sigma^2_{un} + \sigma^2_{uf_t}$. Given the varying nature of this ratio in real-world scenarios, different values of P_n are used in the simulations. The derivation of Eq.(8) can be found in Appendix C, which illustrates the stochastic nature of $n(t)$. It should be noted that W signifies the intensity of the white noise and is associated with the zero-mean Gaussian white noise input $w(t)$ to the remnant transfer function $H_n(s,t)$ as seen in Figure 1. Notably, $w(t)$ is modelled using unit intensity ($W = 1$).

$$K_n = \sqrt{\frac{P_n}{1-P_n} \times \frac{\pi \sigma^2_{uf_t}}{\int_0^\infty |\frac{1}{(\tau_n j\omega+1)^2}|^2 |\frac{1}{(1+H_p(j\omega)H_{CE}(j\omega))}|^2 W d\omega}} \tag{8}$$

In the above equation, to determine $K_n(t)$, a set of noise-free simulations with $w(t) = 0$ are conducted to obtain $\sigma^2_{uf_t}$ that describes the power in the control input due to the forcing function. Meanwhile, the required value of P_n is predefined in the simulation. P_n is set to vary; a range of percentage contribution of noise to the total power in the control input, with values of 5%, 10%, 15% and 20% are used for the Monte Carlo simulations. Finally, utilizing the same sigmoid function employed for the pilot model, the calculated remnant gain $K_n(t)$ is transitioned from DYN1 to DYN2.

Once the system is fully modelled, the Simulink model provides the primary signal values for the simulation duration of $T_m = 90$s. Subsequently, Matlab is employed to obtain the derivatives of these signals via backward finite

difference, yielding the remaining three candidate signals, namely, $\dot{e}(t)$, $\dot{u}(t)$, and $\dot{y}(t)$. This marks the end of the design methodology required to carry out the computer simulations.

The simulation setup and methodology described above were employed for Monte Carlo simulations to evaluate various parameters, with a primary focus on those significantly impacting the pilot's adaptive behaviour. These simulations encompassed a broad range of variations, including the CE rate of transition (G_{CE}), pilot rate of transition (G_{Pilot}), pilot gain multiplier ($K_p\times$) to account for a range of lazy to aggressive HO, and time delay of adaptation ΔM ($\Delta M = M_{pilot} - M_{CE}$) for the f-domain outputs. Subsequent t-domain outputs required three additional parameters: the power ratio (P_n), the number of forcing function realizations (f_t) each with a unique set of phase shifts, and the number of runs per forcing function realization (n_{f_t}) to account for varying pilot noise. This set of seven varying parameters yields a comprehensive dataset of simulation results. These results were subsequently subjected to statistical analysis to address the research question posed.

The values of a total of five varying parameters excluding the f_t realizations and number of runs per realization are mentioned in Table 3. The phase shifts of the ten f_t realizations having an average crest factor are mentioned in Table 4 while the number of runs per realization is set to ten. Here, ten realizations are used to avoid gradient effects on detection.

Table 3 Varying parameter values for the Monte Carlo simulations

G_{CE} $[s^{-1}]$	G_{pilot} $[s^{-1}]$	$K_p\times$ [-]	ΔM $[s]$	P_n [%]
0.5	0.5	0.25	0	5
2.94	2.94	0.50	3	10
5.88	5.88	0.75	6	15
50	50	1.0	-	20
100	100	-	-	-

Table 4 Phase data for the forcing function (f_t) realizations used in the Monte Carlo simulations

Phase Shift	Forcing Function Realization									
$[rad]$	1	2	3	4	5	6	7	8	9	10
ϕ_1	2.8410	2.3929	5.3762	6.2487	3.7558	3.2671	3.5350	1.4183	1.4442	0.3979
ϕ_2	3.3190	4.9697	0.6727	5.8687	1.9471	0.2482	2.1641	2.7251	2.9430	6.2707
ϕ_3	0.7180	5.3091	3.6048	4.9400	6.0459	0.9665	1.6746	2.0221	0.4288	1.8341
ϕ_4	0.7680	1.4863	3.4004	0.0782	0.5257	4.4574	4.6014	5.6634	1.4298	0.2662
ϕ_5	2.9250	3.0193	4.8348	6.0933	2.3904	3.8226	6.2706	5.7495	1.4750	4.5566
ϕ_6	5.1450	6.2722	3.9841	4.9810	3.0183	3.6774	4.5094	5.8329	2.0309	2.7780
ϕ_7	2.0850	3.6813	1.8678	5.4697	4.2311	5.1564	4.9301	1.1731	5.9036	4.4601
ϕ_8	0.3830	3.7568	4.9385	1.8165	1.8488	3.8601	3.1668	3.1755	2.1584	4.6433
ϕ_9	0.7630	0.3674	4.5615	5.2240	2.1321	4.8711	5.3231	4.6184	5.1776	2.9237
ϕ_{10}	3.2470	1.0865	0.2399	6.0067	4.3586	2.9775	5.9006	6.1829	2.5699	6.2330

D. Simulation Results

The Monte Carlo simulations resulted in 300 and 120,000 unique cases of f-domain and t-domain results, respectively. This section provides a comprehensive overview of the methodology employed for post-processing the results, aimed at determining two crucial parameters: the candidate signals for the model and the corresponding threshold values to obtain a high-accuracy model.

The t-domain signals superimposed with the ROI are depicted in Figure 6. This figure presents all six tracking task signals after removing the initial 30s run-in period with the ROI shown as the red-shaded region derived from plot(a) of Figure 5. This plot represents a typical output of the f-domain, which reveals the compromised OL stability. The specific case depicted on the left, and consequently within the time-signals, uses the following parameter values:

$G_{CE} = 0.5s^{-1}$; $G_{Pilot} = 0.5s^{-1}$; $K_p\times = 0.5$; $Delay\,(M_{pilot} - M_{CE}) = 6$s; $P_n = 20\%$; f_t realization #1 and run #1. Similarly, plot(b) in Figure 5 is representative of a variation in the rate of pilot adaptation, with $G_{Pilot} = 100s^{-1}$, to demonstrate how the rate of pilot adaptation affects the stability of the OL system. It can be observed that while the ROI remains unchanged, the recovery of OL stability is notably quicker, as evidenced by a deeper trough followed by a higher peak in $\phi_m(t)$. Also note that the start and end values of ϕ_m are higher than calculated in Table 1, which is a result of the reduced pilot gain that manifests itself in a reduced crossover frequency and hence, an increased phase margin.

1. Candidate Signals:

Like the example shown below, all ROIs are superimposed onto corresponding time signals. This approach leads to a single ROI corresponding to 400 cases of resultant tracking task signals because of the increased number of varying parameters in the t-domain. The combined results obtained are analysed to select the candidate signal of choice for the model. In a compensatory tracking task, the display only provides the HO with the error signal, while the effect of the control input on the error signal is the only other signal that the HO can experience. Therefore, the system output $y(t)$ and its derivative $\dot{y}(t)$ were removed from consideration. From the four remaining signals, $u(t)$ and $\dot{u}(t)$, were observed to show significant variation as a function of HO's control behaviour (aggressiveness: $K_p\times$) and the non-linearity from the remnant, for the same CE dynamics. Consequently, $u(t)$ and $\dot{u}(t)$ were also removed from consideration. This effect is illustrated in Figure 7 which uses the theoretical case of an ideal pilot (no adaptation delay i.e., $\Delta M = 0$).

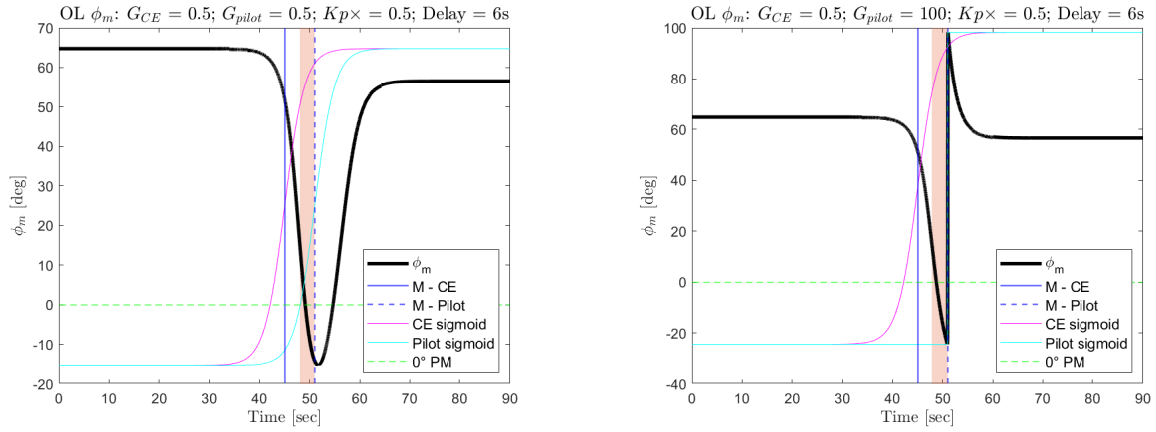

(a) $\phi_m(t)$ **with** $G_{\textbf{pilot}} = 0.5s^{-1}$ **(b)** $\phi_m(t)$ **with** $G_{\textbf{pilot}} = 100s^{-1}$

Fig. 5 Example result of the f-domain output with the Region Of Interest (ROI) in red. The ROI starts when $\phi_m(t) \leq 15°$ and ends at the moment of HO's detection (M_{Pilot})

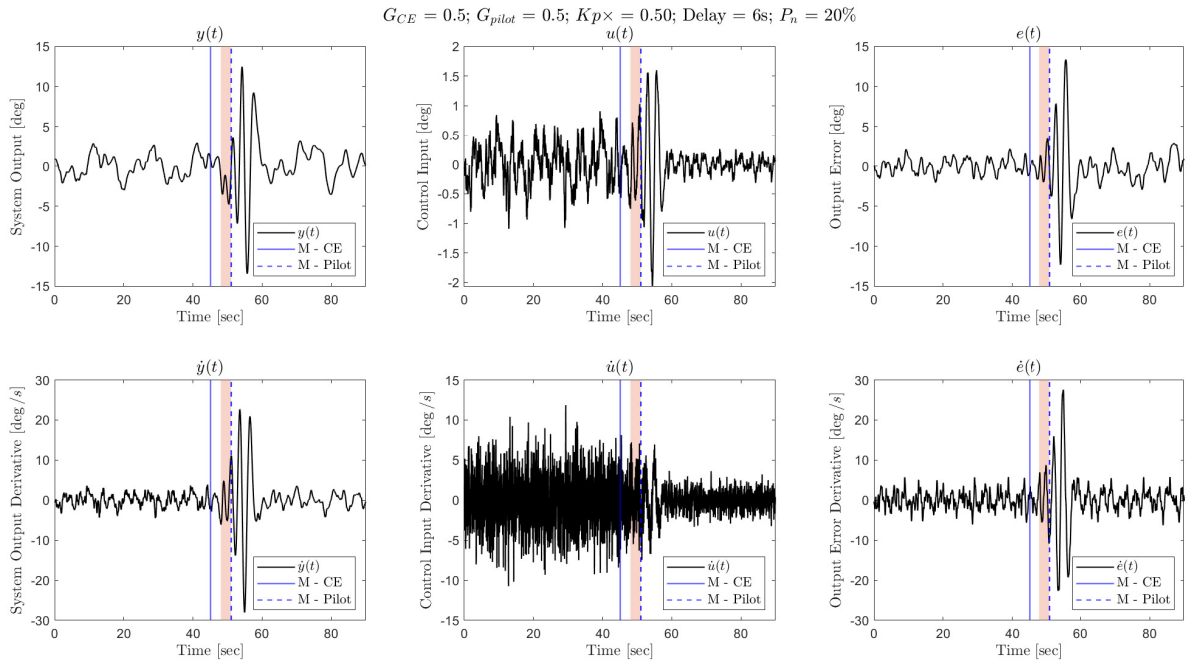

Fig. 6 Example result of the t-domain output with the time signals superimposed with ROI

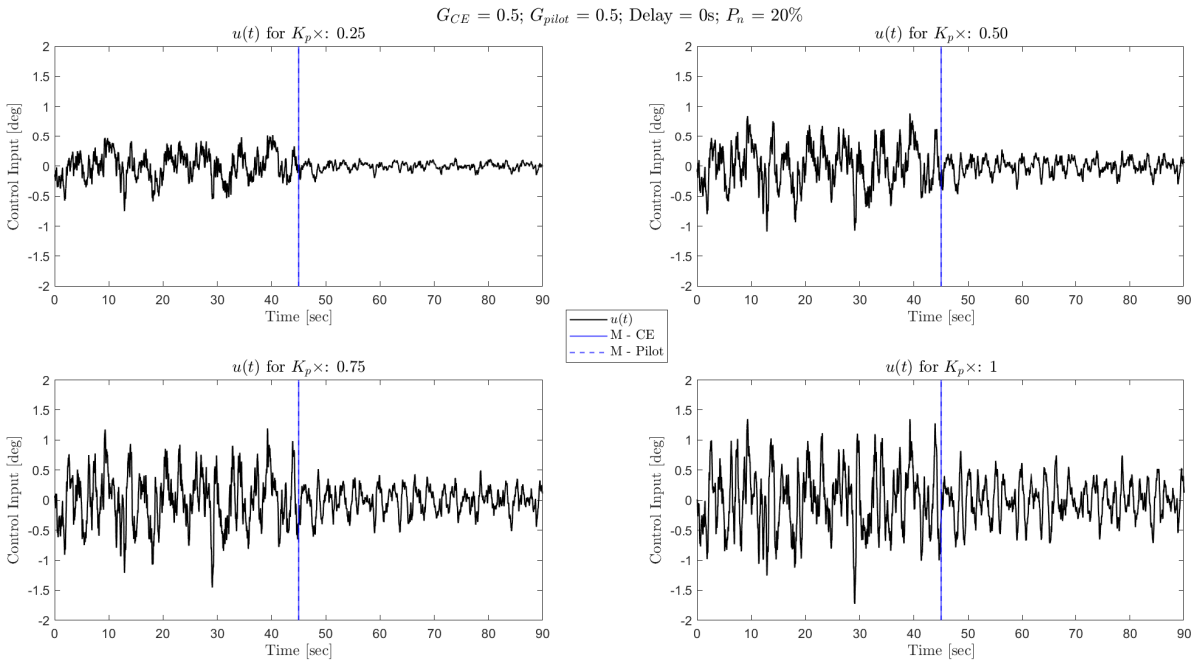

Fig. 7 Variation in control input signal $u(t)$ as a result of varying $K_p\times$ values for the theoretical case of an ideal pilot ($\Delta M = 0$)

Therefore, the error signal $e(t)$ and the error rate signal $\dot{e}(t)$ were identified as the two candidate signals of choice.

Notably, these signals were also previously selected as candidate signals in [10][20][28].

2. Model Accuracy and Threshold Values:

With the candidate signals obtained, their threshold values are obtained to accurately predict the pilot's detection of change in CE dynamics. To achieve this, the following methodology is employed: An optimal model that successfully predicts the pilot's detection of change in CE dynamics should have a threshold value such that it can account for naturally occurring variations in candidate signals during pre-transition conditions while also identifying unusual variations in these signals, within the ROI.

To implement this method, the steady-state DYN1 standard deviation σ is used as the statistical characteristic of the candidate signals, $e(t)$ and $\dot{e}(t)$. The standard deviation serves as a metric for assessing the variation of the signal within the Region of Interest (ROI) relative to its behaviour under steady-state conditions. Consequently, the variation of the signal is expressed as a multiple of the steady-state standard deviation, denoted by $n\sigma$, where n represents a positive value. Subsequently, it can be posited that there exists a specific value of n that maximizes the accuracy of the proposed model, where accuracy is defined as:

$$\% \, Accuracy = \frac{TP + TN}{TP + TN + FP + FN} \times 100 \tag{9}$$

In this context, TP (True Positive) denotes a correct trigger within the ROI, accurately predicting the pilot's detection of changes in CE dynamics (for the DYN12 condition). Conversely, TN (True Negative) contributes to the model's accuracy by remaining un-triggered in cases of no transition (i.e., for the DYN1 condition). On the contrary, FP (False Positive) and FN (False Negative) reduce the accuracy of the model. FP represents triggered detection occurring either before the ROI starts in cases of transition (DYN12 condition) or at any point throughout the runtime in the absence of transition (DYN1 condition), while FN indicates the absence of a trigger despite the presence of a transition (DYN12 condition).

As illustrated in Figure 8a and Figure 8b, these categories can be represented as segments within time signals, where p, q, r, and m are coefficients of σ representing unique choices of n. It is important to note that a run under consideration is categorized at the moment of the first crossing; once the threshold is crossed, i.e., at the instance of a certain trigger, the case is immediately categorized, and the model ceases further analysis of that signal. Additionally, the *steady-state* standard deviation required for determining threshold values (triggers for the model) is calculated using the 30s-60s window depicted in these figures to capture the *steady-state*. This requirement supports the addition of a run-in time of 30s for the time signals. Consequently, the average steady-state standard deviation values were found to be 0.87° for $e(t)$ and 2.08° for $\dot{e}(t)$ in the simulations.

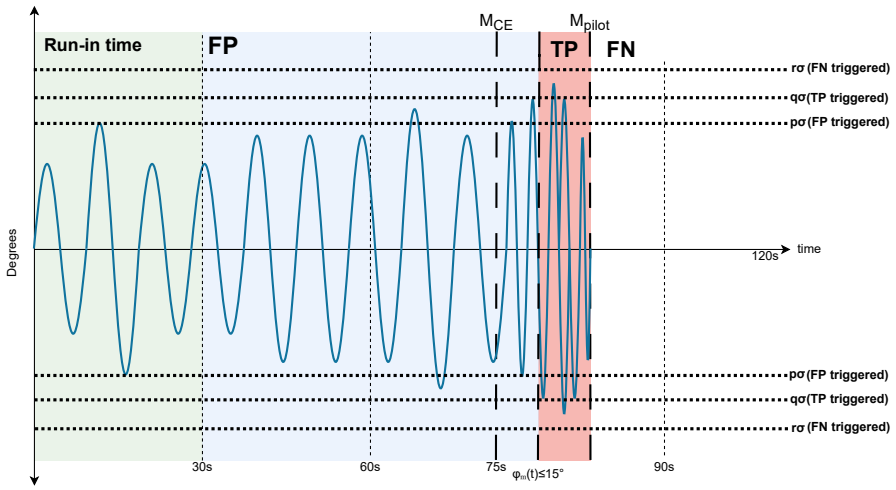

(a) DYN12 condition: Definition of TP, FP and FN

For example, in Figure 8a, the crossing of the $p\sigma$ threshold by the candidate signal within the blue region, representing the pre-transition condition, results in the classification of the case as a FP. Conversely, when the signal

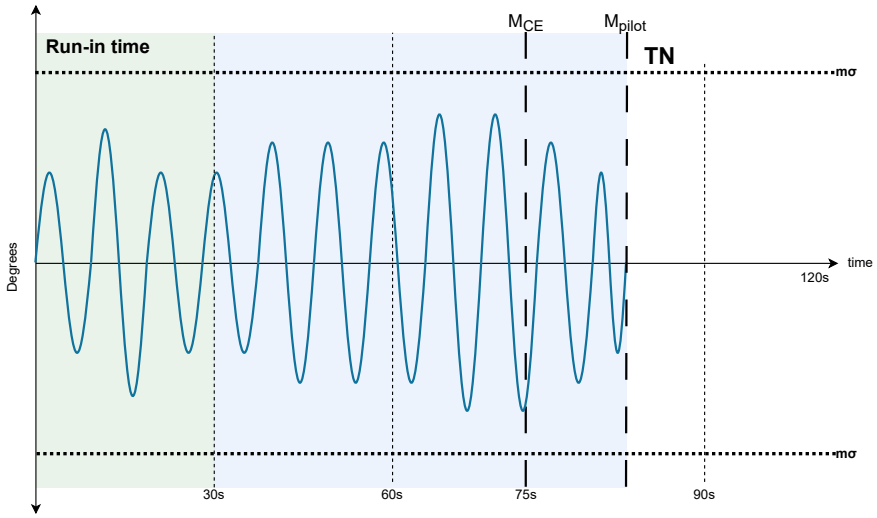

(b) DYN1 condition: Definition of TN

Fig. 8 Definition of accuracy parameters

crosses the threshold $q\sigma$ for the first time, as seen in the red region, it corresponds to a TP. However, if the signal fails to cross the trigger throughout the run, as observed for $r\sigma$, the case would be classified as a FN. This principle is also applicable to Figure 8b, which illustrates a run corresponding to the absence of transition, i.e., DYN1 condition. Here, crossing the threshold $m\sigma$ at any point results in classification as a FP, whereas the absence of a crossing leads to a TN classification.

Furthermore, the method of categorizing all signals involves an additional loop to iterate over a range of multiples of the steady-state standard deviation $n\sigma$, spanning from 2σ to 8σ with an increment of 0.1, for both the error signal $e(t)$ and the error rate signal $\dot{e}(t)$. This iterative process aids in identifying a threshold that results in the highest accuracy.

3. Results:

All cases obtained from the simulations (120,000) undergo the process explained above. Specifically, for each increment of the trigger value, the signals are examined from the first data point until they are successfully categorized, employing a step size of 0.01, consistent with the fixed step size used in Simulink. Subsequently, the simulation cases are categorized based on their G_{CE} values, to obtain an understanding of the model's performance for varying transition rates. The resultant percentage accuracy and trigger values are presented as a boxplot in Plot (a) and Plot (b) of Figure 9 to illustrate the spread of the results while Table 5 shows the mean accuracy and associated trigger values of these boxplots, denoted using circular black markers.

Analysis of the figures revealed several key observations. First, it was noted that the error signal outperforms the error rate signal as the rate of CE transition increases, resulting in higher accuracy. Conversely, the error rate signal gave higher accuracy for the slowest rate of transition and an approximately equal accuracy for $2.94s^{-1}$ as the error signal. The error rate signal performing better for slower transitions can also be seen by the increasing mean trigger values of the error rate signal going from left to right in plot(b) of Figure 9 which indicates that with faster transitions, the magnitude of the error rate signal in the ROI increases considerably. This is an intuitive result given that with a sudden change in CE dynamics, the loss in OL stability will be instant and hence the rate of change in error will be greater than the error signal.

Moreover, due to the large spread of percentage accuracy for the slowest transition rate of $G_{CE} = 0.5s^{-1}$, it was also decided to analyse the trigger values that resulted in the highest average accuracy per G_{CE} value. It was found that for the error signal, the highest average accuracy values of 63.85%, 87.84%, 92.37%, 94.19% and 94.38% were obtained at $3.3\sigma, 3.3\sigma, 3.3\sigma, 3.5\sigma$ and 3.5σ respectively, going from the slowest to the fastest rate of transition. Similarly, for the error rate signal, these values were found to be 67.32%, 89.05%, 92.71%, 81.47% and 70.89% for $3.7\sigma, 3.7\sigma, 3.9\sigma, 7.5\sigma$ and 8.0σ respectively.

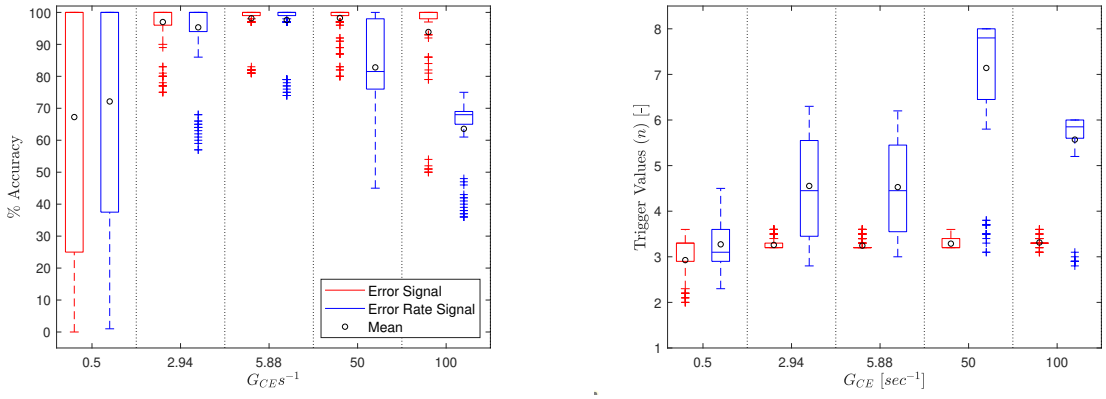

(a) Spread of Percentage Accuracy of the model

(b) Spread of Trigger Values ($n\sigma$)

Fig. 9 Percentage accuracy and correlated trigger values of the model based on error $e(t)$ and error rate $\dot{e}(t)$ signals

Table 5 Model performance for varying rates of transition

Signal	Parameter	G_{CE} [s^{-1}]				
		0.5	2.94	5.88	50	100
Error $e(t)$	% Accuracy	67.25	96.99	98.16	98.25	93.88
	Trigger Value(n)	2.93	3.26	3.25	3.29	3.31
Error Rate $\dot{e}(t)$	% Accuracy	72.14	95.32	97.63	82.80	63.57
	Trigger Value(n)	3.27	4.55	4.53	7.14	5.57

From these values, the first observation was that the model consistently obtains a lower accuracy for the slowest transition, which can be explained as follows: the slower transition in CE dynamics combined with the pilot model, even when the pilot model has an inherent delay, the simulated shifted change in the pilot model (depicting adaptation before detection), helps with maintaining the OL stability and as a result, the tracking error does not increase enough to cross the threshold value of the model. In other words, the slow change in CE dynamics causes the adaptive pilot to inherently and slowly adapt to the change, before detection, causing a gradual change in the system error which is then seen as a steady-state-like signal trend in the ROI. This behaviour can be observed in Figure 10, which shows the selected candidate signals of the same case as shown in Figure 6; here, the oscillations in the ROI are seen to be similar to the steady-state DYN1 part of the run only increasing considerably post the pilot's detection when the adapting pilot is in the *identification* and *adjustment* phase. Second, the error rate signal exhausts the range of $n\sigma$ values for the fast transition cases of $G_{CE} = 50$ and $100s^{-1}$ implying that the oscillations obtained for cases of larger delay like 6s have very high magnitudes which lead to a decrease in accuracy as a result of increase in FN.

Hence, based on the boxplots and the trigger values associated with the highest average accuracy, the thresholds (trigger values) for predicting the pilot's detection were selected as 3.3σ for the error signal $e(t)$ and 3.7σ for the error rate signal $\dot{e}(t)$. Notably, these values are comparable to the threshold values proposed in [21][28]. The application of the selected values on simulated signals is depicted in Figure 11. Here, it can be observed that the signals cross the respective trigger value within the ROI before the pilot's detection (M_{pilot}), thus resulting in the successful prediction of the pilot's detection of changes in CE dynamics. This figure represents, the final outcome of the computer simulations.

From the above observations, the following points were considered noteworthy before proceeding with the experimental phase:

1) The simulations indicate an increasing reliance on the error rate signal by the Human Operator (HO) to detect slow changes in CE dynamics. In contrast, the error signal is preferred for fast changes.
2) The percentage accuracy achieved at the selected trigger values suggests that the error signal consistently yields higher average accuracy calculated across all rates of transitions.

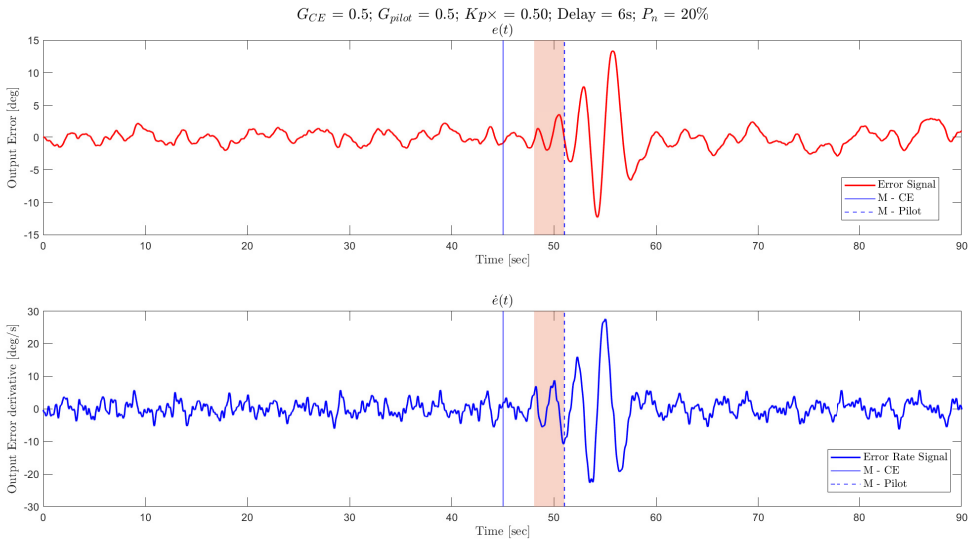

Fig. 10 Example case of slow CE transition, $G_{CE} = 0.5s^{-1}$

3) In addition to the compensatory display, it is of interest to consider the effect of the pursuit display on the HO's detection. Unlike the compensatory display, which solely presents the error, the pursuit display introduces additional strategies by displaying more information. Given that the model leverages both the error and error rate signals to predict the HO's detection of change in CE dynamics, it is anticipated that the model would exhibit superior performance for the compensatory display compared to the pursuit display.
4) On the contrary, given the increased strategies made available to the HO by the pursuit display, it can be argued that the detection of change in CE dynamics will be enhanced, leading to reduced detection lags.
5) The value of $G_{CE} = 50s^{-1}$ yielded very similar results to those observed for $G_{CE} = 100s^{-1}$, providing no additional insight. Therefore, $G_{CE} = 50s^{-1}$ should be excluded from the experiment.

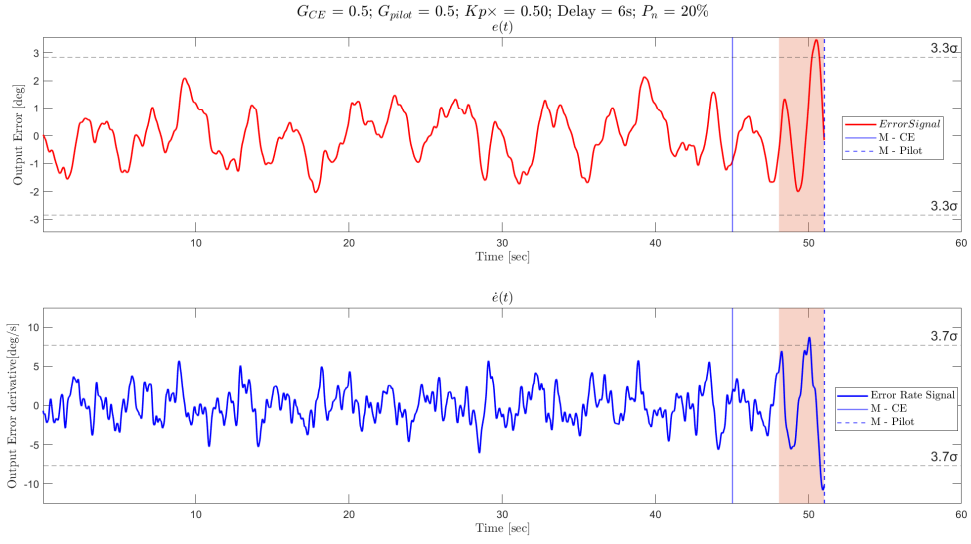

Fig. 11 Candidate signals $e(t)$ and $\dot{e}(t)$ superimposed with the ROI and the selected threshold values that form the model to predict the pilot's detection of change in CE dynamics

The results of the computer simulations thus lead to the following hypotheses for the experiment:

E. Hypotheses

- **Hypothesis 1 -** In the probabilistic period of reduced open-loop (OL) stability, for fast rates of transition ($5.88s^{-1}$ and $100s^{-1}$), the error signal $e(t)$ will result in higher accuracy of the proposed model i.e., the human operator will rely more on the error signal to detect a fast change in CE dynamics.
- **Hypothesis 2 -** In the probabilistic period of reduced open-loop (OL) stability, for slow rates of transition ($0.5s^{-1}$ and $2.94s^{-1}$), the error rate signal $\dot{e}(t)$ will result in higher accuracy of the proposed model i.e., the human operator will rely more on the rate of change of the error signal to detect a slow change in CE dynamics.
- **Hypothesis 3 -** The error signal $e(t)$ will have higher average accuracy calculated over the entire range of transition rates under consideration (0.05s to 10s).
- **Hypothesis 4 -** For a model that is based on error and error rate signals, the accuracy will be higher for the compensatory display than for the pursuit display.
- **Hypothesis 5 -** The use of the pursuit display will lead to reduced detection times when compared to the compensatory display.

These hypotheses will be referred to as **H(n)**, where $n = 1, 2, 3, 4$ and 5.

III. Experiment Setup

This section presents the design and data analysis methodology employed in the second phase of the research, in which a human-in-the-loop experiment was conducted to validate the developed model and hypotheses. The structure of this section is as follows: The control task required to be performed by the human operator is outlined in subsection III.A. Subsequently, subsection III.B details the apparatus utilized in the experiment. Following this, the independent variables and experiment conditions are explained in subsection III.C. Lastly, subsection III.D provides insights into the subjects and provided instructions while subsection III.E details the method developed for data analysis.

A. Experiment Design

The control task performed in this experiment is a single-axis ($roll$) tracking task using both, compensatory and pursuit displays; Figure 12 shows the displays as seen in the experiment. In the case of the pursuit display, the target signal (forcing function) was shown using the white square and the system output using the green square. This means that the participants controlled the green square, using a joystick on their right hand, with the primary objective being to minimize the error i.e., to keep the green square as close as possible (ideally inside) to the white square. Thus, the size of the white square is kept bigger than the green square. Similarly, in the compensatory display, the white square remains fixed at the centre of the display with the green square showing the error e between the target signal and system output. The objective of the task remained consistent, with the error approaching zero when the green square overlapped with the white square.

Additionally, participants were provided with a second joystick on their left hand. This additional joystick allowed participants to indicate when they detected a change in controlled element dynamics by pressing the red push button. The decision to use a separate joystick for this purpose was based on the findings of a previous experiment [21], which suggested that reaction times for detecting transitions could increase if both the primary task (minimizing the error) and the secondary task (pressing the button) were performed with the same hand. In the context of data analysis, the addition of this joystick helps mark the end of the region of interest (similar to the vertical M_{Pilot} line in the computer simulations) and obtain a measurement of subjective detection times.

Each run spanned a duration of 55s to 65s, during which the initial $5s$ /$10s$ /15s (variable) constituted the run-in time. Following this, the actual measurement period of 50s took place, thereby resulting in approximately two complete periods of the forcing function (T_m = 50s). The reason for having a variable run-in time is to counter the adaptive behaviour of HOs wherein with enough practice, they can use mental models to predict when the transition from DYN1 to DYN2 will take place. Furthermore, the centre M of the CE sigmoid (M_{CE} in the simulations) is positioned at 35s post the run-in time, resulting in a short-lived duration of 15s for the double-integrator condition (DYN2). This configuration allows for a full 30s measurement period for the single-integrator case spanning a complete period of the forcing function. The rationale behind shortening DYN2 is twofold: first, the model focuses on the pilot's detection of change in CE dynamics, which is independent of the pilot's performance post-detection; and second, the shortened runtime helps mitigate HO fatigue and reduces the overall duration of the experiment.

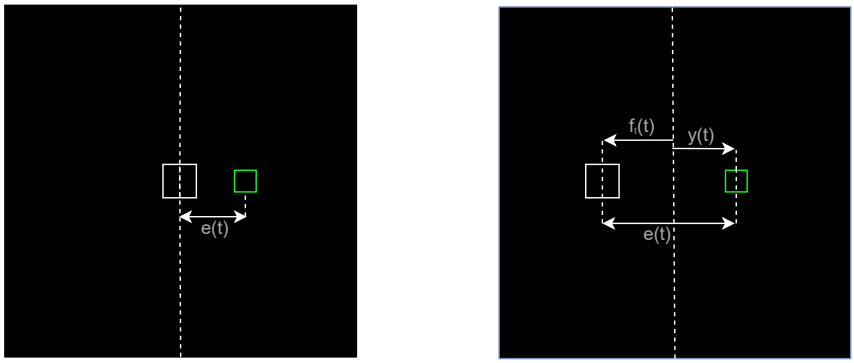

Fig. 12 Compensatory display(left) and pursuit display(right) as seen in the experiment setup (the dotted lines are for reference and are not a part of the actual display)

B. Apparatus

The experiment was conducted in a fixed-base simulator in the Human-Machine-Interaction Laboratory at the Faculty of Aerospace Engineering, TU Delft (Figure 13). Participants were seated on the right and utilized a side-stick located on their right hand to give control inputs. The movement of this side-stick was limited to the left and right ($roll - axis$) during the experiment. The maximum stick deflection was ±15° with the centre of the stick located 9cm above the axis of rotation. It had a stiffness of 3.54Nm/rad, a damping coefficient of 0.22Nms/rad, an inertia of $0.01 kgm^2$, and a breakout moment of 0Nm. Lastly, the additional left-hand joystick with a push-button (in red) is shown as image (b) in Figure 13.

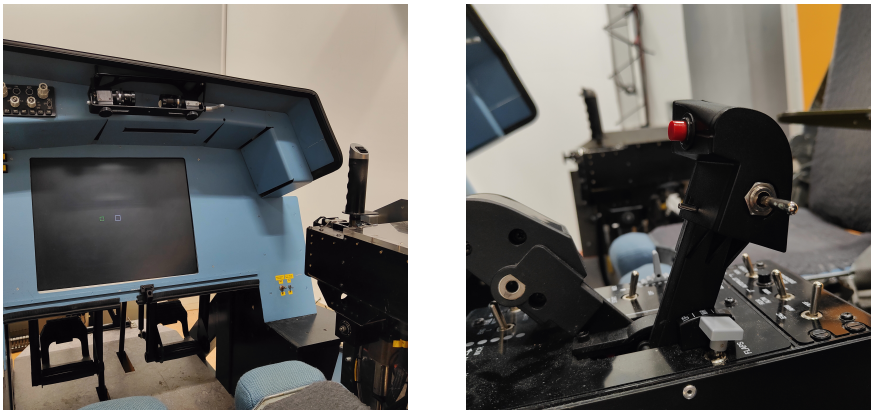

(a) Display and right-hand joystick

(b) Left-hand joystick with red push button

Fig. 13 Fixed base flight simulator at the HMI Laboratory of the Faculty of Aerospace Engineering, TU Delft

C. Independent Variables

The experiment consists of two independent variables: (1) display type and (2) rate of transition (G_{CE}). While the former is used to understand the effect of display type on the pilot and model's detection performance, the latter is varied to investigate different cases of TV CE dynamics.

The use of five forcing function (f_t) realizations per G_{CE} case serves to prevent participants from memorizing and anticipating the target signal, thereby improving the generalization of the model [21]. As such, the f_t realizations are not considered an independent variable in this experiment. Table 6 gives the phases of these realizations. Notably, realization #6 was only used for the training runs and is hence marked by "**T**". The verification of the experimental implementation of the simulated f_t realizations is provided in Appendix D.

Table 6 Phase data of the forcing function (f_t) realizations used in the experiment

Phase shift	Forcing Function Realization					
$[rad]$	1	2	3	4	5	6 (**T**)
ϕ_1	2.8410	0.7139	4.5118	5.7206	0.1654	5.9672
ϕ_2	3.3190	3.2003	3.4325	2.9644	5.9872	0.1799
ϕ_3	0.7180	1.5536	5.1605	0.4830	2.9338	3.9664
ϕ_4	0.7680	3.7235	0.8211	3.4292	4.2986	3.8851
ϕ_5	2.9250	1.4086	2.2409	0.6900	2.3155	6.1022
ϕ_6	5.1450	4.6871	3.7935	1.6630	1.5733	4.5394
ϕ_7	2.0850	1.8420	2.6510	4.7891	0.3204	2.8688
ϕ_8	0.3830	0.8073	1.3646	0.1654	4.2230	0.5136
ϕ_9	0.7630	0.5509	2.1103	1.8372	4.6754	0.5194
ϕ_{10}	3.2470	5.1815	6.2505	4.4607	5.7880	5.4870

Based on the independent variables, the tracking task is structured to contain two conditions divided further as five cases per display type, each consisting of five f_t realizations.

For the compensatory display, the experimental conditions are divided into two as follows:

- DYN1, representing a time-invariant, single-integrator-like condition, referred to as case $C1$.
- DYN12 comprises four cases characterized by varying rates of transitions in CE dynamics such that, $C12S1$ features the slowest transition using $G_{CE} = 0.5s^{-1}$; $C12S2$ with a moderately slow transition, specified by $G_{CE} = 2.94s^{-1}$; $C12F1$ with a moderately fast transition, specified by $G_{CE} = 5.88s^{-1}$ and $C12F2$ with the fastest transition using $G_{CE} = 100s^{-1}$.

Similarly, for the pursuit display, the cases are named $P1$, $P12S1$, $P12S2$, $P12F1$ and $P12F2$. The inclusion of the DYN1 condition aims to mitigate the subjects' anticipation and readiness for a transition in every run, thereby preserving the unpredictability of the experiment. Therefore, this condition is repeated four times (as illustrated by "(×4)" in Table 7), to have an equal quantity of transition and no-transition runs. The resultant setup thus contains a total of 80 runs per participant excluding the training runs.

Table 7 Experiment conditions with parameter values of the CE and sigmoid

Condition	Case	K_{c1} [-]	ω_{b1} $[rad/s]$	K_{c2} [-]	ω_{b2} $[rad/s]$	G $[s^{-1}]$	T_{tr} $[s]$	M $[s]$
DYN1	C1 (×4)	15	20	-	-	-	-	-
DYN12	C12S1	15	20	2	0.2	0.5	≈ 10	35
DYN12	C12S2	15	20	2	0.2	2.94	≈ 2	35
DYN12	C12F1	15	20	2	0.2	5.88	≈ 1	35
DYN12	C12F2	15	20	2	0.2	100	≈ 0.05	35
DYN1	P1 (×4)	15	20	-	-	-	-	-
DYN12	P12S1	15	20	2	0.2	0.5	≈ 10	35
DYN12	P12S2	15	20	2	0.2	2.94	≈ 2	35
DYN12	P12F1	15	20	2	0.2	5.88	≈ 1	35
DYN12	P12F2	15	20	2	0.2	100	≈ 0.05	35

Furthermore, the experimental conditions stated above show the initial and final values of the controlled element (CE) dynamics. Notably, these conditions maintain consistency with the simulations, with a difference seen in the CE gain values while the poles remain the same. This difference only changes the scaling while ensuring that the fundamental behaviour of the CE, whether single-integrator-like or double-integrator-like is preserved. Subsequently, the dependent variables are the RMSE, pilot model parameters, variance of the error and error rate signals, subjective detection lags and the HO's accuracy. This approach enables a direct comparison between the human operator's control

behaviour in the experiment and the theoretical results obtained from the simulations.

D. Subjects and Instructions

A total of twelve participants took part in the experiment with a within participant experiment design preferred for this study. The participants were all students and staff of the Faculty of Aerospace Engineering, TU Delft as they have satisfactory technical knowledge to perform the tracking tasks. Before commencing the experiment, participants received a comprehensive briefing on the experiment procedure with emphasis on the directive that their primary focus throughout the experiment should be the minimization of tracking error, with the button push serving as a secondary task. However, in the event of detecting a change in CE dynamics, the button push task could temporarily be treated as their primary objective.

The experiment consisted of two phases, a "training phase" and a "measurement phase". Before conducting the actual experiment in the measurement phase, several training runs were performed until a stable level of tracking performance was achieved. Except during the training runs, participants were not provided with feedback on their performance other than the root-mean-square error (RMSE) score displayed on the top-left of the screen at the end of every run. Post the training runs, data from five repetitions per experimental case was measured using different f_t realizations. The participants were made to follow the conditions as per a randomized order of 40 runs per display (20 runs of DYN1 and 20 of DYN12), which ensured that the different runs were evenly distributed across the subjects. Moreover, half the participants started with the compensatory display first while the other half started with the pursuit display first; these measures ensured that the statistical data analysis was not influenced by order effects or HO fatigue. The run tables used in the experiment can be found in Appendix H.

This experiment was reviewed and approved by the Human Research Ethics Committee (HREC) at TU Delft under application number 3866. The experiment briefing and consent form provided to the participants before starting the experiment are provided in Appendix I.

E. Data Analysis

The computer simulations assume that the pilot model uses the same transition function as the CE to adapt to the changing CE dynamics i.e., a sigmoidal change of their control behaviour. While this is a viable assumption to design time-varying mathematical models, the same cannot be assumed for human operators. Therefore, as the time-varying pilot model cannot be obtained as before, the start of the ROI, which is based on the onset of reduced open-loop stability (from $\phi_m(t) \leq 15^\circ$ in the simulations), cannot be calculated for experimental data. Consequently, the methodology used to implement the model on experimental data is as follows: it is argued that a time duration of *probable* compromise in OL stability will exist only on/after the onset of the designed sigmoidal transition of CE dynamics and the definition of the start of ROI is restructured based on this probability. **Hence, the ROI for experimental analysis starts when the CE dynamics have transitioned to** 50% **of their final (DYN2) steady-state parameter value**. Here, the selection of 50% transition is deemed suitable to cover all scenarios of probable OL instability safely based on a post hoc analysis of the experiment data, conducted to verify the validity and sensitivity of this selection, provided in Appendix G. Another advantage of using this value is the fact that all sigmoids, irrespective of their G value, attain 50% transition at the same moment in time i.e., 50% transition corresponds to M, the centre of the sigmoid placed at 35s in the experiment. In contrast, for all other percentage transition values, the moment in time to attain the required percentage will vary based on the G value, making the comparison of parameters like the detection lag as a function of G value, difficult to interpret. For example, the moment of 5% transition for $G = 0.5s^{-1}$ occurs at $t = 29.14$s while for $G = 100s^{-1}$ this value shifts to $t = 34.99$s leading to a difference of 5.8s. **It is noted that the moment of end of ROI retains its definition from the simulations - at the moment of the pilot's detection of change in CE dynamics which, for experiments, is obtained from the time-stamp of the button press.**

The next step is to analyse human error that affects the four parameters (TP, TN, FP and FN) that decide the accuracy of the proposed model. In the results of the computer simulations, the FP and FN parameters are defined based on incorrect classification by the model. However, in the experiments, the human operator is prone to three types of errors: an early (before the transition begins) button press in a run having a DYN12 condition, classified as FP; a button press in a run having a DYN1 condition, also classified as FP; and failure to detect the change in CE dynamics i.e., no button press in a run featuring a DYN12 condition leading to a FN classification. These human errors result in the absence of a pre-defined duration used as the ROI and hence need to be corrected. The corrections made for the human errors are mentioned in Table 8, which results in the model processing the experiment data that now adheres to the required signal conditions of Figure 8a and Figure 8b.

Table 8 ROI Corrections for human error

Experiment Condition	Human error	Correction
DYN12	FP	ROI start: at 50% transition; ROI end: extended to end of run
DYN1	FP	ROI removed
DYN12	FN	ROI start: at 50% transition; ROI end: extended to end of run

The result of pre-processing the data is shown in Figure 14 where a HO's TP case is shown for a $C12S1$ experiment condition with the ROI, and the 5% and 95% sigmoid values that define T_{tr}. In this figure, the initial 30s of the plot represents the *steady-state* DYN1 condition, followed by the CE transition centred at M_{CE} at 35s, and finally, 15s of DYN2 condition from $35-50$s. Lastly, the sigmoid (in pink) depicting the CE transition is shown to scale with respect to the X-axis.

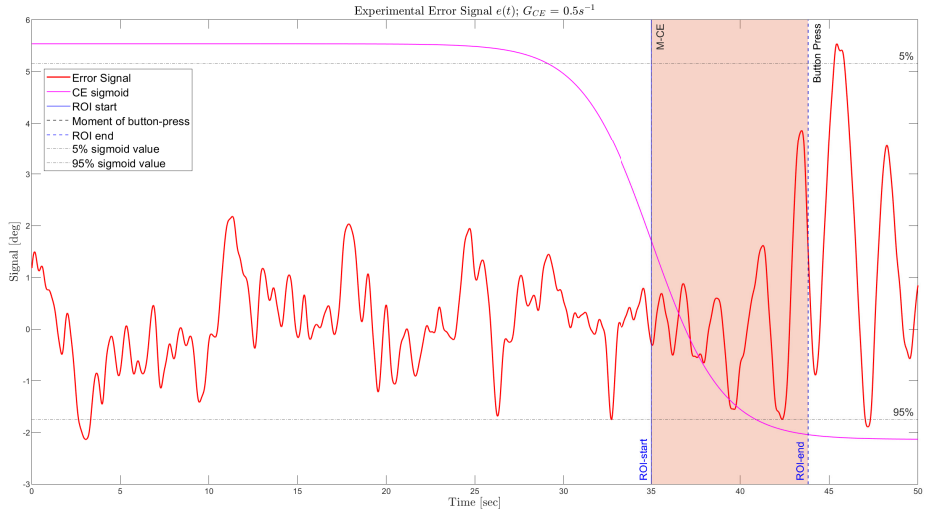

Fig. 14 Example of measured error signal $e(t)$ after pre-processing, $G_{CE} = 0.5s^{-1}$

IV. Experiment Results

This section analyses the subject and model's performance using experimental data. Initially, this section discusses the pre-transition metrics of Root Mean Square Error (RMSE), crossover frequency (ω_c) and phase margin (ϕ_m) followed by in-transition (ROI) metrics like the variance of signals (σ_e^2 and $\sigma_{\dot{e}}^2$) and detection lags providing insights into the quality of the experimental data and the impact of the independent variables on the HO's performance. The focus is then shifted to the model's accuracy and performance for the gathered experimental data.

A. Pre-transition Metrics

The RMSE scores discussed in this section are related to the DYN1 part i.e., the first 30s of all runs performed by each subject irrespective of the condition (DYN1/DYN12) of the run, thus they are independent of the G_{CE} values. The RMSE helps analyse a subject's performance w.r.t the other subjects in the experiment and draw a comparison between the performance achieved in compensatory and pursuit displays. Figure 15 shows the boxplot of RMSE scores with the global mean values per display as colour-coded horizontal lines in plot(a) and black circular markers in plot(b). It can be seen that the pursuit display helps all subjects have a lower error as compared to the compensatory display, which can be explained by the explicit availability of the control output $y(t)$ and target signal $f_t(t)$ in addition to the system error signal. Moreover, as seen in plot(a), there is an evident difference in tracking performance between different participants. However, it is typical to anticipate different skill levels from different subjects in any experiment, and the

variation in the dataset is not large enough to warrant the identification of specific participants or groups thereof as outliers or unskilled. This is backed by the fact that there are no outliers in plot(b) which has twelve data points per boxplot corresponding to the mean RMSE score of the twelve subjects. Therefore, these results suggest that the quality of the experiment data is good, and all participants can be considered skilled HOs. Moreover, the RMSE values show a clear difference in global mean values with the compensatory display (red) having a mean value of 0.77° and 0.66° for the pursuit display (blue); this shows that the two mean values are significantly different, $t(11) = 5.676, p < 0.001$, consistent with the fact that the pursuit display helps achieve better performance (lower error) in tracking tasks [30].

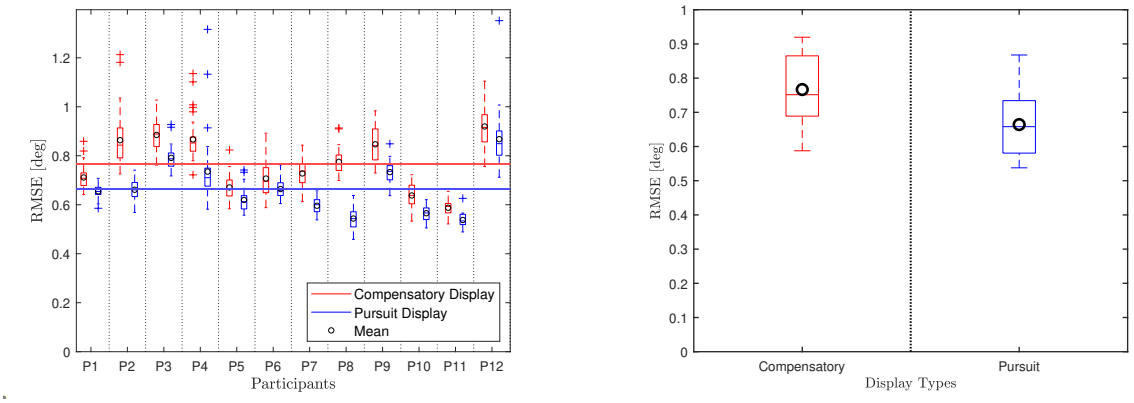

(a) RMSE values per subject **(b) RMSE values per display type**

Fig. 15 RMSE values per subject (left) and per display type (right) in pre-transition (DYN1) phase

Moreover, to characterize the participants in the experiments, the pilot model parameters are identified using a Maximum Likelihood Estimation (MLE) process, which uses the same pilot model structure shown in Eq.(3). The detailed results of this process are provided in Appendix E; the use of MLE becomes possible because of the 30s DYN1 part of all runs. Utilizing the derived pilot model in combination with the CE dynamics, the crossover frequency (ω_c) and phase margin (ϕ_m) are obtained using OL bode-plot data.

The obtained average crossover frequency (ω_c) and phase margin (ϕ_m) for all subjects per display type are shown in Figure 16 with a mean value of 2.73 rad/s and 64.19° for the compensatory display and 2.81 rad/s and 60.61° for the pursuit display. The paired T-test statistically validates the visual observation that the display types do not affect these metrics; with $t(11) = 0.349, p = 0.734$ for the crossover frequency and $t(11) = 1.637, p = 0.130$ for the phase margin. Notably, the mean crossover frequency has approximately the same value as that of the f_t bandwidth which suggests that the HOs actively tried to keep the tracking error at the minimum i.e., the pilot adjusted their gain to place the ω_c at ω_i to address the entire band of frequencies (the HO acts as a low-pass filter) while maintaining good stability margins. This also highlights the relationship between performance and stability ($\omega_c \propto \frac{1}{\phi_m}$).

While the mean values align with $\omega_c = 2.77$ rad/s and $\phi_m = 55.6°$ obtained for the pursuit display in Barragan's report [28]. The mean value of the crossover frequency is found to be higher than found in [21] and [26] with the probable reason being the selected CE dynamics, which by the virtue of the poles selected, behaves more like a pure-single integrator than used in the mentioned studies. The values for both these metrics further indicate that the quality of the experimental data is good. Lastly, the relationship between RMSE and crossover frequency can be seen to be consistent in that subjects with lower RMSE scores generally had higher crossover frequencies with the Pearson correlation coefficient found to be high [31] for the compensatory display, $\rho = -0.812, p < 0.001$ as well as for the pursuit display with $\rho = -0.979, p < 0.001$.

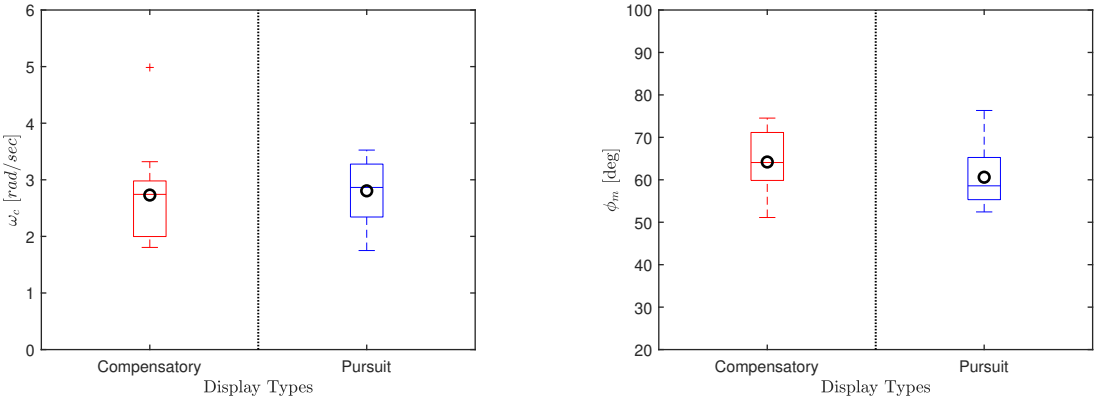

(a) Crossover frequency (ω_c) **(b) Phase margin (ϕ_m)**

Fig. 16 Crossover frequency and phase margin per display type in pre-transition (DYN1) phase

B. In-transition (ROI) Metrics

The performance metrics discussed above are characteristic to the DYN1 part of the experiment. Given the study's focus on time-varying conditions, the subsequent metric under consideration is the variance of candidate signals $e(t)$ (σ_e^2) and $\dot{e}(t)$ ($\sigma_{\dot{e}}^2$) within the ROI. The variance aims to explain the impact of different G_{CE} values on the signals and consequently, on the HO's performance during the transition. For reference, the value of σ_e^2 and $\sigma_{\dot{e}}^2$ in the steady-state DYN1 condition of the experiment is found to have a global average (averaged across all runs for all participants) of $0.58 deg^2$ and $5.97 deg^2$ in the compensatory display and $0.44 deg^2$ and $4.84 deg^2$ for the pursuit display, respectively. In comparison, for the computer simulations, the values of σ_e^2 and $\sigma_{\dot{e}}^2$ were $0.75 deg^2$ and $4.33 deg^2$ respectively, which are similar and thus lend support to the fidelity of the computer simulations.

Plot(a) and plot(b) of Figure 17 show the variance in ROI for the error signal and the error rate signal, respectively with the coloured horizontal lines depicting the global DYN1 average values mentioned above. Wherein in plot(a), the mean values of the error signal for the compensatory display are found to be 1.03, 2.31, 2.96, and $3.18 deg^2$ and; 0.69, 1.28, 1.91, and $1.98 deg^2$ for the pursuit display. Similarly, in plot(b), for the error rate signal the mean values are 9.17, 14.27, 17.83, and $19.15 deg^2$ for the compensatory display and; 6.48, 8.82, 13.05, and $13.09 deg^2$ for the pursuit display. Given that these values are from within the ROI, it is important to note that they are related to runs that belong to the DYN12 condition.

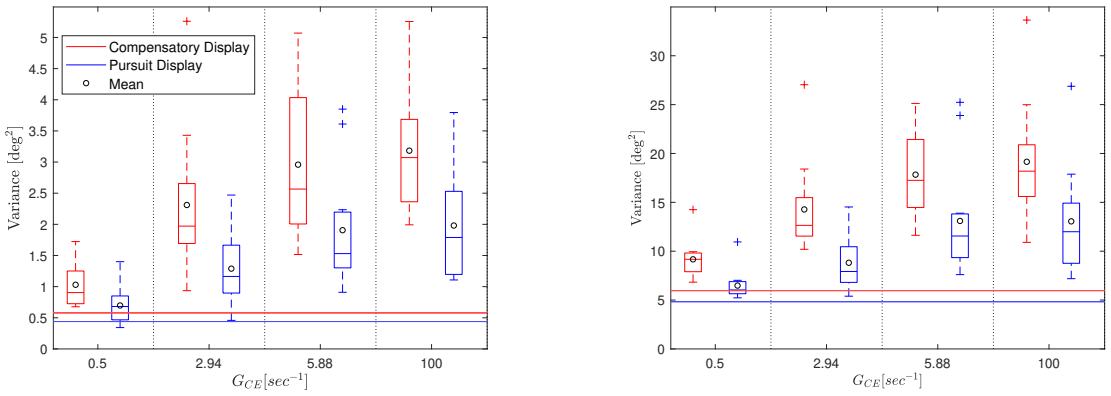

(a) Variance of error signal $e(t)$ in ROI **(b) Variance of error rate signal $\dot{e}(t)$ in ROI**

Fig. 17 Variance of error signal $e(t)$ (left) and error rate signal $\dot{e}(t)$ in ROI per G_{CE} value for both display types (the colour-coded horizontal lines correspond to the global DYN1 (pre-transition) average values)

Several observations emerge from this analysis. First, it is anticipated that the error rate signal, being the derivative of the error signal, will exhibit larger magnitudes. Second, both the signals notably demonstrate higher magnitudes within the region of interest (ROI) compared to the steady state, particularly evident in conditions with high G_{CE} values, where the step-like change in CE dynamics induces increased error and error rate. Additionally, the lower variance observed in slower transitions is likely associated with longer detection times, a concept discussed later. Third, the reduced variance in the pursuit display suggests enhanced tracking performance, which may also be supported by reduced detection lags. Based on these observations, the variance values in the ROI encourage further exploration into detection lags and their statistical correlation.

Thus, the next step in evaluating performance is to analyze the detection lag of the subjects deriving further insight into the transition phase of the runs. This metric is related to how quickly subjects detect the change in CE dynamics. It will be demonstrated that detection lags vary, based on both the display type and the G_{CE} value, highlighting the relationship between these variables. The boxplots shown below in Figure 18 display the detection lags per G_{CE} value (using only the TP category of the DYN12 runs) for the compensatory display (in red) and the pursuit display (in blue).

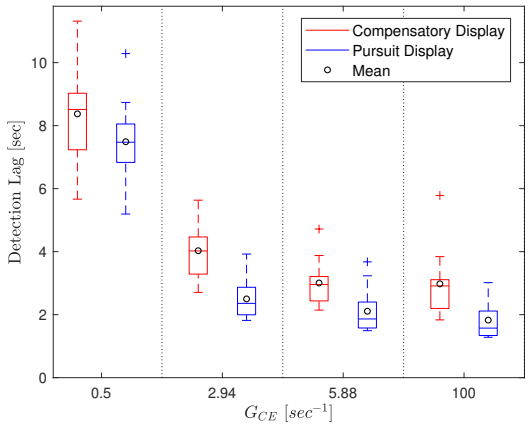

Fig. 18 Temporal scale of subject's detection lag per G_{CE} value for both display types

As mentioned in subsection III.E, the reference time to quantify detection lag is defined as the point when the CE dynamics have transitioned to 50% of their final DYN2 value (see Figure 14), i.e., the origin of the Y-axis in the above plot corresponds to t = 35s of the experiment. Consequently, as only TP cases can be considered to obtain the detection lag; in the case of the compensatory display, this led to the exclusion of 15 FP and 4 FN from a total of 240 DYN12 runs and 2 FP and 6 FN for the pursuit display.

For the above figure, two important observations were made: (1) for the boxplot of $G_{CE} = 2.94s^{-1}$ for the compensatory display, a value for subject 2 (P2) was missing because they had no TP detections for this G_{CE} value and (2) the mean detection lags in the pursuit display tend to be lower across all G_{CE} values compared to the compensatory display (like the variance values). Here, for the compensatory display, the mean detection lags are found to be 8.37, 4.03, 3.01, and 2.98s for G_{CE} = 0.5, 2.94, 5.88, and $100s^{-1}$ respectively. For the pursuit display, the mean values are 7.48, 2.50, 2.11, and 1.83s, respectively. The lower detection lags observed for the pursuit display show that the choice of display type significantly affects the HO's detection process with $F(1, 11) = 18.588$, $p = .001$, partial $\eta^2 = 0.628$. The observed consistent decrease in detection lag with an increase in transition rate is also validated with repeated measures ANOVA, here, Mauchly's test indicated that the assumption of sphericity had been violated, $\chi^2(5) = 19.344$, $p = 0.002$ and therefore degrees of freedom were corrected using Greenhouse-Geisser estimates of sphericity ($\epsilon = 0.474$) resulting in $F(1.421, 15.634) = 348.264$, $p < 0.001$, partial $\eta^2 = 0.969$. In contrast, given the relative decrease in detection lag by using the pursuit display remains approximately the same across all G_{CE} values, it can be concluded that the interaction effects of both these independent variables are not significant, $F(3, 33) = 1.091$, $p = 0.367$, partial $\eta^2 = 0.090$.

Comparing these findings to previous experiments, it is notable that the detection lags for $G_{CE} = 100s^{-1}$ are considerably lower than those found in studies utilizing a compensatory display by Van Ham [21] and Plaetinck [25], the median detection lags were reported to be 6.6s and 5.2s respectively. On the contrary, the detection lag for

$G_{CE} = 100s^{-1}$ in the pursuit display matches the detection lag value of 1.82s found in Barragan's report [28].

This disparity in detection lag for $G_{CE} = 100s^{-1}$ in [21][25] is likely due to ω_{b1} which was kept to be 6 rad/s in those experiments while this study utilizes 20 rad/s (same as [28]) making the system respond more like a pure single-integrator, and hence makes the difference between single-integrator and double-integrator more distinct and easier to detect. Furthermore, the phenomenon of slower rates of transitions corresponding to higher detection lags can be correlated to the findings of the computer simulations in that the slow changes lead to fewer changes in signal magnitudes in the ROI and hence the time taken by the adaptive HO to detect the change in CE dynamics increases. This phenomenon can be extrapolated such that we can expect the model to have lesser accuracy for such slower transitions in line with the computer results (subsection II.D).

Lastly, the variance of the signals in ROI and the detection-lag can be seen to have a negative correlation, with a Pearson correlation coefficient of $\rho = -0.461, p < 0.01$ for the σ_e^2 - detection lag and $\rho = -0.457, p < 0.01$ for $\sigma_{\dot{e}}^2$ - detection lag.

C. Model Accuracy

In Figure 19, the model's accuracy is depicted independently for the compensatory and pursuit displays across all experimental conditions. Each boxplot comprises 12 data points representing the mean accuracy of the model for the twelve subjects. Given that the DYN1 condition (pink region) constitutes 50% of all experimental runs, the mean value per subject is derived from 20 runs. Conversely, for DYN12 conditions (blue region), each data point is a mean value per subject derived from 5 runs. In the figure, the red boxplots represent the model's accuracy using the error signal $e(t)$, while the blue boxplots correspond to the model's accuracy using the error rate signal $\dot{e}(t)$. Lastly, the black boxplots show the model's combined accuracy i.e., using both, the error and error rate signals.

Here, Table 9 gives the associated numerical values (black circular markers in the plots) while Appendix F provides categorical ($TP/TN/FP/FN$) values for this data. The model demonstrates high accuracy for the DYN1 condition, with combined model accuracy values of 96.25% and 98.33% for the compensatory and pursuit displays, respectively. Interestingly, this is the only condition where the model exhibits a higher percentage accuracy for the pursuit display. In contrast, for the DYN12 condition, the combined model gives an average accuracy of 88.33% for the compensatory display and 81.04% for the pursuit display, which is relevant to **H(4)**. For the study's focus on varying rates of transition, and given that the model demonstrates higher accuracy for the compensatory display, this phenomenon can be explained as: in the pursuit display, additional signals are available, providing the human operator with more strategies to detect changes in CE dynamics. However, the model developed in this study relies solely on the error signal and its derivative, which are explicitly available in the compensatory display. Consequently, the human operator relies more on these signals to detect changes in CE dynamics.

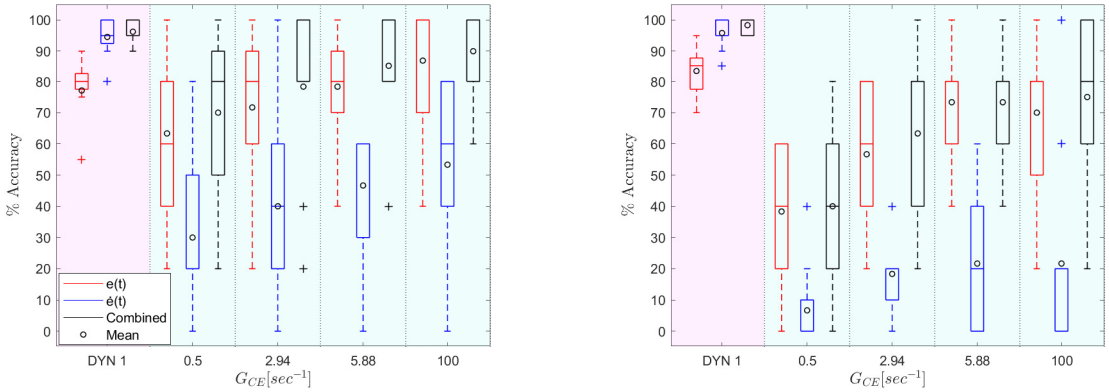

(a) Model accuracy for compensatory display

(b) Model accuracy for pursuit display

Fig. 19 Model's accuracy on experimental data using the error signal, error rate signal and both signals combined. Shown for DYN1 condition and DYN12 conditions

For the compensatory display, from a total of 480 runs (designed as 240 TP and 240 TN) conducted throughout the experiment, the combined model categorized 194 runs as TP, 231 as TN, 27 as FP and 28 as FN with the lowest

accuracy of 70.00% related to the slowest rate of transition as expected, and the highest accuracy of 90.00% for the fastest rate of transition. The same trend persists when the model explicitly uses the error signal and error rate signals. While **H(1)** was supported by high model accuracy, **H(2)** lacked support from the model's findings. A probable explanation for the lack of higher accuracy using error rate signal for slower rates of transition can be that the HO uses some filtered form of $e(t)$ to detect the changes in CE dynamics or the $\dot{e}(t)$ is used only as a secondary identifier by the HO. The latter explanation is backed by all blue boxplots (for DYN12) extending downwards to 0% accuracy for a subject either as a whisker or within their Inter Quartile Range (IQR). For reference, Table 9 also gives the subject's average accuracy for all cases.

Table 9 Subject and Model's accuracy for experiment data

Condition	Case	Subject's Accuracy	**% Accuracy based on Signal Used**		
			$e(t)$	$\dot{e}(t)$	Combined
DYN1	C1	93.75	77.08	94.58	96.25
DYN12	C12S1	88.33	63.33	30.00	70.00
DYN12	C12S2	90	71.67	40.00	78.33
DYN12	C12F1	95	78.33	46.67	85.00
DYN12	C12F2	95	86.67	53.33	90.00
DYN1	P1	98.75	83.33	95.83	98.33
DYN12	P12S1	88.33	38.33	6.67	40.00
DYN12	P12S2	100	56.67	18.33	63.33
DYN12	P12F1	98.33	73.33	21.67	73.33
DYN12	P12F2	100	70.00	21.67	75.00

Furthermore, the fact that $G_{CE} = 0.5s^{-1}$ runs had the lowest accuracy amongst subjects and the model for both displays suggests that the continuous adaptation by the HO to slow-changing CE dynamics makes the transition more difficult to detect. While the combined model can be used increasingly for faster rates of transition in the compensatory display, the model's low accuracy in the pursuit display, suggests that the HO relies more on either control input $u(t)$ or system output $y(t)$ or a combination of the available signals. For the pursuit display, the model categorized 151 runs as TP, 236 as TN, 30 as FP and 63 as FN. Here, the twofold increase in FN also indicates the improved tracking performance (lower RMSE $\rightarrow e(t)/\dot{e}(t)$ not crossing the selected $n\sigma$ trigger value) for the pursuit display, leading the model to categorize DYN12 runs as DYN1.

It is further observed that for the compensatory display, for the DYN12 condition, using the error-signal-based model leads to a higher average accuracy of 76.35% than using the error rate-signal-based model which has an average accuracy of 66.15% supporting **H(3)**. Therefore, it can be concluded that the accuracy of the model is affected by the display type, $F(1, 11) = 7.942$, $p = 0.017$, partial $\eta^2 = 0.419$. Similarly, the observation that increasing transition rates lead to increased model accuracy helps conclude that the rate of transition significantly affects the model's performance, $F(3, 33) = 15.589$, $p < 0.001$, partial $\eta^2 = 0.586$. However, the interaction effects of display type and rate of transition on the model's accuracy are not significant, $F(3, 33) = 0.094$, $p = 0.963$, partial $\eta^2 = 0.008$.

When Figure 19 is compared to Figure 9 of the computer simulations. It is observed that (in line with the findings of the simulations) with increasing transition rates, going from left to right in the plots, the accuracy of the model increases for the error signal i.e., the skilled HO relies more on the error signal for faster rates of transition. However, the simulation's trend of the error rate signals is not validated by the experiments. Lastly, for the temporal scale of the model's performance, which is crucial for the model's accuracy, Figure 20 shows the spread of moment in time when the model is triggered for varying rates of transition. The mean values of these boxplots are 7.98, 2.65, 1.84 and 1.63s for the compensatory display and 5.92, 1.68, 1.53 and 1.02s for the pursuit display going from left to right, respectively. When these values are compared with subjective detection lags mentioned in subsection IV.B it is observed that the time difference between the HO's detection and the model trigger has a mean value of 1.97, 1.30, 1.08 and 1.62s for the compensatory display and 2.07, 0.83, 0.62 and 0.81s for the pursuit display corresponding to $G_{CE} = 0.5$, 2.94, 5.88 and $100s^{-1}$ respectively. These values suggest that the mean values of the model's detection lag are not significantly different, $t(3) = 2.965$, $p = 0.081$ for the two displays. Moreover, these values are notably higher than human reaction times [32] implying that there are additional factors other than human reaction time contributing to the detection process.

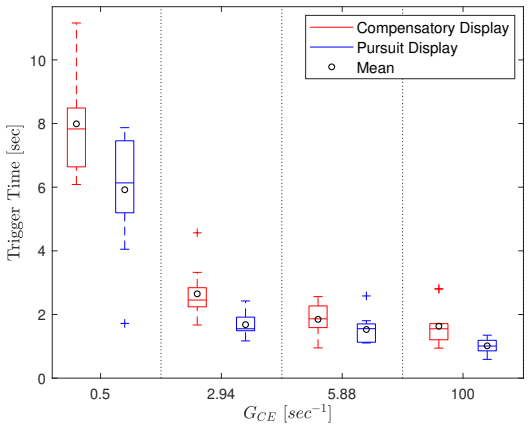

Fig. 20 Temporal scale of model's performance

These findings conclude that the combined model, based on $e(t)$ and $\dot{e}(t)$ can be effectively used for a range of rates of transition considered in this study. Moreover, this model is more suitable for the compensatory display.

V. Discussion

The objective of this research was to investigate how adaptive pilots utilize the compromised stability of the open-loop system to detect the change in controlled element dynamics. To achieve this goal, Monte Carlo simulations were conducted using the principles of the crossover model with added time delay. The simulation results yielded a high-accuracy model based on the error signal $e(t)$ and error-rate signal $\dot{e}(t)$, with threshold values of 3.3σ and 3.7σ, respectively.

To validate the simulation findings, a human-in-the-loop experiment was conducted, wherein the subjects performed a primary tracking task with a secondary task of pressing a button whenever they detected a change in CE dynamics. Twelve subjects participated in this experiment and tested both, compensatory and pursuit displays. Each display had twenty DYN1 runs and twenty DYN12 runs with five runs each for a different rate of change (G_{CE}). The results indicated that the error signal $e(t)$, similar to the simulations, exhibited high accuracy in predicting the HO's detection of change in CE dynamics. However, the model's performance using the error rate signal $\dot{e}(t)$ showed considerably lower accuracy compared to the simulations, with an average difference of 39% for the compensatory display, suggesting potential support-like use of this signal.

The experiment yielded good-quality data (subsection IV.A and subsection IV.B), with participants achieving an average accuracy of 92.08% for the compensatory display and 96.67% for the pursuit display. Regarding subjective detection lags, the mean values for the slowest ($G_{CE} = 0.5s^{-1}$) and fastest ($G_{CE} = 100s^{-1}$) rates of transition were 8.37s and 2.98s for the compensatory display, and 7.48s and 1.83s for the pursuit display, respectively. These values are consistent with those reported in Barragan's report [28] that used the pursuit display but lower than reported in [21][25] that used the compensatory display type. Moreover, the mean values of crossover frequency and phase margin in the DYN1 phase were very similar for the compensatory (2.73 rad/s and 64.19°) and pursuit display (2.81 rad/s and 60.61°) types. In a similar experiment conducted previously [26], the mean crossover frequency was reported to be 0.97 rad/s, a value not representative of skilled human operator behaviour [7]. Therefore, it is likely that the findings of the current study are more applicable to skilled human operator behaviour, which is the primary target audience for the applications of this model, which is in line with [28].

The first hypothesis, **H(1)**, predicted that $e(t)$ would have higher accuracy in predicting the HO's detection of change in CE dynamics for faster rates of transition i.e., for $G_{CE} = 5.88$ and $100s^{-1}$. The accuracy of the model using $e(t)$ presented in Table 9 shows that the error signal consistently had higher accuracy (compensatory display: 78.83% and 86.67%; pursuit display: 73.33% and 70.00%) than the error rate signal (compensatory display: 46.67% and 53.33%; pursuit display: 21.67% and 21.67%) for these G_{CE} values. Therefore, **H(1) is accepted**.

The second hypothesis, **H(2)**, predicted that $\dot{e}(t)$ would have higher accuracy for slower rates of CE transition ($G_{CE} = 0.5$ and $2.94s^{-1}$). This hypothesis, based on computer simulations, suggested that skilled HOs continuously adapt to gradual changes in CE dynamics, resulting in a less significant increase in tracking error. Consequently, it

would be the increase in the error rate signal that would help detect the change. However, the experimental findings contradict this hypothesis; $\dot{e}(t)$ did not contribute to high accuracy for slower transitions. The likely explanation is that the skilled HO uses some filtered version of $e(t)$ or the delay observed between control input and system output which is characteristic of double-integrator dynamics to detect the change in CE dynamics. Consequently, **H(2) is rejected**. Notably, this leads to a future interest in adjusting the trigger value (currently set at 3.7σ) of the error rate signal to validate the findings.

The next hypothesis, **H(3)** was based on simulation findings that the error signal had a higher mean accuracy across all DYN12 conditions, despite different G_{CE} values exhibiting varying preferences between $e(t)$ and $\dot{e}(t)$. Based on the experimental findings that support **H(1)** and reject **H(2)**, the fact that $e(t)$ consistently has higher accuracy for the entire range ($0.5s^{-1}$ to $100s^{-1}$) of DYN12 transitions makes it implicitly have higher average accuracy. Thus, **H(3) is accepted**. Moreover, this aligns with previous research indicating that a model with a threshold based on $e(t)$ performs well in detecting the DYN12 transition [10][20][21].

Moreover, **H(4)** predicted that the model, utilizing both error and error rate signals, would be more suitable for the compensatory display when compared with the pursuit display. This hypothesis was based on the premise that the HO has more information ($f_t(t)$ and $y(t)$) in the pursuit display and hence is not restricted to $e(t)$ and $\dot{e}(t)$. Table 9 supports this hypothesis and hence, **H(4) is accepted**. The inclusion of this hypothesis was crucial due to the availability of both error and error rate signals to the HO in a pursuit display and because prior studies have indicated that adaptive pilots often demonstrate compensatory tracking behaviour in pursuit tracking tasks [8].

Lastly, **H(5)**, predicted that the use of the pursuit display would lead to reduced detection lags when compared to the compensatory display. This hypothesis is supported by Figure 18 and was found to be statistically significant as well. Therefore, **H(5) is accepted**.

To improve the implementation of the model in real-life applications, a crucial next step would be to obtain the pilot model for the transitory part of the run i.e., in and around the centre of the CE's sigmoid. This can be achieved by implementing online identification models like recursive low-order ARX identification developed in [25] or algorithms like Box-Jenkins models [33] that can be used either offline or online so that the TV pilot model can be obtained. The obtained pilot model can then be utilized to adjust the pilot model parameters as a function of time similar to the computer simulations, thereby obtaining an accurate open-loop system. Subsequently, this process would facilitate a precise estimation of the region of interest. Implementing such a methodology will significantly contribute to further validating the model.

Moreover, a limitation of this model for the compensatory display lies in its inability to achieve high accuracy for gradual transitions, such as when the transition time is approximately 10s, despite the error being the only signal available to the human operator. This suggests the potential use of control input $u(t)$ which may become more prominent during slow transitions (as mentioned earlier, when the dynamics shift from DYN1 to DYN2, the delay between input and output becomes more noticeable) as the effect of control input is the only other signal available to the HO in compensatory displays. This limitation could also extend to the pursuit display, where the model's performance indicates the utilization of other strategies involving $u(t)$ and $y(t)$ by the HO. Therefore, it is recommended to incorporate $u(t)$ into the model to address this limitation effectively. The correct implementation will be evident when the model consistently achieves similar accuracy across all G_{CE} values. In essence, the model should demonstrate consistently high and very similar accuracy for DYN12 conditions, regardless of the rate of transition. An added approach is to conduct simulations and experiments for a range of G_{CE} with closely spaced transition times (like $1s, 2s$, 3s, etc) to obtain a range of time that marks the onset of decreased model accuracy and hence, increased dependency on $u(t)$. This can help further optimise the model by adding an increased weight to $u(t)$ as a function of decreasing rate of transition.

In addition to the current findings, further efforts should be directed towards investigating DYN21 transitions to assess whether the approach utilizing open-loop stability can be extended to dynamics that become more stable. This extension could involve redefining the ROI as a function of increased stability and adjusting threshold values such that a TP would be derived for no-trigger conditions, as demonstrated in [28].

Moreover, it is imperative to evaluate the model's applicability across a spectrum of different start and end CE dynamics to ascertain that the findings are not confined to the specific gain and pole values utilized in this study. This broader exploration would provide insights into generalising the proposed model. Furthermore, it is crucial to acknowledge that the threshold values employed in this study were derived from computer simulations and may not be optimized for experimental data. Therefore, optimizing these threshold values to better suit the experimental data can enhance the accuracy and reliability of the model's predictions when applied to real-world scenarios.

Lastly, it should be noted that there is a difference in subject and model detection times. The current difference ($\approx$ 1.5s in the compensatory display and $\approx$ 1s in the pursuit display) suggests that the model is triggered earlier than the

actual moment of HO's detection.

Overall, this study introduces a high-accuracy model that explains why and how the HO uses certain signals in a time duration preceding the detection of change in CE dynamics. The study thoroughly demonstrates the effect of display type and rate of transition on the human operator's detection process as well as on the model's accuracy. Thus, this study successfully models the pilot's detection of change in controlled element dynamics with proposed recommendations to increase the effectiveness of the model in order to develop more human-like automation.

VI. Conclusion

This study investigated the modelling of human operator's detection of change in controlled element dynamics using open-loop stability approach. It addressed a range of transition rates and considered two prominent display types used in aviation: compensatory and pursuit displays. The findings revealed that human operators predominantly rely on the error signal, demonstrating higher accuracy for both display types, during periods of compromised open-loop stability. This was in contrast to the simulation's findings that suggested the use of both, the error and error rate signals. Threshold values for these signals were established at 3.3σ and 3.7σ respectively. The pursuit display helped the human operator to have better performance and lower detection lags. The combined model utilizing both signals exhibited superior accuracy for the compensatory display (88.54%) compared to the pursuit display (80.62%). Overall, the study underscores the adaptive nature of human pilots, who effectively utilize the decrease in open-loop stability to detect changes in controlled element dynamics.

References

[1] "Loss of Control In-flight (LOC-I)," https://www.iata.org/en/programs/safety/operational-safety/loss-of-control-inflight/, 2023. Accessed: 2023-10-11.

[2] McRuer, D. T., and Jex, H. R., "A review of quasi-linear pilot models," *IEEE transactions on human factors in electronics*, Vol. HFE-8, No. 3, 1967, pp. 231–249. URL https://doi.org/10.1109/THFE.1967.234304.

[3] Zaal, P., and Sweet, B., "Estimation of time-varying pilot model parameters," *AIAA Modeling and Simulation Technologies Conference*, 2011, p. 6474. URL https://doi.org/10.2514/6.2011-6474.

[4] Mulder, M., Pool, D. M., Abbink, D. A., Boer, E. R., Zaal, P. M., Drop, F. M., van der El, K., and van Paassen, M. M., "Manual control cybernetics: State-of-the-art and current trends," *IEEE Transactions on Human-Machine Systems*, Vol. 48, No. 5, 2017, pp. 468–485. URL https://doi.org/10.1109/THMS.2017.2761342.

[5] Young, L. R., Green, D. M., Elkind, J. I., and Kelly, J. A., "Adaptive dynamic response characteristics of the human operator in simple manual control," *IEEE Transactions on Human Factors in Electronics*, Vol. HFE-5, No. 1, 1964, pp. 6–13. URL https://doi.org/10.1109/THFE.1964.231648.

[6] Sadoff, M., *A Study of a Pilots Ability to Control During Simulated Stability Augmentation System Failures*, National Aeronautics and Space Administration, 1962. https://doi.org/19630000307.

[7] McRuer, D. T., "Human-pilot dynamics in compensatory systems," *AFFDL-TR-65-15*, 1965. URL https://doi.org/10.1109/THFE.1965.6591261.

[8] Wasicko, R. J., McRuer, D. T., and Magdaleno, R. E., *Human pilot dynamic response in single-loop systems with compensatory and pursuit displays*, Vol. 66, Air Force Flight Dynamics Laboratory, Research and Technology Division, Air Force Systems Command, 1966. URL https://doi.org/10.21236/ad0646652.

[9] Stapleford, R. L., McRuer, D. T., and Magdaleno, R. E., "Pilot describing function measurements in a multiloop task," *IEEE Transactions on Human Factors in Electronics*, Vol. HFE-8, No. 2, 1967, pp. 113–125. URL https://doi.org/10.1109/THFE.1967.233628.

[10] Phatak, A. V., and Bekey, G. A., "Model of the adaptive behavior of the human operator in response to a sudden change in the control situation," *IEEE Transactions on Man-Machine Systems*, Vol. 10, No. 3, 1969, pp. 72–80. URL https://doi.org/10.1109/TMMS.1969.299886.

[11] Levison, W. H., Baron, S., and Kleinman, D. L., "A model for human controller remnant," *IEEE Transactions on man-machine systems*, Vol. 10, No. 4, 1969, pp. 101–108. URL https://doi.org/10.1109/TMMS.1969.299906.

[12] Hess, R. A., "Modeling the pilot detection of time-varying aircraft dynamics," *Journal of aircraft*, Vol. 49, No. 6, 2012, pp. 2100–2104. URL https://doi.org/10.2514/1.C031805.

[13] Hess, R. A., "A model for pilot control behavior in analyzing potential loss-of-control events," *Proceedings of the Institution of Mechanical Engineers, Part G: Journal of Aerospace Engineering*, Vol. 228, No. 10, 2014, pp. 1845–1856. URL https://doi.org/10.2514/6.2011-6474.

[14] van der El, K., Pool, D. M., Damveld, H. J., van Paassen, M. M., and Mulder, M., "An empirical human controller model for preview tracking tasks," *IEEE transactions on cybernetics*, Vol. 46, No. 11, 2015, pp. 2609–2621. URL https://doi.org/10.1109/tcyb.2015.2482984.

[15] Drop, F. M., *Control-Theoretic Models of Feedforward in Manual Control*, Vol. 46, Logos Verlag Berlin GmbH, 2016. URL https://api.semanticscholar.org/CorpusID:114491896.

[16] Jakimovska, N., Pool, D. M., van Paassen, M. M., and Mulder, M., "Using the Hess Adaptive Pilot Model for Modeling Human Operator's Control Adaptations in Pursuit Tracking," *AIAA SCITECH 2023 Forum*, 2023, p. 0541. URL https://doi.org/10.2514/6.2023-0541.

[17] Xu, S., Tan, W., Wang, W., and Sun, L., "Pilot time-varying control behavior modeling in refractory period with aircraft failures," *Science China Technological Sciences*, 2023, pp. 1–13. URL https://doi.org/10.1007/s11431-022-2099-6.

[18] Hess, R. A., "Modeling pilot control behavior with sudden changes in vehicle dynamics," *Journal of Aircraft*, Vol. 46, No. 5, 2009, pp. 1584–1592. URL https://doi.org/10.2514/1.41215.

[19] Hess, R., "A preliminary study of human pilot dynamics in the control of time-varying systems," *AIAA modeling and simulation technologies conference*, 2011, p. 6554. URL https://doi.org/10.2514/6.2011-6554.

[20] Elkind, J. I., and Miller, D. C., "Process of adaptation by the human controller," Tech. rep., NASA, 1966.

[21] van Ham, J., "Predicting Adaptive Human Control Behavior to Changing Controlled Element Dynamics Based on Statistical Variations in Error and Error Rate," *IFAC-PapersOnLine*, 2021. URL https://doi.org/10.1016/j.ifacol.2022.10.250.

[22] Weir, D. H., and Johnston, W., "Pilot's Response to Stability Augmentation System Failures and Implications for Design," *Proceedings of the Fourth Annual NASA-University Conference on Manual Control*, 1969, pp. 341–360. URL https://doi.org/10.2514/3.44096.

[23] Zaal, P., and Pool, D. M., "Multimodal pilot behavior in multi-axis tracking tasks with time-varying motion cueing gains," *AIAA Modeling and Simulation Technologies Conference*, 2014, p. 0810. URL https://doi.org/10.2514/6.2014-0810.

[24] van Grootheest, A., Pool, D. M., van Paassen, M., and Mulder, M., "Identification of Time-Varying Manual Control Adaptations with Recursive ARX Models," *2018 AIAA Modeling and Simulation Technologies Conference*, 2018, p. 0118. URL https://doi.org/10.2514/6.2018-0118.

[25] Plaetinck, W., Pool, D., Van Paassen, M., and Mulder, M., "Online identification of pilot adaptation to sudden degradations in vehicle stability," *IFAC-PapersOnLine*, Vol. 51, No. 34, 2019, pp. 347–352. URL https://doi.org/10.1016/j.ifacol.2019.01.020.

[26] Terenzi, L., Zaal, P., Pool, D. M., and Mulder, M., "Adaptive manual control: A predictive coding approach," *AIAA SCITECH 2022 Forum*, 2022, p. 2448. URL https://doi.org/10.2514/6.2022-2448.

[27] Zaal, P. M., "Manual control adaptation to changing vehicle dynamics in roll-pitch control tasks," *Journal of guidance, control, and dynamics*, Vol. 39, No. 5, 2016, pp. 1046–1058. URL https://doi.org/10.2514/1.G001592.

[28] Barragan, M., Pool, D. M., Mulder, M., and van Paassen, M. M., "Modeling the Human Operator's Detection of a Change in Controlled Element Dynamics," , 2023. Unpublished.

[29] Pool, D. M., Pais, A. V., De Vroome, A. M., van Paassen, M. M., and Mulder, M., "Identification of nonlinear motion perception dynamics using time-domain pilot modeling," *Journal of guidance, control, and dynamics*, Vol. 35, No. 3, 2012, pp. 749–763. URL https://doi.org/10.2514/1.56236.

[30] Allen, R. W., and Jex, H. R., "An experimental investigation of compensatory and pursuit tracking displays with rate and acceleration control dynamics and a disturbance input," Tech. rep., NASA, 1968.

[31] Gignac, G. E., and Szodorai, E. T., "Effect size guidelines for individual differences researchers," *Personality and Individual Differences*, Vol. 102, 2016, p. 74–78. https://doi.org/10.1016/j.paid.2016.06.069.

[32] Thorpe, S., Fize, D., and Marlot, C., "Speed of processing in the human visual system," *nature*, Vol. 381, No. 6582, 1996, pp. 520–522. URL https://doi.org/10.1038/381520a0.

[33] Moya, A., Pool, D. M., Mulder, M., and van Paassen, M. M., "Time-Varying Human-Operator Identification with Box-Jenkins Models," , 2023. Unpublished.

Part III

Appendices

A

State-Space Modelling

The modelling and representation of systems are generally done using either of the two methods: transfer functions tf and state-space ss representation. While the former is unique to a system, the latter is not unique, i.e. a system can have two different state-space representations. While a transfer function is a mathematical representation that relates the system's output to its input, a state-space representation is a mathematical model used to describe the behaviour of a dynamic system over time. Generally, a system can be represented in either format based on the requirements. For the research carried out in this study, it is a common practice to have a tf representation of the CE and the pilot model given that they are SISO systems and are simpler systems not requiring explicit representation of their state variables. Moreover, the behaviour and reasoning of all the parameters present in the CE and pilot model are easier to interpret using transfer functions. As a result, the formal definitions of these systems throughout the study are done using transfer functions. These transfer functions are shown below in Equation A.1 and Equation A.2 for CE and pilot model respectively. As seen in Equation A.1, two equivalent forms of representation are available for CE dynamics.

$$H_{CE}(s,t) = \frac{K_c(t)}{s(s+\omega_b(t))} \Leftrightarrow \frac{K_c(t)\tau_c(t)}{s(\tau_c(t)s+1)} \tag{A.1}$$

$$H_p(s,t) = K_p(t)(\tau_L(t)s+1)e^{-s\tau_e(t)}\frac{\omega_{nm}^2}{s^2+2\zeta_{nm}\omega_{nm}s+\omega_{nm}^2} \tag{A.2}$$

Here $\tau_c(t)$ is the CE time constant ($\tau_c = \frac{1}{\omega_b}$). In initial simulations, the latter structure was used for CE dynamics, i.e. using the time constant. While this was reasonable, it was found that the product of two sigmoids did not result in a required sigmoid. This anomaly occurred in the second structure's numerator where $K_c(t)$ and $\tau_c(t)$ are multiplied. Figure A.1 shows the sigmoidal behaviour of the parameters of the selected CE structure from DYN1 to DYN2 for the entire duration of the simulation with $G = 0.5[sec^{-1}]$ and the resultant non-sigmoidal behaviour obtained from the multiplication of the two parameters to achieve the numerator of the second structure.

Subsequently, the pilot will then adapt to the TV CE dynamics by varying required parameters, namely, $K_p(t), \tau_L(t)$ and $\tau_e(t)$. These parameters in the theoretical case of an ideal pilot without delay, should exhibit the same behaviour as that of individual sigmoidal transition as seen in for CE parameters in Figure A.1. Similar to the case of CE, given the structure of the pilot model, it can be seen that these parameters are not independent in transition, but rather in combination, therefore, the multiplication of $K_p(t)$ and $\tau_L(t)$, will exhibit the same divergence from sigmoidal behaviour like the numerator of the second CE structure. This is shown in Figure A.2. It is to be noted that, in the figure, $Kedot$ is the required form of transition. It is observed that even though the sigmoids seem to overlap, the non-sigmoidal behaviour can be seen in the zoomed-in version of the same plot focusing on the behaviour around the centre of the sigmoid M.

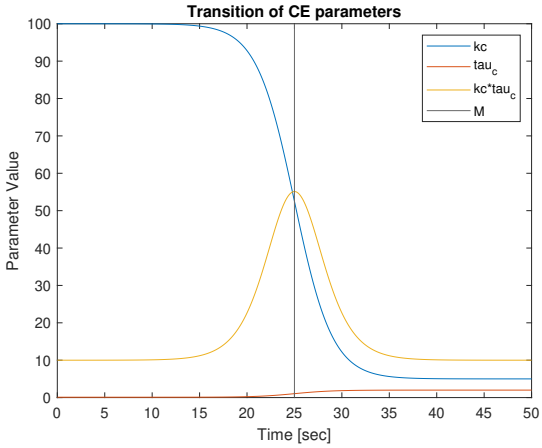

Figure A.1: Non-sigmoidal behaviour of the TV CE tf

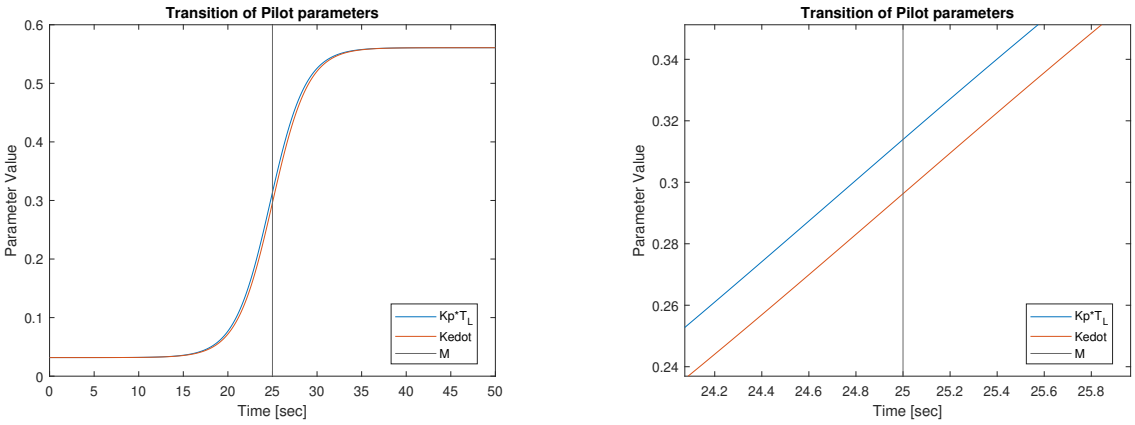

(a) Problem of using tf for the pilot

(b) Maximized view

Figure A.2: Non-sigmoidal behaviour of the TV pilot tf

Figure A.3 shows the normality-normality plot of $Kedot$ to represent how divergent the noon-sigmoidal behaviour is from a sigmoidal behaviour, which is the diagonal reference line. The non-sigmoidal behaviour of the pilot transfer function parameters will continue to diverge when the effective time delay term is added. Given the problems caused by using tf, it was concluded that this form leads to the violation of the crossover model for time-varying simulations that are fundamental to manual tracking tasks.

As a result, an alternative approach, which proved to be successful and was henceforth used in the simulations conducted in this study, was the use of ss representation of the CE and pilot systems. The symbolic ss obtained for CE and pilot are mentioned in Equation A.3 and Equation A.4 respectively. Lastly, it is essential to note that the transfer function representation of the CE that uses ω_b will not show non-sigmoidal behaviour as the two parameters, namely, K_c and ω_b do not form a combined unit during calculations; the eventual use of ss for the CE is done to have all systems represented using the same format. The proof that both CE parameters act individually can also be seen in its ss representation. Eq.(A.3) and Eq.(A.4) give the ss representation of the CE and pilot respectively.

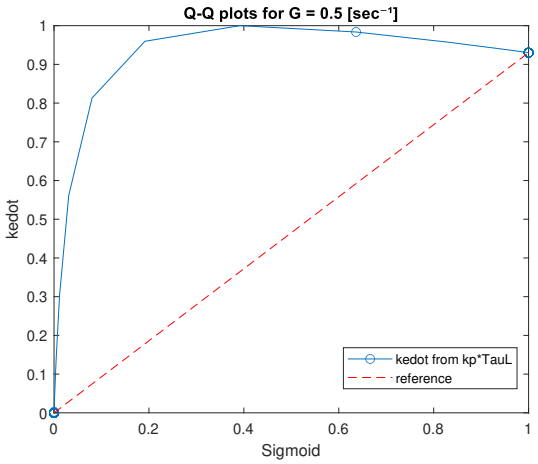

Figure A.3: Normality-normality plot of $Kedot$

$$
\begin{aligned}
A_{CE} &= \begin{bmatrix} -\omega_b & 0 \\ 1 & 0 \end{bmatrix} \\
B_{CE} &= \begin{bmatrix} 1 \\ 0 \end{bmatrix} \\
C_{CE} &= \begin{bmatrix} 1 & K_c \end{bmatrix} \\
D_{CE} &= 0
\end{aligned}
\tag{A.3}
$$

$$
A_{CE} = \begin{bmatrix} \frac{-(D_2+2\cdot D_1\cdot\omega_{nm}\cdot\zeta_{nm})}{D_1} & \frac{-(D_1\cdot\omega_{nm}^2+2\cdot D_2\cdot\zeta_{nm}\cdot\omega_{nm}+D_3)}{D_1} & \frac{-(D_2\cdot\omega_{nm}^2+2\cdot D_3\cdot\omega_{nm}\cdot\zeta_{nm})}{D_1} & \frac{-(D_3\cdot\omega_{nm}^2)}{D_1} \\ 1 & 0 & 0 & 0 \\ 0 & 1 & 0 & 0 \\ 0 & 0 & 1 & 0 \end{bmatrix}
$$

$$
B_{CE} = \begin{bmatrix} 1 \\ 0 \\ 0 \\ 0 \end{bmatrix}
$$

$$
C_{CE} = \begin{bmatrix} \frac{(N_1\cdot\dot{K_e}\cdot\omega_{nm}^2)}{D_1} & \frac{(N_2\cdot\dot{K_e}\cdot\omega_{nm}^2+N_1\cdot K_p\cdot\omega_{nm}^2)}{D_1} & \frac{(N_3\cdot\dot{K_e}\cdot\omega_{nm}^2+N_2\cdot K_p\cdot\omega_{nm}^2)}{D_1} & \frac{(N_3\cdot K_p\cdot\omega_{nm}^2)}{D_1} \end{bmatrix}
$$

$$
D_{CE} = 0
\tag{A.4}
$$

Where N_x $(x = 1, 2, 3)$ represents the numerator terms and D_x the denominator terms of the 2^{nd} order pade approximation of the exponential time delay $e^{-s\tau_e}$ term of the pilot model. This is done to be able to represent the ss of the pilot using Matlab's `Symbolic Math Toolbox` along with the `tf2ss` function

that cannot take exponential terms in its argument. Eq(A.5) shows the structure of the 2^{nd} order pade approximation. Here, s^2 is included in N_1 and D_1; s in N_2 and D_2 and N_3 and D_3 are constants.

$$pade(e^{-s\tau_e}) = \frac{N_1 + N_2 + N_3}{D_1 + D_2 + D_3} \tag{A.5}$$

It is vital to note that all the elements of the different ss matrices are then transitioned as a sigmoid to achieve the required time-varying nature of the simulations. Hence, the ss representation of systems under consideration solves the identified pitfalls of the tf representation for the paper's primary aim of time-varying manual control task simulations.

B

Simulink Modelling

This section shows the final simulink model used for t-domain simulations.

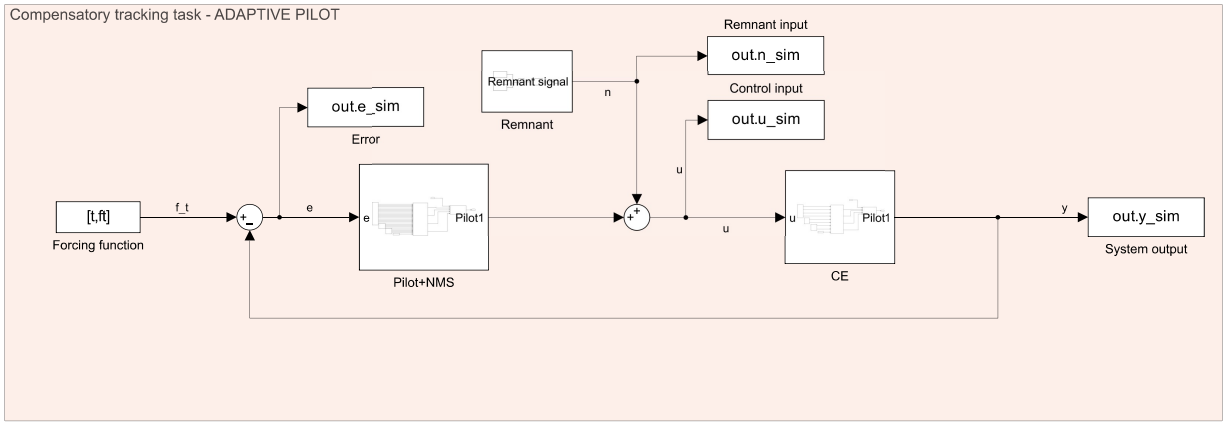

Figure B.1: Simulink model of the compensatory tracking task

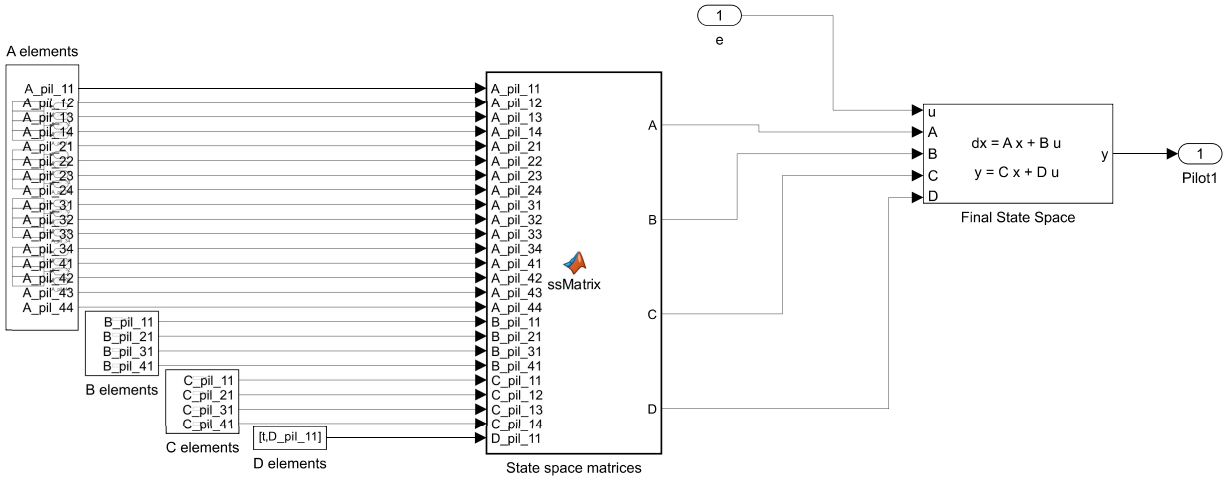

Figure B.2: Simulink model - pilot

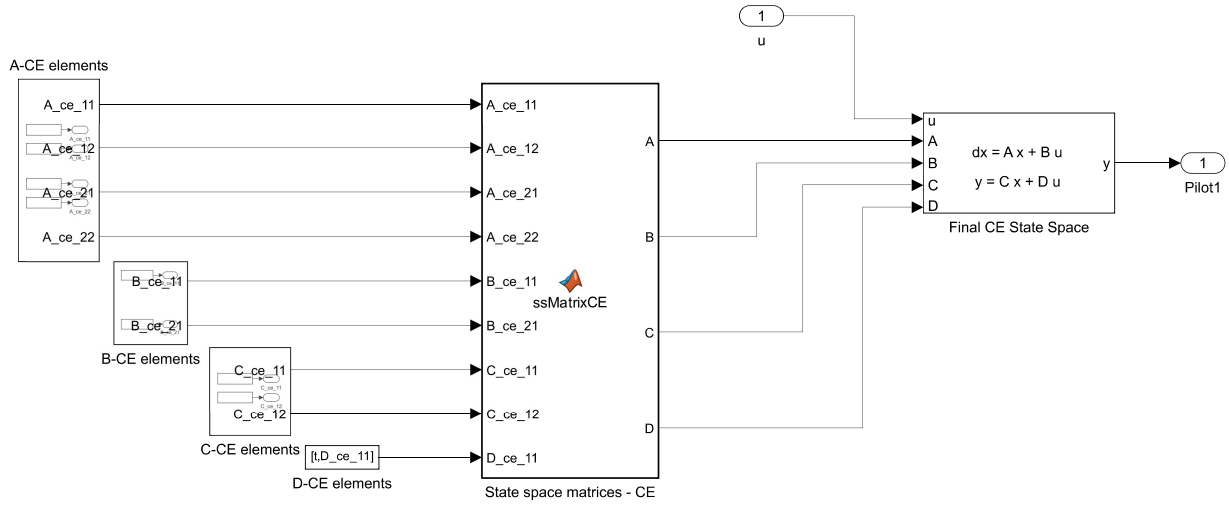

Figure B.3: Simulink model - CE

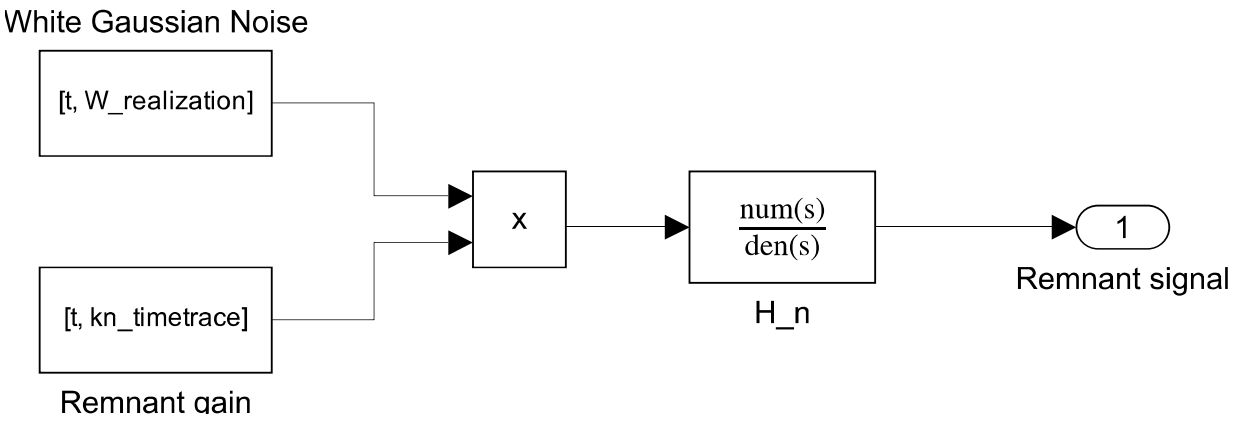

Figure B.4: Simulink model - Remnant

Here, the state-space matrix function block in Figure B.2 and Figure B.3 are Matlab function blocks which restructure the inputs into matrices required for the ss.

C

Calculating the Remnant Gain

This appendix outlines the derivation of the relation utilized in the computer simulations to account for the non-linear part of the human operator, specifically the remnant filter. The objective is to determine the remnant gain K_n needed to achieve the desired power of the noise signal in the control input, based on the power ratio P_n.

To establish the relation for the time-varying remnant gain, it is essential to define the covariance function (C) of two zero-mean stochastic variables: $\bar{x}(t)$ and $\bar{y}(t)$.

$$C_{\bar{x}\bar{y}}(\tau) = E\{\bar{x}(t)\bar{y}(t+\tau)\} = \lim_{T\to\infty}\left(\frac{1}{2T}\int_{-T}^{T}\bar{x}(t)\bar{y}(t+\tau)dt\right) \tag{C.1}$$

With this covariance function defined, the next step involves obtaining the power spectral density (PSD) function by taking the Fourier transform ($\mathcal{F}$):

$$S_{\bar{x}\bar{y}}(\omega) = \mathcal{F}\left\{C_{\bar{x}\bar{y}}(\tau)\right\} = \int_{-\infty}^{\infty} C_{\bar{x}\bar{y}}(\tau)e^{-j\omega\tau}d\tau \tag{C.2}$$

Here, since two different stochastic processes are considered, the PSD is a cross-PSD ($S_{\bar{x}\bar{y}}(\omega)$). If it were taken for the same stochastic process, it would be the auto-PSD ($S_{\bar{x}\bar{x}}(\omega)$). The definitions of these PSDs are given below:

$$S_{\bar{x}\bar{y}}(\omega) = \lim_{T\to\infty}\left(\frac{1}{2T}\bar{Y}(\omega)\bar{X}(-\omega)\right), \quad S_{\bar{x}\bar{x}}(\omega) = \lim_{T\to\infty}\left(\frac{1}{2T}\bar{X}(\omega)\bar{X}(-\omega)\right) = \lim_{T\to\infty}\left(\frac{1}{2T}|\bar{X}(\omega)|^2\right) \tag{C.3}$$

Furthermore, the variance ($\sigma^2_{\bar{x}\bar{x}}$) of a stochastic variable can be calculated by integrating the auto-PSD function:

$$\sigma^2_{\bar{x}\bar{x}} = C_{\bar{x}\bar{x}}(\tau = 0) = \frac{1}{2\pi}\int_{-\infty}^{\infty} S_{\bar{x}\bar{x}}(\omega)d\omega \tag{C.4}$$

Now, using Figure 3.5 as reference, it is observed that $\bar{u}(t) = \bar{u_e}(t) + \bar{n}(t)$, where $\bar{u_e}(t)$ is the output signal from $H_P(s)$. Thus, taking the Fourier transform of these signals gives:

$$\bar{U}(\omega) = \bar{U_e}(\omega) + \bar{N}(\omega) \tag{C.5}$$

However, as the forcing function and the noise signal are assumed to be uncorrelated, $S_{\bar{f}_t\bar{n}} = S_{\bar{n}\bar{f}_t} = 0$. The auto-PSD of $\bar{u}(t)$ in Equation C.5 can be obtained as follows:

$$\bar{U}(\omega)\bar{U}(-\omega) = \big(\bar{U}_e(\omega) + \bar{N}(\omega)\big) \cdot \big(\bar{U}_e(-\omega) + \bar{N}(-\omega)\big)$$
$$\therefore \bar{U}(\omega)\bar{U}(-\omega) = \left(\frac{H_P(\omega)}{1 + H_P(\omega)H_{CE}(\omega)}\bar{F}(\omega) + \frac{H_n(\omega)}{1 + H_P(\omega)H_{CE}(\omega)}\bar{N}(\omega)\right) \cdot \left(\frac{H_P(-\omega)}{1 + H_P(-\omega)H_{CE}(-\omega)}\bar{F}(-\omega) + \frac{H_n(-\omega)}{1 + H_P(-\omega)H_{CE}(-\omega)}\bar{N}(-\omega)\right)$$

Taking the expectation, E$\{\cdot\}$:

$$S_{\bar{u}\bar{u}}(\omega) = \left|\frac{H_P(\omega)}{1 + H_P(\omega)H_{CE}(\omega)}\right|^2 S_{\bar{f}_t\bar{f}_t}(\omega) + \left|\frac{H_n(\omega)}{1 + H_P(\omega)H_{CE}(\omega)}\right|^2 S_{\bar{n}\bar{n}}(\omega)$$
$$\rightarrow S_{\bar{u}\bar{u}}(\omega) = S_{\bar{u}_{f_t}\bar{u}_{f_t}}(\omega) + S_{\bar{u}_n\bar{u}_n}(\omega)$$

Where, $H_n(\omega) = K_n^2 \cdot \frac{1}{(\tau_n j\omega+1)^2} = K_n^2 \cdot H_n'(\omega)$

Given the relation defined in Equation C.4 and the definition of P_n given by Equation C.6, substituting the relevant terms obtained above yields the following relation:

$$P_n = \frac{\sigma^2_{\bar{u_n}\bar{u_n}}}{\sigma^2_{\bar{u}\bar{u}}} = \frac{\sigma^2_{\bar{u_n}\bar{u_n}}}{\sigma^2_{\bar{u_n}\bar{u_n}} + \sigma^2_{\bar{u}_{f_t}\bar{u}_{f_t}}} \tag{C.6}$$

$$\therefore P_n = \frac{\frac{1}{2\pi} \cdot \int_{-\infty}^{\infty} |\frac{H_n(\omega)}{1+H_P(\omega)H_{CE}(\omega)}|^2 \cdot S_{\bar{n}\bar{n}}dt}{\frac{1}{2\pi} \cdot \int_{-\infty}^{\infty} |\frac{H_n(\omega)}{1+H_P(\omega)H_{CE}(\omega)}|^2 \cdot S_{\bar{n}\bar{n}}dt + \frac{1}{2\pi} \cdot \int_{-\infty}^{\infty} |\frac{H_P(\omega)}{1+H_P(\omega)H_{CE}(\omega)}|^2 \cdot S_{\bar{f}_t\bar{f}_t}dt} \tag{C.7}$$

Now let,

$$a = \frac{1}{2\pi} \cdot \int_{-\infty}^{\infty} |\frac{H_n'(\omega)}{1 + H_P(\omega)H_{CE}(\omega)}|^2 \cdot S_{\bar{n}\bar{n}}dt$$
$$b = \frac{1}{2\pi} \cdot \int_{-\infty}^{\infty} |\frac{H_P(\omega)}{1 + H_P(\omega)H_{CE}(\omega)}|^2 \cdot S_{\bar{f}_t\bar{f}_t}dt$$
$$\therefore P_n = \frac{K_n^2 a}{K_n^2 a + b} \; (\because H_n(\omega) = K_n^2 \cdot H_n'(\omega))$$
$$\rightarrow K_n = \sqrt{\frac{P_n}{1 - P_n} \times \frac{b}{a}}$$

And, rearranging b as:

$$b = \frac{1}{2\pi} \cdot \int_{-\infty}^{\infty} |\frac{H_P(\omega)}{1 + H_P(\omega)H_{CE}(\omega)}|^2 \cdot S_{\bar{f}_t\bar{f}_t}dt$$
$$\therefore b = \frac{1}{\pi} \cdot \int_{0}^{\infty} |\frac{H_P(\omega)}{1 + H_P(\omega)H_{CE}(\omega)}|^2 \cdot S_{\bar{f}_t\bar{f}_t}dt$$
$$\rightarrow b = \pi\sigma^2_{\bar{uf}_t}$$

Lastly, substituting the value of $S_{\bar{n}\bar{n}}$ = Intensity of white noise (W) = 1 by design. We obtain the following relation:

$$K_n = \sqrt{\frac{P_n}{1 - P_n} \times \frac{\pi\sigma^2_{uf_t}}{\int_0^{\infty} |\frac{1}{(\tau_n j\omega+1)^2}|^2 |\frac{1}{(1+H_p(j\omega)H_{CE}(j\omega))}|^2 W d\omega}} \tag{C.8}$$

Thus, the above relation can now be used to calculate the remnant gain for a given set of dynamics and pre-defined power ratio.

D

Validating f_t Realizations

Implementing the forcing function realizations used in the experiment needs to be validated to ensure that the f_t does not undergo any unforeseen change because, the process of implementation in DUECA (middleware), utilizes the forcing function parameters and not the time-signal as is. Thus, first, the simulated f_t realizations are implemented on the hardware. Second, the realizations are run for their entire period T_m and a log file is obtained that gives time-signal data at each time step. This data is now tested against the simulated f_t.

The verification of the f_t implemented in the experiment in comparison to the simulated ones is given in Figure D.1, which shows a round-off error pattern for one complete period of all six realizations obtained by subtracting the experimental realizations from their simulated counterpart. The magnitude of error was found to be of the order of $10^{-7\circ}$. This error results from the rounding-off of the decimal place integers which changes based on the hardware used.

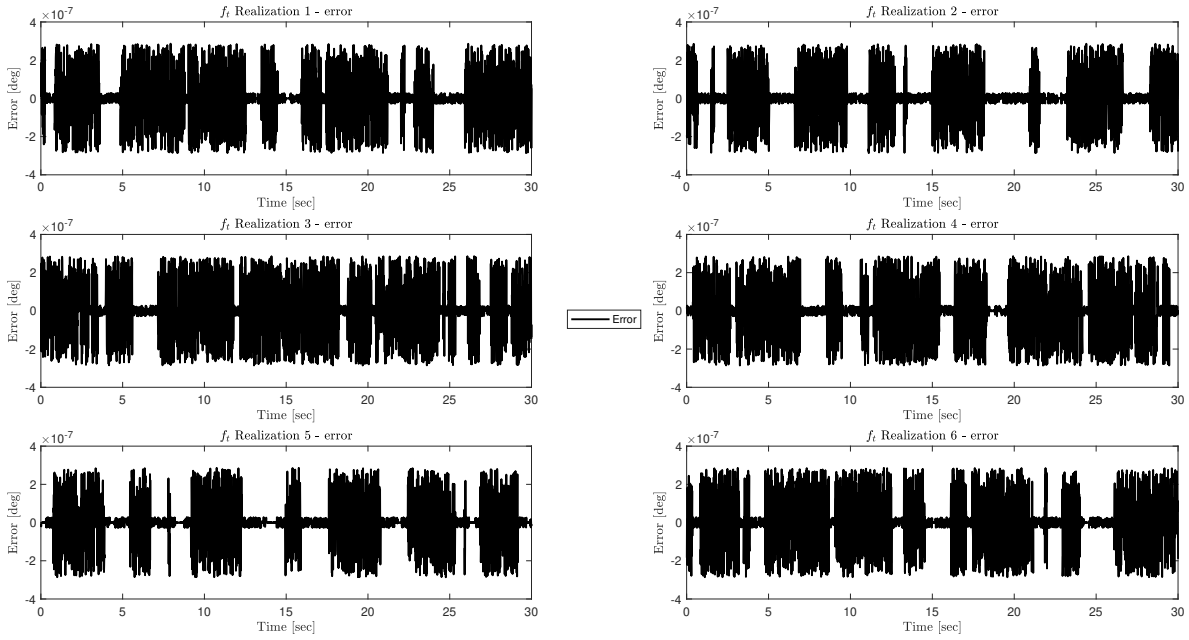

Figure D.1: Comparison of theoretical (designed) and experimentally implemented forcing function (f_t) realizations

Moreover, Figure D.2 shows a comparison of theoretical and experimental power spectral density (PSD) of the f_t, which shows that both the forcing functions have power at the desired frequencies; peaks occurring at integer multiples of the fundamental frequency $k\omega_m$. Here, the difference observed for

extremely low powers (depth of Y-axis) is a result of the difference in the number of decimal place integers considered.

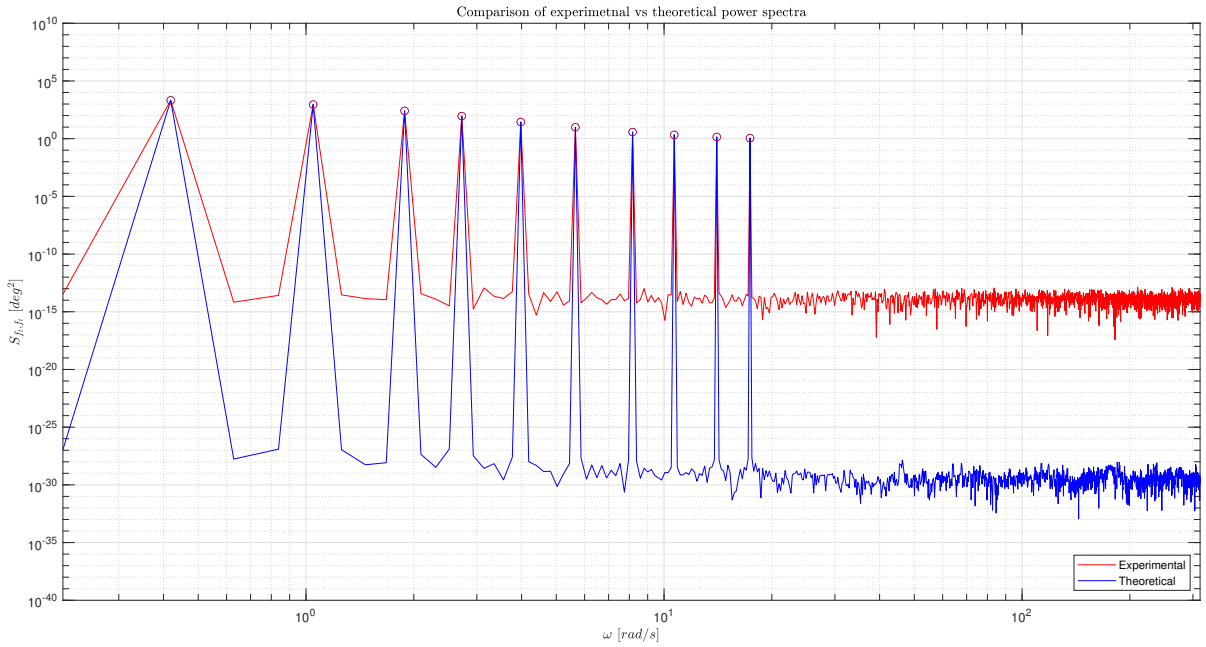

Figure D.2: Comparison of theoretical and experimental Power Spectral Density of the forcing function (f_t)

E

Pilot Model Parameters

The pilot model parameters are derived using Maximum Likelihood Estimation (MLE) from the time signal data collected during the 30-second pre-transition period corresponding to the DYN1 part of all runs.

The MLE algorithm operates by employing common estimates (provided by the user) as initial guesses for the pilot parameters, to find the optimal match between the simulated control input signal (obtained from $e(t)$ as input to the initial guess-based pilot model) and the experimental record of the control input signal. The algorithm is iterated 100 times per run. Here, during any of these iterations, the algorithm stops further iterations if the best fit surpasses a predefined minimum threshold (10^{-6}) for the difference between the current and previous step's fits. The corresponding percentage variance accounted for (%VAF) is also noted to check for the quality of the fit obtained.

Even though all runs were iterated over with 2 sets of initial guesses, the figures shown below give the spread of mean parameter value per run per participant. Thus, each boxplot contains 40 data points. Moreover, it is noted that all parameters obtained from the MLE are presented here, namely, pilot gain K_p, lead time τ_L, effective time delay τ_e, natural frequency of the neuromuscular system ω_{nms}, damping ratio of the neuromuscular system ζ_{nms} and the variance accounted for %VAF.

The corresponding global mean values (red horizontal line) of these parameters are found to be $K_p = 2.96$, $\tau_L = 0.20s$, $\tau_e = 0.24s$, $\omega_{nms} = 12.37rad/s$, $\zeta_{nms} = 0.36$ and %$VAF = 75.85$% for the compensatory display and $K_p 3.31$, $\tau_L = 0.15s$, $\tau_e = 0.23s$, $\omega_{nms} = 12.24rad/s$, $\zeta_{nms} = 0.28$ and %$VAF = 80.93$% for the pursuit display.

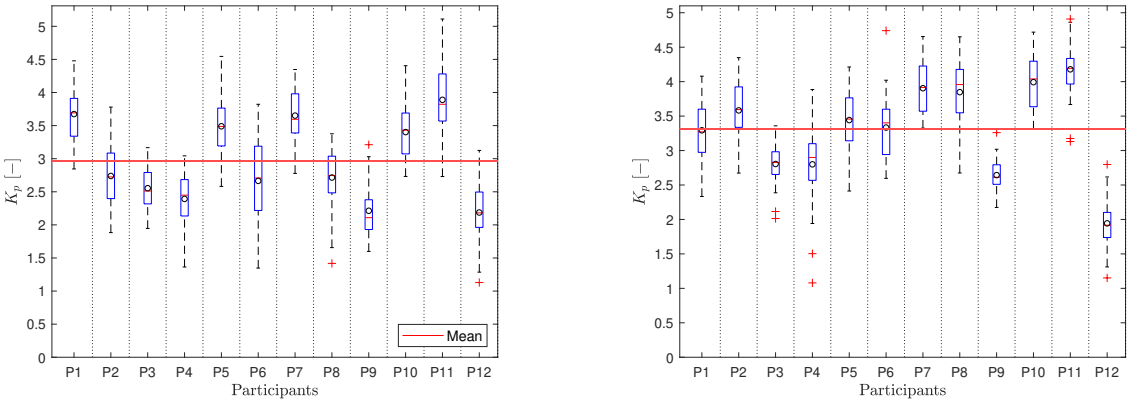

(a) K_p in compensatory display

(b) K_p in pursuit display

Figure E.1: Pilot Gain (K_p)

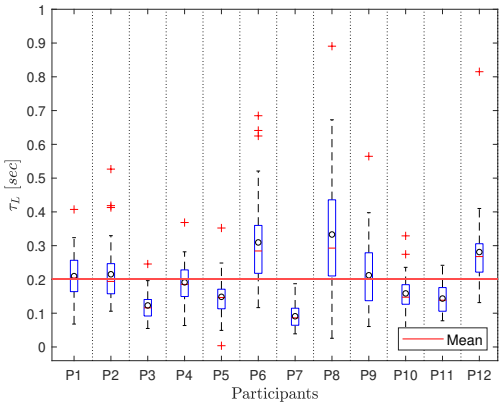

(a) τ_L in compensatory display

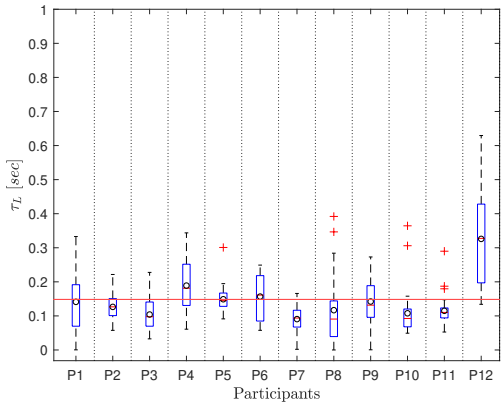

(b) τ_L in pursuit display

Figure E.2: Lead Time (τ_L)

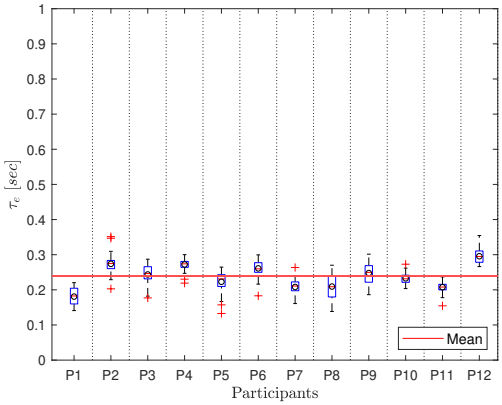

(a) τ_e in compensatory display

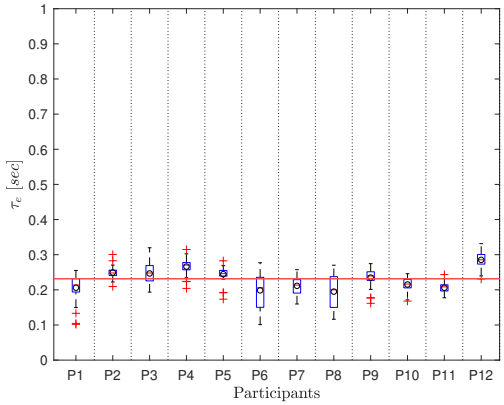

(b) τ_e in pursuit display

Figure E.3: Effective Time Delay (τ_e)

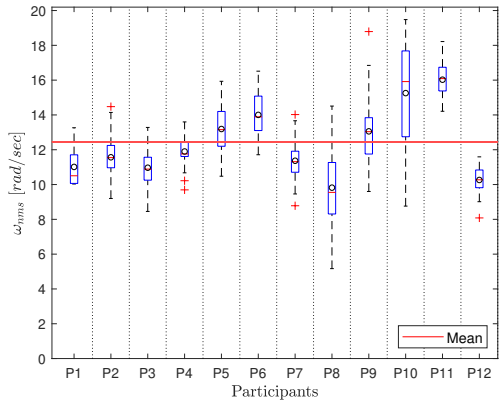

(a) ω_{nms} in compensatory display

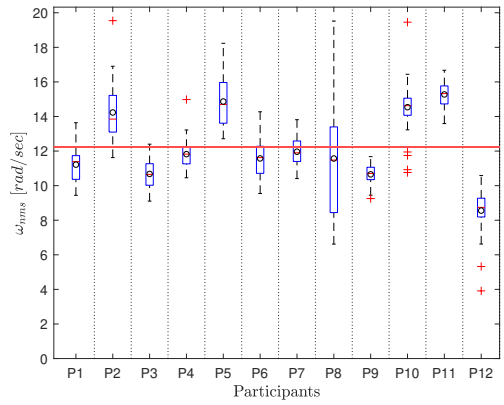

(b) ω_{nms} in pursuit display

Figure E.4: Natural Frequency of the Neuromuscular System (ω_{nms})

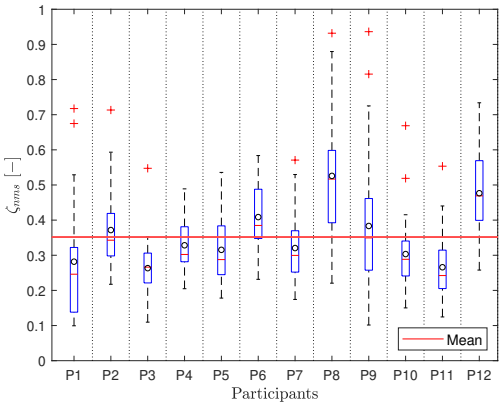

(a) ζ_{nms} in compensatory display

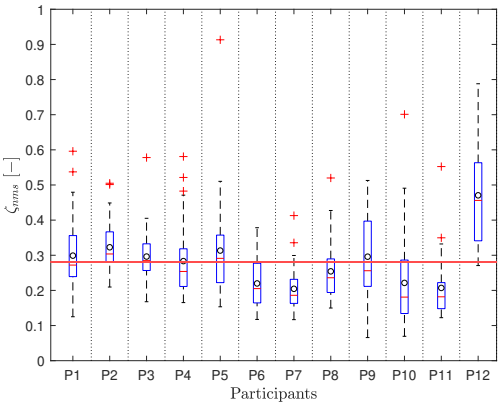

(b) ζ_{nms} in pursuit display

Figure E.5: Damping Ratio of the Neuromuscular System (ζ_{nms})

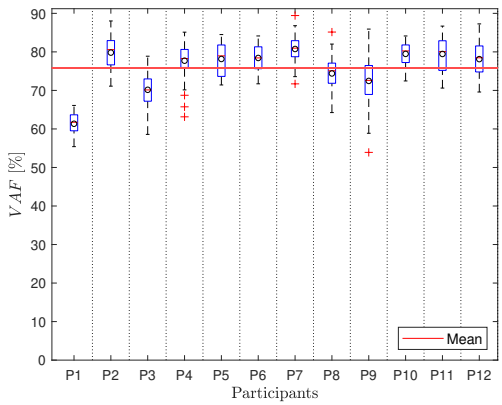

(a) %VAF in compensatory display

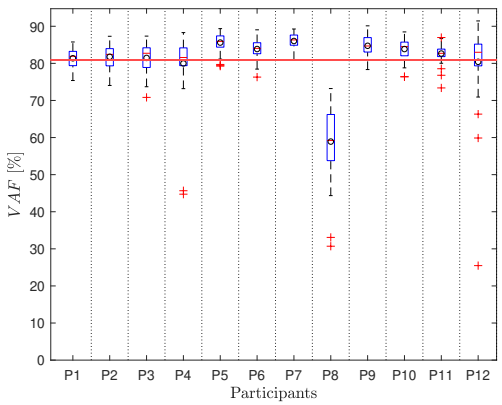

(b) %VAF in pursuit display

Figure E.6: Variance Accounted For (%VAF)

F

Categorical Data of Accuracy

This appendix provides the categorical data of both, the subject's and the combined model's root cause of accuracy. That is the quantification of the TP, TN, FP and FN. The first two figures, Figure F.1 and Figure F.2, give the subject and combined model's categorical data respectively, for the DYN1 condition, which covers half of the total runs per display type. This is followed by the data for the DYN12 condition in Figure F.3 and Figure F.4 where each row in the subplots corresponds to a G_{CE} value.

It can be seen from these figures that each G_{CE} has five runs related to the five f_t realizations, which make a total of 20 DYN12 runs. Notably, the values in each segment of the stacked bar graphs correspond to the quantity in that segment (category).

Furthermore, for the figures that correspond to the combined model's accuracy, the legend entry "FN/P" implies that the error signal-based model and error rate signal-baed model categorized a run in two different false categories i.e., if $e(t)$ category for a specific run was FP then the same run was categorized as a FN by $\dot{e}(t)$ and vice versa.

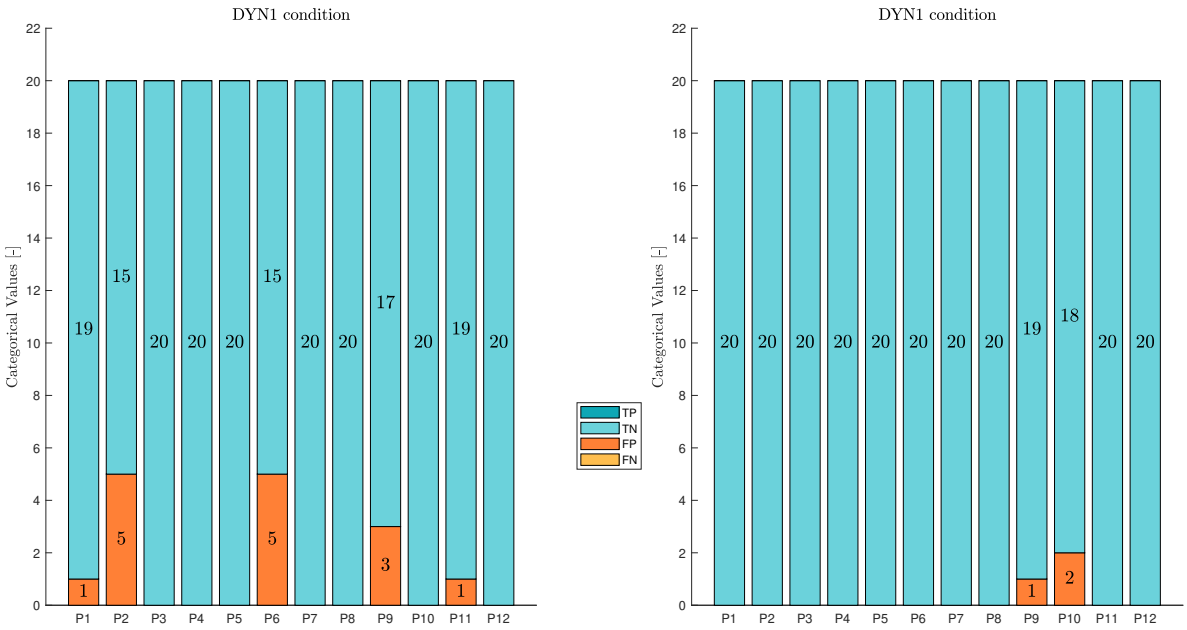

Figure F.1: Subject's accuracy for DYN1 condition. The left subplot corresponds to the compensatory display while the right corresponds to the pursuit display

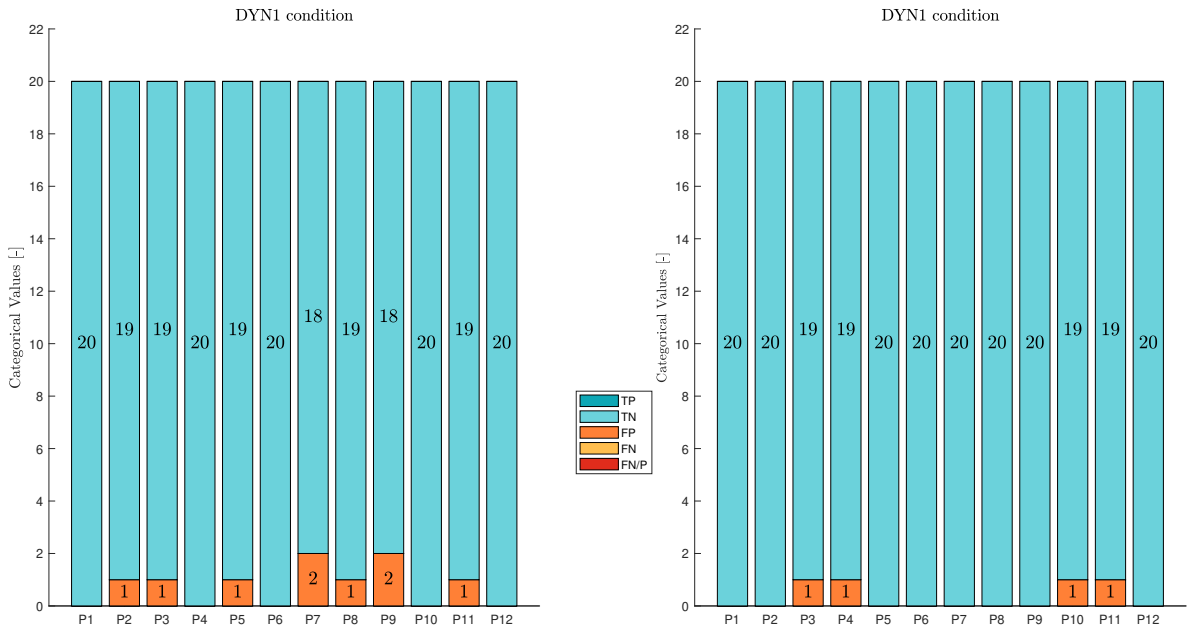

Figure F.2: Combined model's accuracy for DYN1 condition. The left subplot corresponds to the compensatory display while the right corresponds to the pursuit display

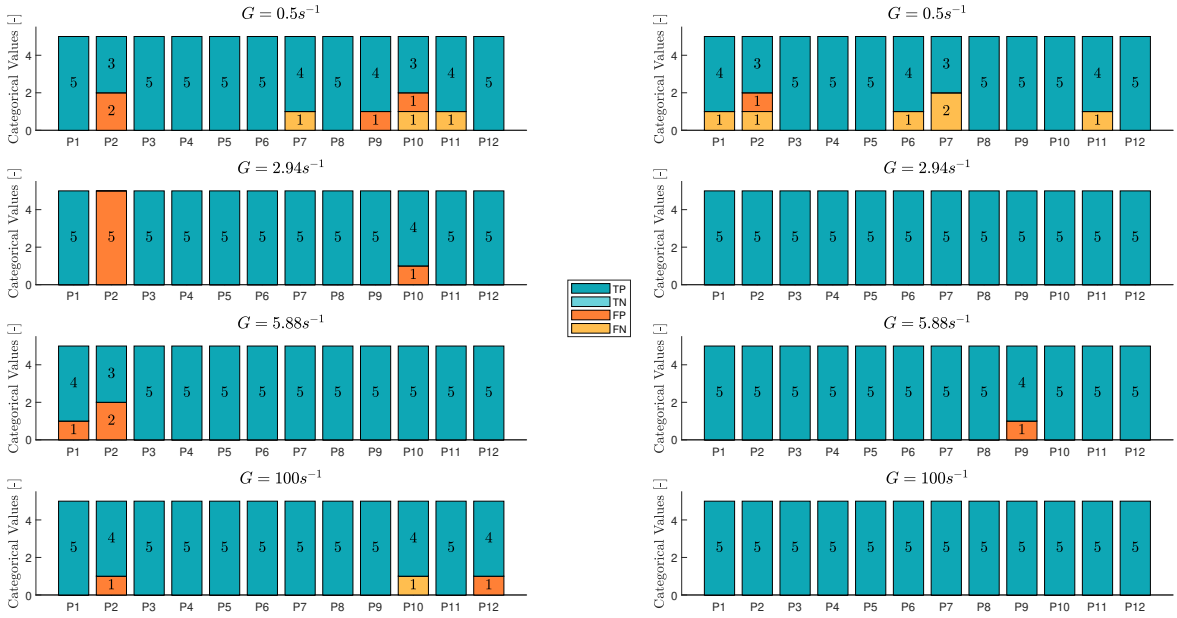

Figure F.3: Subject's accuracy for DYN12 condition. The left subplots correspond to the compensatory display while the right corresponds to the pursuit display

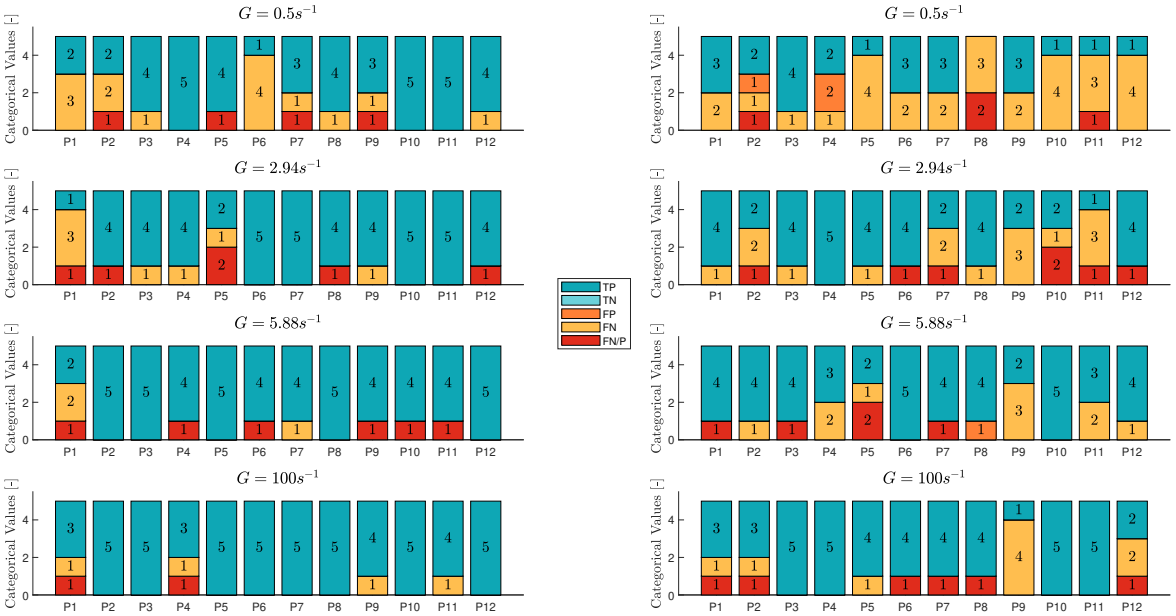

Figure F.4: Combined model's accuracy for DYN12 condition. The left subplots correspond to the compensatory display while the right corresponds to the pursuit display

G

Sensitivity Analysis of ROI

The degradation of Open-Loop (OL) stability occurs when the Human Operator (HO) has yet to detect the change in Controlled Element (CE) dynamics. Once the *detection* occurs, the *identification* and *adjustment* phases take place wherein they adapt to the changed dynamics and adjust for the errors. In this study, a critical parameter was redefined to apply the proposed model to the experimental data: the start of the Region Of Interest (ROI). As outlined in the data analysis methodology, due to the unavailability of time-varying pilot model parameters for the experiments, the ROI starts when the CE dynamics have transitioned to 50% of their final value. This moment in time is consistent for all sigmoids, regardless of their G value, as 50% transition represents the centre of the sigmoid M, while achieving all other percentage values is contingent upon the G value used. This appendix provides details of a post hoc analysis of this selection, to check for its validity and sensitivity.

Given that the loss of OL stability over time ($\phi_m(t)$) triggers the HO's detection, the analysis evaluates the percentage transition value of the CE dynamics at which the operator typically detects the change. This method works as a litmus test for the selected start of ROI. Although the detection lags mentioned in the experiment results show that the detection happens much later in the transition, the figures provided below offer quantitative evidence to support this observation. Importantly, the percentage value represents the proportion of transition completed by the CE, using the sigmoid function to transition from DYN1 to DYN2. This can be interpreted as the sigmoid's percentage transition from P_1 to P_2.

Figure G.1 and Figure G.2 give the HO's detection values per G_{CE} value for the compensatory and pursuit display, respectively.The global mean (indicated by the red horizontal line) is 94.02%, 98.26%, 99.99%, and 100% for the compensatory display and 94.85%, 99.65%, 99.99%, and 100% for the pursuit display, corresponding to $G_{CE} = 0.5$, 2.94, 5.88, and $100s^{-1}$, respectively. Notably, the maximum number of data points that a boxplot can have is five if the HO has all five correct True Positive (TP) detections.

As observed, detection increasingly occurs near or after the completion of the CE dynamics transition as the transition rate increases (higher G). Particularly noteworthy is the lowest percentage value of HO detection, observed for participant P2 in the compensatory display at 6.64% for $G_{CE} = 0.5s^{-1}$. This value may indicate either an early-stage loss of OL stability triggering the HO's detection or a False Positive (FP) detection. Here, the former is considered to be correct as detection is highly subjective and because the subject did not add any comments indicating a FP post the completion of this run.

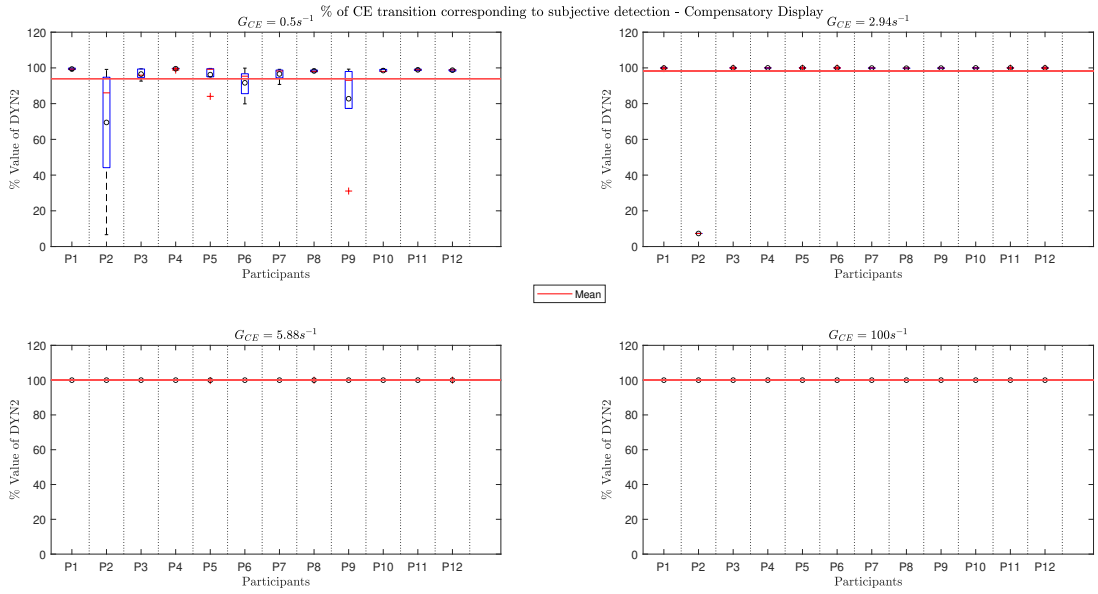

Figure G.1: % of CE transition completed at the moment of HO's detection of change in CE dynamics for the compensatory display

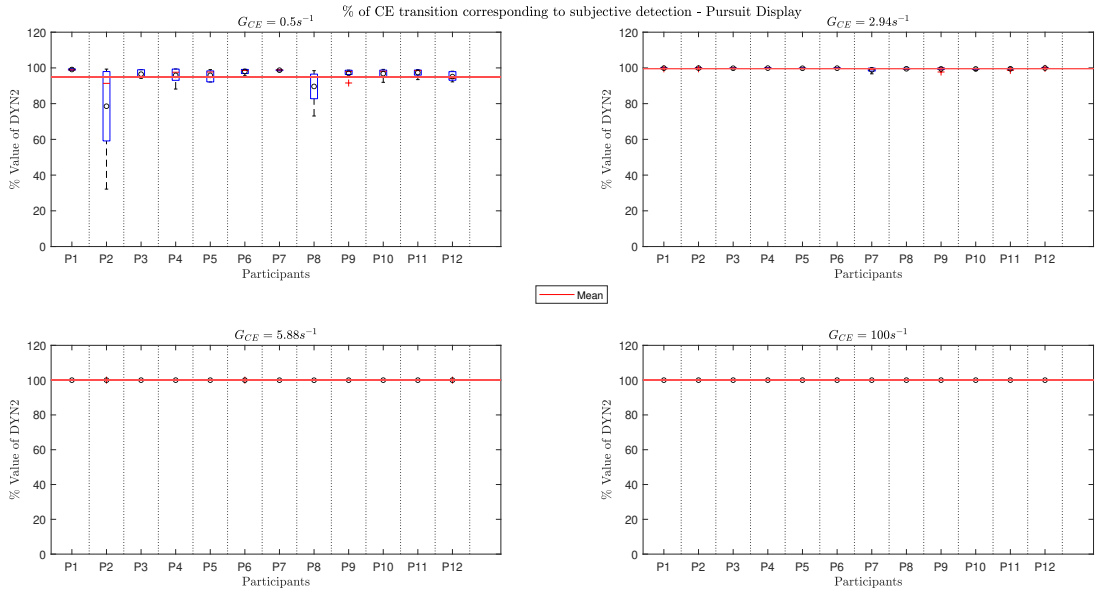

Figure G.2: % of CE transition completed at the moment of HO's detection of change in CE dynamics for the pursuit display

Given below are the figures for the model's detection with Figure G.3 and Figure G.4 corresponding to the compensatory and pursuit displays for when the model uses the error signal $e(t)$ and Figure G.5 and Figure G.6 for when the model uses the error rate signal $\dot{e}(t)$.

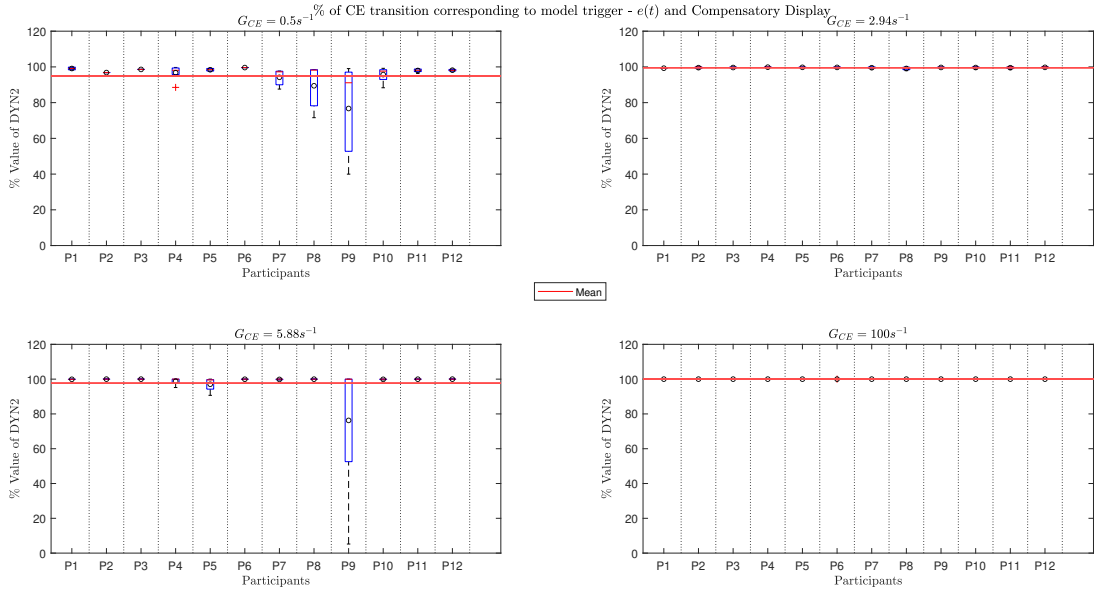

Figure G.3: % of CE transition completed at the moment of model trigger for $e(t)$ in the compensatory display

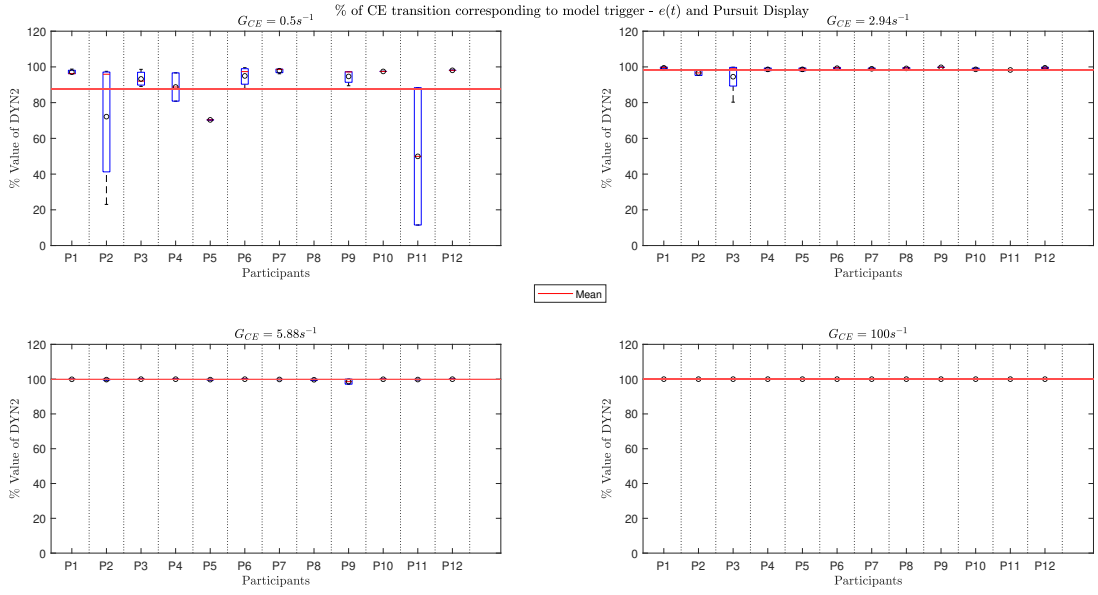

Figure G.4: % of CE transition completed at the moment of model trigger for $e(t)$ in the pursuit display

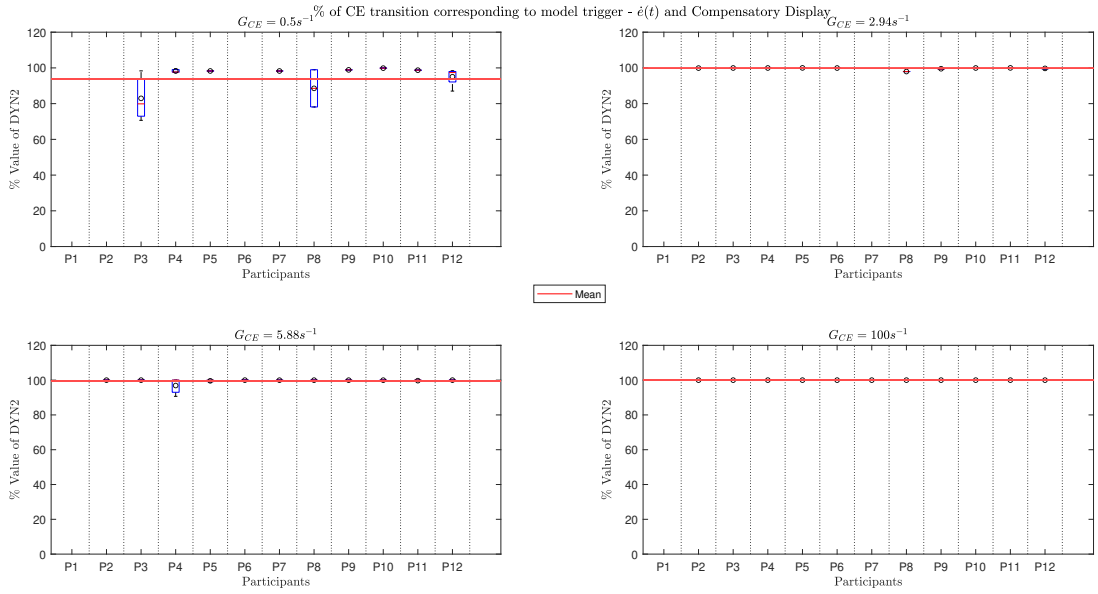

Figure G.5: % of CE transition completed at the moment of model trigger for $\dot{e}(t)$ in the compensatory display

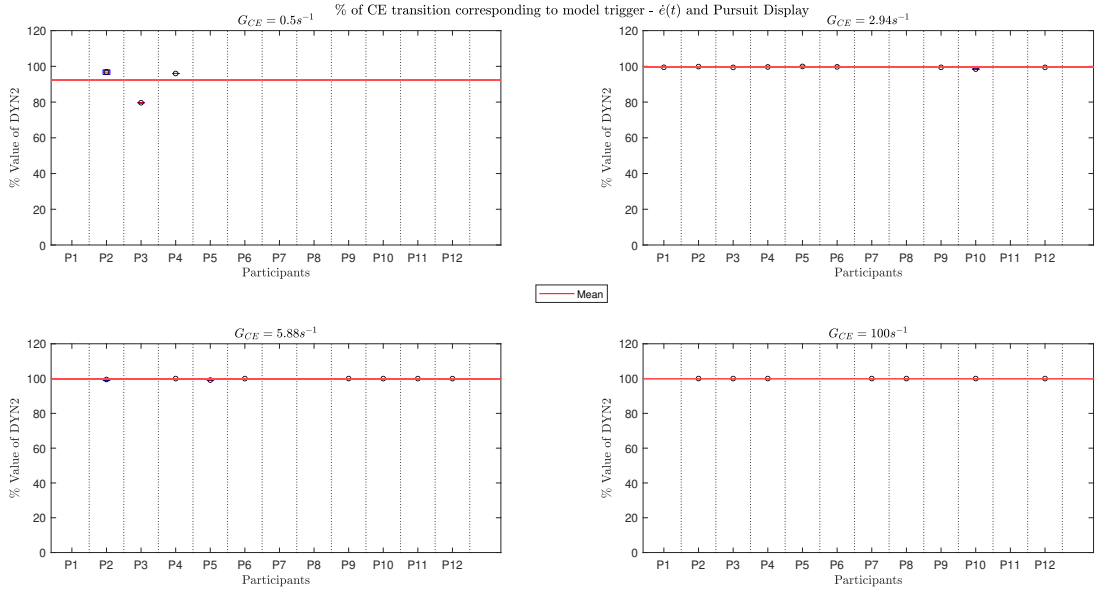

Figure G.6: % of CE transition completed at the moment of model trigger for $\dot{e}(t)$ in the pursuit display

In the case of the $e(t)$ in the compensatory display, the global mean values are found to be 95.02%, 99.60%, 97.58% and 100% for increasing values of the rate of transition. Similarly, for the pursuit display the values are 87.73%, 98.42%, 99.80% and 100%. While, for $\dot{e}(t)$, the values are found to be 93.83%, 99.77%, 99.58% and 100% and; 92.29%, 99.53%, 99.80% and 100% for the compensatory and pursuit display respectively.

Notably, the lowest transition value corresponding to the model's trigger is 5.22% for $e(t)$ in the compensatory display for $G_{CE} = 5.88s^{-1}$ for participant P9. Furthermore, for $\dot{e}(t)$, many boxplots are

absent due to its low accuracy combined with only True Positive (TP) cases considered in this analysis.

Considering these values, if all HO detections and model triggers were required to be contained within the ROI, the percentage transition value of selection would be 5%. However, this approach may present drawbacks as metrics such as detection lag, variance, and model accuracy would become challenging to compare between different G_{CE} values. Nonetheless, this analysis explores a wide range of transition values to assess the effect of the selected value on model performance (trigger time and accuracy). Consequently, Figure G.7 and Figure G.8 illustrate the variation in trigger time for $e(t)$ and $\dot{e}(t)$, while Figure G.9 and Figure G.10 present their respective accuracy. Each subplot in these figures contains percentage transition values of 5%, 50%, 60%, 70%, 80%, 90%, 95%, 96%, 97% and 98%, arranged from left to right.

It is crucial to note that for all percentage values other than 50% (highlighted in green in the plots), the origin of the Y-axis for trigger times varies over time. For instance, the moment of 5% transition for $G = 0.5$, 2.94, 5.88, and $100s^{-1}$ for a sigmoid centered at 35 seconds corresponds to $29.13s$, $34.01s$, $34.51s$, and $34.99s$, respectively.

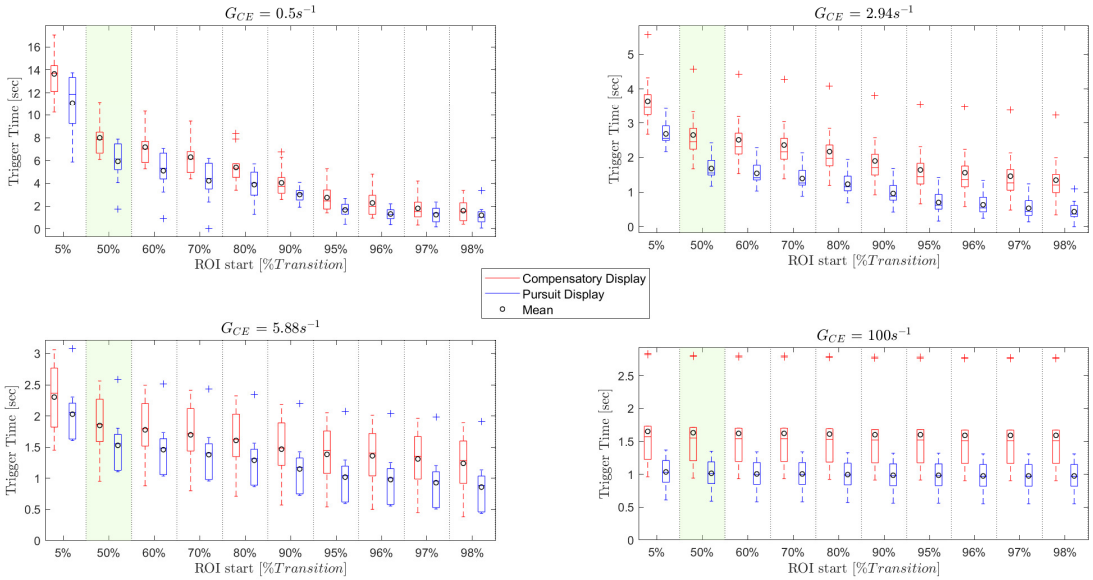

Figure G.7: Variation in trigger time for model using $e(t)$ for both, compensatory (red) and pursuit (blue) display

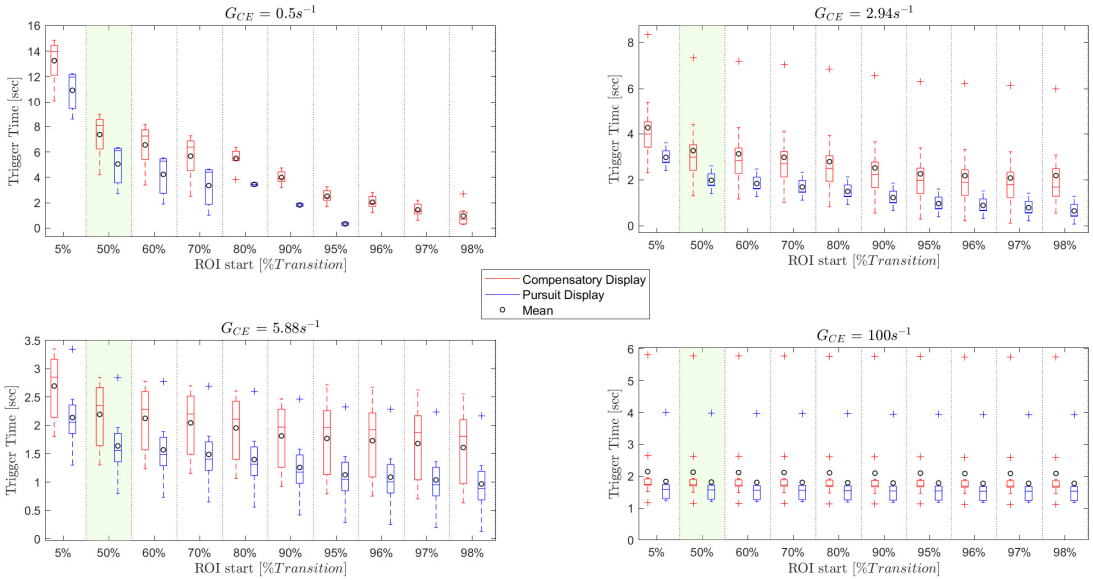

Figure G.8: Variation in trigger time for model using $\dot{e}(t)$ for both, compensatory (red) and pursuit (blue) display

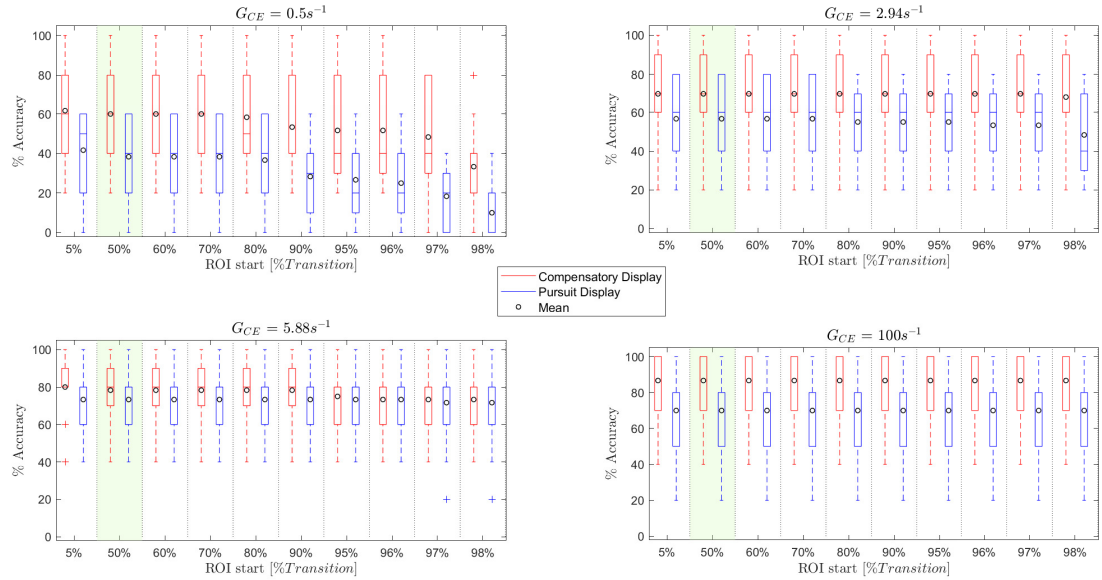

Figure G.9: Variation in model accuracy using $e(t)$ for both, compensatory (red) and pursuit (blue) display

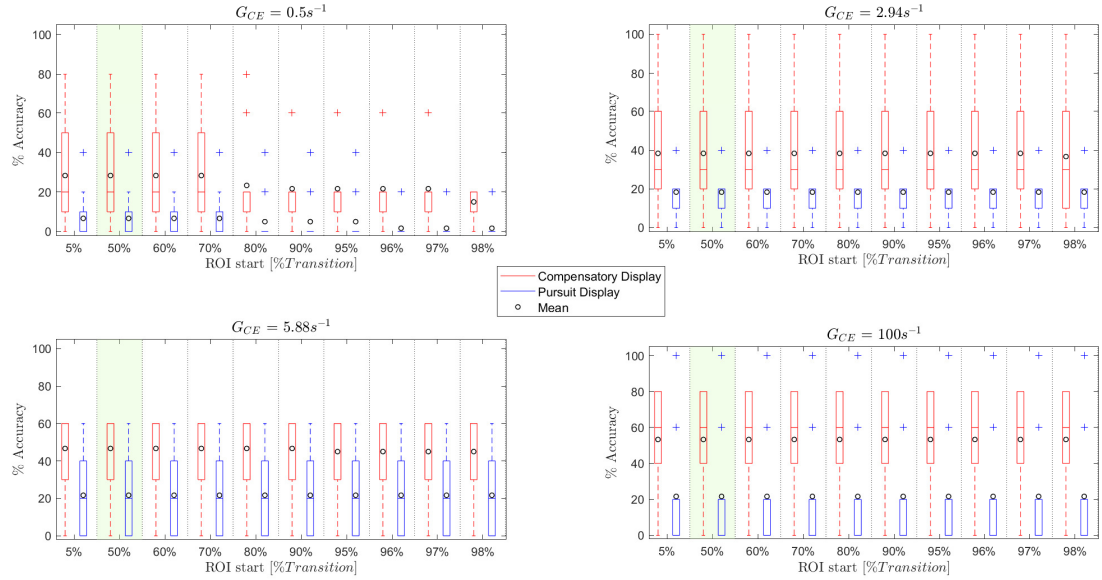

Figure G.10: Variation in model accuracy using $\dot{e}(t)$ for both, compensatory (red) and pursuit (blue) display

From the above figures, several observations can be made. First, the variation in trigger time becomes less distinct as the rate of transition increases. Secondly, for very fast transitions, such as $G = 100s^{-1}$, where the transition time from 5% to 95% is only $0.05s$, both the HO and the model are likely to detect the transition only after its completion, thus not significantly affecting accuracy. Third, the decrease in accuracy from 5% transition to 50% transition is not substantial for either display. In the case of $e(t)$, the maximum percentage accuracy difference is observed for the slowest rate of transition, resulting in a decrease of 1.67% (approximately 3 True Positives) and 3.34% (approximately 5 True Positives). This minor decrease

in accuracy is outweighed by the advantage of having a common time instance for comparing all G values for various performance metrics.

Notably, further reduction in the length of the Region Of Interest (ROI) significantly impacts the model's accuracy, as evidenced by decreasing trends in Figure G.9 and Figure G.10. These findings, particularly the lowest percentage values observed for the subjects and the model, indicate that initiating the ROI at the moment of 50% transition of CE dynamics, as done in the experiments, is satisfactory.

Experiment Run Tables

Below are the experiment run tables for all twelve subjects categorized by display type. It is important to note that this format serves solely to present the run order, which does not follow a Latin square design but instead is entirely randomized.

The run order given below uses the following terminology for ease of interpretation: "G_{CE}/f_t realization" where $G_{CE} = 0$ denotes the DYN1 condition, representing no transition runs.

It is noted that participants identified by odd numbers (P1, P3, P5, P7, P9 and P11) started the experiment using the pursuit display first while the participants identified by even numbers (P2, P4, P6, P8, P10 and P12) used the compensatory display first.

Table H.1: Run order for the compensatory display

	Participants											
Run No.	P1	P2	P3	P4	P5	P6	P7	P8	P9	P10	P11	P12
1	100/4	0/3	2.94/2	0/1	0.5/2	100/1	100/5	100/5	0/2	2.94/2	100/1	100/2
2	100/5	0/2	5.88/2	0.5/3	5.88/3	100/5	2.94/5	100/4	5.88/5	5.88/1	0/3	5.88/1
3	2.94/3	0/2	0/2	0/1	0.5/1	0/2	5.88/5	0/5	5.88/3	100/3	5.88/1	0/5
4	0/5	5.88/5	2.94/4	0/4	100/2	5.88/3	0/4	0/5	0/1	0/2	0/1	100/5
5	0/5	100/4	0.5/1	5.88/4	2.94/5	0/1	100/1	5.88/5	5.88/2	0/2	0/3	0/3
6	2.94/1	100/2	2.94/1	0.5/4	5.88/2	0/3	0.5/1	100/3	0/2	0/4	0/1	2.94/4
7	0/1	0/5	100/2	100/5	100/5	0/4	0.5/5	0/3	2.94/3	0.5/3	0/5	0/4
8	100/2	0.5/3	0/4	2.94/2	0/1	0/5	5.88/1	0.5/5	0/2	5.88/3	0/4	2.94/3
9	0/2	0/4	100/3	0/2	0.5/5	100/3	0/3	0/4	0/3	2.94/3	0/2	0/4
10	2.94/4	0/5	0/2	0/4	0/3	0/4	100/3	0/2	5.88/4	0/1	0/1	0/2
11	0/5	0/4	0/1	0/1	0/4	0.5/5	0/4	2.94/4	0.5/1	0.5/5	0.5/1	0/3
12	5.88/1	2.94/1	2.94/3	2.94/5	0/2	0/2	2.94/2	0.5/2	0.5/4	0/1	2.94/2	100/3
13	2.94/5	5.88/3	0/5	0/4	5.88/4	0/3	100/2	0/2	5.88/1	0/1	0/2	5.88/3
14	0/4	0/3	0/2	0/3	0/3	0.5/2	0/2	0/1	100/1	2.94/5	0.5/2	0/4
15	0/3	0/1	0/4	0/3	0/3	0/1	0/2	2.94/1	0/4	0/5	0/5	0/5
16	2.94/2	0/2	0/1	0/2	0/1	2.94/3	0.5/4	0/4	0/3	0/4	0/4	0/4
17	100/1	100/5	0/1	5.88/1	2.94/1	0/4	0/5	0/1	2.94/5	0.5/4	0/3	0/1
18	0.5/1	5.88/4	0/5	5.88/2	100/1	0.5/4	2.94/3	5.88/2	0/5	0/1	5.88/5	0.5/2
19	0.5/4	0/3	0/5	0/5	0.5/4	0/1	0/5	2.94/5	0/1	100/5	2.94/3	100/4
20	0.5/3	100/3	0/3	0.5/2	0/4	5.88/4	5.88/4	0/5	2.94/1	0/3	0/4	0.5/3
21	0/4	0.5/2	0/5	0/2	0/2	0/4	0.5/3	0.5/3	0/3	100/1	0/1	0.5/1
22	0.5/5	0.5/5	0.5/5	100/1	0/3	0/2	0/2	5.88/4	0/5	0/4	0.5/3	0/1
23	5.88/4	0/1	2.94/5	100/2	5.88/1	0/3	0/3	5.88/3	0/4	0/3	5.88/2	0/1
24	0/4	0/2	0.5/3	100/4	0/5	0/1	0/1	2.94/2	0.5/2	0/5	0/2	0.5/5
25	0/4	0/3	0/2	0/3	0/4	0/3	2.94/4	0/5	0/4	100/4	100/4	0/2
26	0/3	0/1	0/4	0/4	0/2	0/5	0/4	0/4	0/4	5.88/5	0/3	2.94/2
27	5.88/2	0/4	0/3	5.88/5	0/2	5.88/1	100/4	100/1	0/1	5.88/2	0.5/5	0/3
28	0/1	0/4	0/3	0/5	0/5	0/2	0/1	0/3	0.5/3	0/5	5.88/4	0/2
29	0/5	0.5/4	0/4	2.94/4	0/5	2.94/5	0/2	0.5/1	100/3	100/2	0/5	0/2
30	5.88/3	2.94/4	0/3	2.94/1	0/5	0/5	5.88/2	0.5/4	0/5	0/2	100/5	2.94/5
31	0/1	100/1	5.88/3	0/5	100/4	5.88/5	0/1	0/2	0/3	0.5/1	0/2	0/5
32	0/1	5.88/1	100/4	100/3	100/3	0.5/1	2.94/1	5.88/1	0/1	0/3	100/3	0/5
33	0/3	2.94/2	0.5/4	0/1	0/1	2.94/1	0/5	0/1	100/4	0/3	2.94/5	5.88/2
34	100/3	2.94/3	0/1	2.94/3	0/1	5.88/2	0.5/2	0/4	2.94/4	0.5/2	0/4	0/1
35	5.88/5	0/5	100/5	0.5/5	2.94/3	0.5/3	0/3	100/2	0/5	0/4	2.94/1	0.5/4
36	0.5/2	0/1	5.88/5	0/5	0/4	2.94/2	0/3	0/3	100/5	5.88/4	100/2	5.88/5
37	0/2	0/5	0.5/2	5.88/3	0.5/3	2.94/4	5.88/3	2.94/3	100/2	2.94/4	2.94/4	5.88/4
38	0/3	0.5/1	5.88/4	0.5/1	2.94/4	100/4	0/4	0/1	0/2	2.94/1	0.5/4	2.94/1
39	0/2	5.88/2	5.88/1	0/2	2.94/2	0/5	0/1	0/2	2.94/2	0/5	0/5	100/1
40	0/2	2.94/5	100/1	0/3	5.88/5	100/2	0/5	0/3	0.5/5	0/2	5.88/3	0/3

Table H.2: Run order for the pursuit display

	Participants											
Run No.	P1	P2	P3	P4	P5	P6	P7	P8	P9	P10	P11	P12
1	5.88/2	0/1	0/4	2.94/2	0/5	0/2	0/5	0/2	100/4	5.88/3	0/3	5.88/4
2	0/4	100/4	0/5	0/1	0/1	100/1	0/4	0/5	0/2	0/4	0/4	0/1
3	0.5/4	0/4	0/3	5.88/3	2.94/4	0/3	0/2	0/4	0/4	100/1	0/5	100/1
4	2.94/2	5.88/1	100/3	0.5/3	100/2	0/5	0/2	0/5	5.88/3	0/3	0.5/5	2.94/4
5	0.5/1	0/1	100/2	100/3	0/2	100/3	2.94/3	100/5	100/1	0.5/5	2.94/3	100/3
6	0.5/5	100/5	0/2	5.88/5	5.88/5	0.5/3	0/2	100/2	0/3	0/3	2.94/4	0/1
7	0/3	0/4	0/5	0/4	100/5	0/5	100/5	5.88/3	0/4	5.88/4	0.5/3	0/3
8	0/5	100/2	0/3	100/5	0.5/1	0/4	0/4	2.94/2	0/2	0/5	0/5	0/2
9	2.94/5	0/3	0/3	2.94/4	0.5/2	0/1	100/3	2.94/5	0.5/3	100/4	0/1	0/5
10	100/4	5.88/2	2.94/2	100/2	0/3	0.5/4	5.88/5	0/3	0/1	0/3	2.94/2	0/5
11	2.94/3	0.5/2	0.5/4	0/2	0.5/3	0/1	0.5/5	0.5/2	0/3	0.5/2	2.94/1	0/1
12	2.94/4	0.5/4	100/4	0/2	0/5	5.88/4	0.5/3	0/1	0/4	0/2	0/4	5.88/3
13	0/2	0/4	0.5/5	0.5/5	100/3	0/5	2.94/4	0/3	0/1	0/4	0/3	0/4
14	0/3	2.94/4	0/2	0/5	2.94/3	0/3	0/1	0/5	0.5/2	0/1	100/1	100/2
15	0/5	0/2	0.5/3	0/3	2.94/5	0/4	0/3	100/4	2.94/3	100/2	5.88/5	0/3
16	0/1	2.94/2	2.94/5	0/1	0/4	0.5/1	100/4	0.5/1	0.5/5	5.88/2	0/2	0/4
17	0/1	0.5/5	0.5/1	5.88/2	2.94/1	0/2	0/1	2.94/3	2.94/4	0/5	0.5/4	0.5/3
18	5.88/1	5.88/3	0/1	0/1	0/2	2.94/2	2.94/5	0/2	5.88/1	5.88/1	0/2	0/2
19	100/5	5.88/5	2.94/4	0/3	0/3	5.88/5	0/5	0/4	0/2	0.5/1	0.5/1	100/4
20	2.94/1	100/1	5.88/5	100/4	0.5/5	5.88/2	0/4	0/4	100/5	0/1	0/1	0/3
21	100/2	0/4	5.88/3	0/4	2.94/2	0.5/2	0/1	100/3	100/2	2.94/1	2.94/5	5.88/1
22	5.88/3	5.88/4	0/3	0/2	5.88/1	0/3	100/2	0/1	5.88/5	0/1	0/4	5.88/5
23	0/4	0/2	0/4	2.94/1	5.88/2	5.88/3	0/3	0/4	2.94/1	0/5	5.88/1	2.94/3
24	0/3	0/5	0.5/2	5.88/1	0/1	2.94/5	0.5/2	0.5/3	2.94/5	0/5	100/3	0.5/4
25	5.88/5	0/5	100/5	0/5	0/3	0/5	2.94/2	5.88/4	5.88/4	2.94/3	0/4	2.94/2
26	100/1	100/3	0/1	5.88/4	0.5/4	0/2	5.88/3	5.88/2	0/1	0.5/4	0/3	0/1
27	0.5/2	0/3	100/1	2.94/3	0/3	0/4	0.5/1	2.94/1	100/3	0/2	0/2	0.5/1
28	0/2	0/3	0/2	0/3	0/5	100/5	0/3	5.88/5	0.5/1	0/3	5.88/3	0/3
29	100/3	2.94/3	5.88/4	0.5/4	5.88/3	0/1	0/5	0/3	0.5/4	2.94/4	5.88/4	0/4
30	0/2	0/1	0/5	0/1	0/2	5.88/1	0.5/4	0/1	0/4	0/1	0/5	0/4
31	0.5/3	0/2	0/2	0/5	0/1	0.5/5	0/2	0.5/5	0/2	5.88/5	100/2	0/2
32	0/2	0.5/1	0/1	0/2	0/4	2.94/3	0/5	0/2	5.88/2	0/4	0/2	0.5/5
33	0/1	0.5/3	0/5	0/4	0/5	0/4	5.88/4	5.88/1	0/5	0.5/3	100/5	5.88/2
34	0/1	2.94/1	0/1	0/4	0/4	100/4	0/3	0.5/4	0/5	2.94/5	0/1	2.94/1
35	0/5	0/3	5.88/2	2.94/5	0/2	100/2	0/4	0/3	0/5	100/3	0/5	100/5
36	5.88/4	2.94/5	5.88/1	100/1	100/4	2.94/1	0/1	0/5	2.94/2	2.94/2	5.88/2	2.94/5
37	0/4	0/5	0/4	0.5/2	0/1	0/3	2.94/1	0/1	0/5	0/4	100/4	0/2
38	0/5	0/2	2.94/3	0.5/1	5.88/4	0/1	5.88/2	2.94/4	0/3	100/5	0/3	0/5
39	0/4	0/5	2.94/1	0/5	100/1	0/2	5.88/1	100/1	0/3	0/2	0.5/2	0/5
40	0/3	0/1	0/4	0/3	0/4	2.94/4	100/1	0/2	0/1	0/2	0/1	0.5/2

Documents - Human Research Ethics Committee

Attached on the next page is the consent form followed by the experiment briefing submitted to the Human Research Ethics Committee (HREC) under application number 3866. Both these forms were provided to the subjects before starting the experiment.

Experiment Consent Form

Measuring Human Controllers' Detection of Changes in Aircraft Dynamics

I hereby confirm, by ticking the box, that:

1. I volunteer to participate in the experiment conducted by the researcher (**Devashish Patel**), under supervision of **Dr. ir. Daan Pool,** from the Faculty of Aerospace Engineering of TU Delft. I understand that my participation in this experiment is voluntary and that I may withdraw ("opt-out") from the study at any time, for any reason. I understand that I have the right to withdraw the collected data from further analysis within 2 weeks from conducting the experiment. ☐

2. I have read the briefing document and I understand the experiment instructions, and have had all remaining questions answered to my satisfaction. ☐

3. I understand that my participation involves performing manual tracking tasks in the fixed-base HMI-Lab simulator at TU Delft. I understand that only the pseudonymized recorded time traces of the tracking tasks are saved and used for data analysis. ☐

4. I confirm that the researcher has provided me with detailed safety and operational instructions for the HMI-Lab simulator (simulator setup, electro-hydraulic side stick, emergency procedures) used in the experiment. Furthermore, I understand the researcher's instructions for guaranteeing the experiment's compliance with current COVID-19 guidelines, and that this experiment shall at all times follow these guidelines. ☐

5. I understand that the researcher will not identify me by name in any reports or publications that will result from this experiment, and that my confidentiality as a participant in this study will remain secure. Specifically, I understand that any demographic information I provide (gender, age range, ***see next page***) will only be used for reference and always presented in aggregated form in scientific publications. ☐

6. I understand that this research study has been reviewed and approved by the TU Delft Human Research Ethics Committee (HREC). To report any problems regarding my participation in the experiment, I know I can contact the researchers using the contact information below. ☐

My Signature Date

My Printed Name Signature of researcher

Participant Demographic Information

Measuring Human Controllers' Detection of Changes in Aircraft Dynamics

Age range:

- 18 – 19
- 20 – 24
- 25 – 29
- 30 – 34
- 35 – 39
- 40 – 44
- 45 – 49
- 50 – 55
- 55+

Gender: _____

Participant number: _____
(Filled out by the researcher)

Experiment Briefing

Measuring Human Controller's Detection of Changes in Aircraft Dynamics

First of all, thank you for your participation! This experiment is part of an MSc thesis research project that aims to understand and model how a human operator (you) detects that the controlled element dynamics have changed. The experiment consists of a simple tracking task and will be performed in the Human-Machine Interaction Laboratory (HMI-Lab) at TU Delft's Faculty of Aerospace Engineering. This briefing will give an overview of the experiment and explains what is expected from you as a participant. Please read this document carefully. Should any questions or comments remain, always feel free to discuss these with the researcher conducting the experiment.

Experiment Objective

The goal of this experiment is to investigate how human operators detect changes in the controlled element dynamics. Data from this experiment will be used to develop and validate a model that can predict the moment a human operator detects a change in controlled element dynamics and consequently can be used in future models on adaptive manual control behavior.

Experiment Set-up

The experiment will take place in the HMI-Lab (Fig. 1), a fixed-base simulator set-up at TU Delft's Faculty of Aerospace Engineering. The task you will be carrying out is a tracking task with a compensatory and a pursuit display as shown in Fig. 2. This compensatory display shows a fixed reference marker (White Square) and a moving "follower" marker (Green Square), whose lateral displacement indicates the error signal that you will need to correct for while the pursuit display has the reference marker (White Square) to be moving as well with your task remaining the same. Please take a seat on the chair on the right and use the side-stick on your right-hand side to control the system by moving the side-stick to the left and right. There is another side-stick on your left-hand side. The purpose of this side-stick will be explained in the next section.

Figure 1: Illustration of HMI-Lab. The participant will be sitting on the right (blue) seat and controls the side-stick.

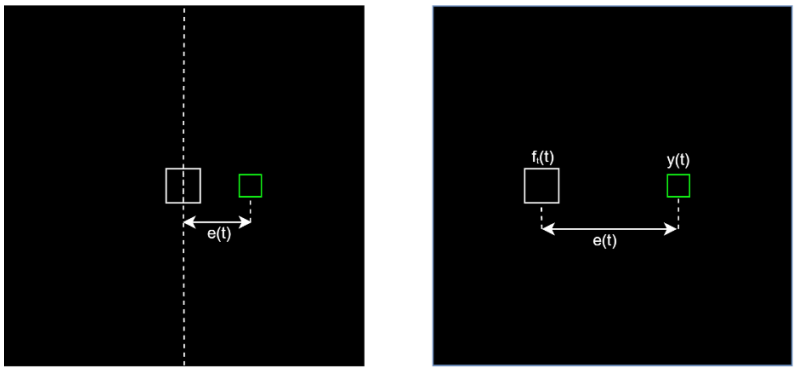

Figure 2: Compensatory display (left) and Pursuit display (right)

Experiment procedure

Before starting the data collection, some training runs will be performed so that you can familiarize yourself with the different scenarios and controlled element dynamics. In the experiment, you will control dynamics that respond like a single integrator (rate control) and transitions between single integrator and double integrator (acceleration control) dynamics. Once your performance is stable, the data collection phase will begin. There is no pre-defined number of tracking runs that are required for collecting the data: the experimenter will simply notify you when sufficient data has been collected. All individual tracking runs last approximately 60 seconds.

It is important that you continue to focus on keeping the error (the distance between the reference and the moving signal) as low as possible during the entire run by continuously controlling the system with the side-stick on your **right**. At the end of each run, the researcher will communicate your score to you. During the runs, the controlled element dynamics may change. If you detect a change in the controlled element dynamics, please **immediately** indicate this by pressing the button on the side-stick to your **left.** Please note that only **some** of the runs will contain a change in the controlled element dynamics, so it is possible to go through an entire run without needing to press the button.

Short breaks can be taken between runs to alleviate any discomfort that might occur due to fatigue, controlling the side-stick, or sitting in a fixed position for a prolonged period. A longer break of approximately 10 minutes will be taken after the first hour. The experiment will last approximately 1.5 hours. Should more breaks be required, you can request them at any moment.

For each subsequent trial, the following procedure will be applied:

1. The researcher applies the settings for the next run.
2. The researcher checks that the participant is ready to proceed and initiates the run after a countdown from 3 (i.e. “3-2-1-go”).
3. The participant performs the tracking task.
4. The participant will be notified of their performance in the run in terms of the error score that will appear on the display after completing the run.

Your Rights & Consent

Experiment participation is voluntary. Should you feel uncomfortable, you can decide to stop your participation at any time. By participating in the experiment, you agree that the collected data may be published. You can ask for this data to be withdrawn within 2 weeks of participating in the experiment. Your personal data will remain confidential and anonymous, only the researcher can link the collected data to a specific participant. To ensure you understand and comply with the conditions of the experiment, you will be asked to sign an informed consent form.

Analysis of Caffeine Requirement

In the total 32 weeks and 3 weekdays, which is the duration of this study, the primary brain food apart from the O_2, H_2O and $food$ necessary to survive life has been coffee, or rather, the caffeine that makes coffee the great capitalist drug that it is. This appendix provides a rudimentary analysis of the amount of caffeine consumed (**read as: "required"**) to deliver this undertaking in my conquest to obtain an ***MSc in Aerospace Engineering***.

Assumptions of analysis:

- The coffee beans used, throughout this thesis, to make the coffee are homogeneous.
- A single dosage of espresso is $\approx 30g$ and contains $63.6mg$ rounded off to $64mg$ of caffeine.
- On weekdays, the average number of espressos consumed are 7. This includes the variations like a lungo. (In honesty, the number should be 8, but a *conservative estimate* is considered best)
- On weekends [I did work on all weekends :(...], the average number of espressos consumed are 2 (Again, a *conservative estimate*)

Basis these assumptions, the amount of coffee cups consumed is obtained as:
Weekdays:

$$(32(weeks) \times 5(weekdays)) + 3(weekdays) = 163\,days$$

$$163(days) \times 7(cups) \times 64(mg) = 73,024\,mg$$

Weekends:

$$(32(weeks) \times 2(weekends)) = 64\,days$$

$$64(days) \times 2(cups) \times 64(mg) = 8,192\,mg$$

Resulting in a total of $81,216mg$ of caffeine. For reference, it takes $\approx 5,000mg$ (Source: Link) for a human to die of an overdose. Therefore, it required a total of 16.24 deaths for me to successfully complete (again an assumption, as I have not yet graduated when writing this) my thesis.

So, one may ask, if all those (coffee-)deaths (16 of those; a *conservative estimate*), excluding the near-death experiences when a code failed or results were found to be unhinged, were worth it. The answer to this question is simple my friend: **"YES! Because an unhealthy obsession with coffee has never failed to make me happy."**

Coffee will save the world
- Devashish, 2024